



Graduation Project - Final Studies Project (PFE)

Field of Study: Mechanical Engineering
Scholar Year : 2023-2024

Fatigue Test Modeling For The European INCEFA-SCALE Project

Confidentiality Notice

Non-confidential and publishable report

Author: Raphael ALVES HAILER

Promotion: 2024

ENSTA Paris Tutor: Anne-lise GLOANEC
Host Organization Tutor: Stéphan COURTIN

Internship From 15/04/2024 to 06/09/2024

Host Organization Name: Électricité de France (EDF) Lab Paris-Saclay
Address: Bd Gaspard Monge, 91120 Palaiseau, France

Confidentiality Notice

This present document is not-confidential. It can be communicated outside in paper format or distributed in electronic format.

Acknowledgements

First and foremost, I want to praise and thank God for the opportunity of working alongside wonderful people and for giving me all the strength and energy necessary to complete this internship at EDF.

I want to express my profound love and fondness for my wife Gabriely, who gave me all the needed support for the completion of this work. Since the beginning of my internship you always motivated me to work hard and give my best. Thank you for believing in my potential and capacity. I love you.

Moreover, I feel extremely grateful to have been tutored by Mr. Stéphan Courtin. Thank you for all your support and patience throughout my internship at EDF. Many problems have arisen, but we managed to bypass them and deliver the results in this report.

I would like to express my gratitude to the Ermes research team at EDF Lab Paris-Saclay, for helping me with the most basic questions on how to use `code_aster` and following along the evolution of my work.

Furthermore, I want to thank EDF Lab Paris-Saclay and the École Nationale Supérieure de Techniques Avancées (ENSTA) Paris, for making this internship experience possible. This has been my first research experience in a big company, conducting a research that could benefit all members of the INCEFA-SCALE project, and I loved it.

This study was partly financed in part by the Coordenação de Aperfeiçoamento de Pessoal de Nível Superior - Brasil (CAPES) - Finance Code 001. I want to express my thankfulness to CAPES for the BRAFITEC program, which granted me financial support to maintain myself in France during all the period of my studies. Without this support, I would never have achieved so much in my academic journey.

This report symbolizes the end of my academic journey at ENSTA, marking the last page of a chapter in the book of my life. I look forward to using all the gathered knowledge in my years of study for the best.

Last but not least, I want to thank my family in Brazil for giving me so much love and support during my years in France.

Abstract

In this study, we are interested in characterizing the mechanical response of the 316L stainless steel through the use of finite elements method, using the Chaboche constitutive model with a variety of parameter sets. An optimization of the model parameters is conducted using the NSGA-II evolutionary algorithm, in order to seek a model that can accurately capture the deformation of full-scale specimens under cyclic loading with different strain amplitudes. The main objective is to contribute to the European INCEFA-SCALE project, proposing a framework that can be replicated by other members to enhance the numerical models of the 316L steel, allowing for better fatigue life predictions and failure assessment.

Keywords— Finite Element Analysis, Evolutionary Algorithms, NSGA-II, Fatigue, Environmentally Assisted Fatigue, INCEFA-SCALE

Résumé

Dans cette étude, nous nous intéressons à la caractérisation de la réponse mécanique de l'acier inoxydable 316L par l'utilisation de la méthode des éléments finis, en utilisant le modèle constitutif de Chaboche avec une variété d'ensembles de paramètres. Une optimisation des paramètres du modèle est réalisée à l'aide de l'algorithme évolutionnaire NSGA-II, afin de rechercher un modèle capable de capturer avec précision la déformation d'échantillons grandeur nature sous chargement cyclique avec différentes amplitudes de déformation. L'objectif principal est de contribuer au projet européen INCEFA-SCALE, en proposant un cadre qui peut être reproduit par d'autres membres pour améliorer les modèles numériques de l'acier 316L, permettant de meilleures prévisions de la durée de vie en fatigue et de l'évaluation des défaillances.

Mots clés— Analyse par Éléments Finis, Algorithmes Évolutionnaires, NSGA-II, Fatigue, Fatigue Assistée par l'Environnement, INCEFA-SCALE

Contents

1	Introduction	13
2	Theoretical section on fatigue	15
2.1	Historical context and motivation	15
2.2	Fundamentals of fracture mechanics and fatigue	16
2.2.1	Characterization of the crack tip	17
2.2.2	Fatigue crack growth	20
2.3	The 316L stainless steel	22
2.4	The Chaboche Constitutive Model	23
2.5	Important measures	24
3	Computational tools	26
3.1	Salome Meca	26
4	Fundamentals of evolutionary algorithms in multi-objective optimization	27
4.1	Deterministic multi-objective optimization	27
4.2	Evolutionary algorithms	29
4.2.1	Introduction to evolutionary algorithms	29
4.2.2	Motivation	29
4.2.3	Non-dominated Sorting Genetic Algorithm II (NSGA-II)	30
4.3	Implementing NSGA-II in the context of this work	34
5	Results and discussion	35
5.1	Notched Specimen	35
5.1.1	Comparison with INCEFA-SCALE results	35
5.1.2	Comparison of studied parameter sets within INCEFA-SCALE	45
5.1.3	Optimization of the Chaboche model parameters	52
5.1.4	Implementation of optimized parameters in diagnostic tests	57
5.1.5	Implementation of optimized parameters in new specimens	61
5.1.6	Conclusion on the notched specimens	63
5.2	Variable amplitude loading	65
5.2.1	Conclusion on the variable amplitude loading test	66
6	Conclusion and perspectives	67
7	References	68
A	Technical Drawings	72

List of Figures

1	Lithograph of the Versailles-Paris railway accident in may 8, 1842. Courtesy of the Bibliothèque Nationale de France.	15
2	Typical S-N curve, or Wöhler curve. Credits to [14].	16
3	Illustration of the three crack opening modes: opening mode (mode I), sliding mode (mode II) and tearing mode (mode III). Credits to [19].	17
4	Illustration of the components of the stress tensor σ , indicating the direction of all components. Credits to [20].	18
5	Illustration of the polar coordinate system at the crack tip. Credits to [25]. . . .	18
6	Crack growth regimes according to the Paris Law. Credits to [14].	20
7	Schematic view of crack growth evolution through the load cycles. Credits to [29].	21
8	Experimental data on the cyclic hardening and softening phenomena in the 316L stainless steel, in strain-controlled cyclic tests. Credits to [17].	21
9	Example of a Pareto front in a bi-objective optimization problem. Credits to [36].	28
10	One of the evolved ST5-33-142-7 antenna prototypes developed by NASA for the Space Technology 5 (ST5) mission. Credits to [40].	29
11	Visual representation of the procedure to compute the crowding distance for the i th individual inside a rank. Credits to text[46]	32
12	NSGA-II algorithm procedure to extract new generation. Credits to [7].	34
13	Illustration of notched specimen with its geometrical parameters D, r and d . Credits to [52].	35
14	Illustration of the cyclic stress-strain curve concept, used to simplify numerical simulations. Credits to [53].	36
15	Illustration containing a wide variety of experimental data points from contributors of the INCEFA-SCALE project, used to build the EDF bi-linear cyclic stress-strain curve.	36
16	Reduced stress-strain curves provided by Framatome France (FRF) and EDF for the numerical simulations, compared with experimental data in different fatigue life stages.	37
17	Illustration of the meshes used for the numerical simulations on the notched specimens, together with the respective design parameters defining each geometry. The red dots highlight the position of the extensometer measurement sought.	38
18	Comparison of numerical and experimental results of extensometer amplitude and Von Mises equivalent strain, in diagnostic tests.	41
19	Von Mises equivalent stress and strain at bottom edge for the diagnostic test of the Framatome Specimen.	42
20	Von Mises equivalent stress and strain at bottom edge for the diagnostic test of the EDF Specimen in all steps.	43
21	Von Mises equivalent stress and strain at bottom edge for the diagnostic test of the KTU Specimen in all steps.	45
22	Elementary cube used to compare all the parameter sets used to describe the 316L steel in the numerical simulations, with all nodes identified.	46
23	Figure comparing simulation results with experimental data using Zhang's parameter sets, with and without history effect at different stages of fatigue life. . .	48
24	Figure comparing simulation results with experimental data using CEA parameter sets.	49
25	Figure comparing simulation results with experimental data using CEA parameter sets, with separate subplots for each strain amplitude.	50
26	Comparison of simulation results from the best parameter sets for both fatigue life stages studied.	51

LIST OF FIGURES

27	Enumeration of points of interest to compute objective functions with Equation 17, with FEA result with arbitrary set of parameters.	53
28	Illustration of all individuals in the three-dimensional objective space, for all runs of the NSGA-II algorithm.	56
29	Hysteresis loops found using the optimized parameter set, compared with experimental data at half life stage of fatigue life.	57
30	Von Mises equivalent stress and strain at bottom edge, using the optimized parameter set on all diagnostic tests.	59
31	Hysteresis loops using the optimized parameter set on all diagnostic tests, considering the applied force and the Von Mises equivalent Strain as key parameters.	61
32	Illustration of the new meshes used for the numerical simulations on the notched specimens, together with the respective design parameters defining each geometry.	62
33	Illustration of the strain evolution in a POUL strain-controlled test.	65
34	Illustration of the strain evolution in a POUL strain-controlled test.	66
A.1	Framatome France essay specimen used in this work	72
A.2	EDF essay specimen used in this work	73
A.3	KTU essay specimen used in this work	74

List of Tables

1	Chemical composition of the 316L stainless steel. Credits to [31].	22
2	Reference data on a few physical properties of the 316L stainless steel. Credits to [31].	23
3	Breakdown of Chaboche elastic-plastic cyclic model equations. Table extracted from [17].	24
4	Von Mises equivalent strain results obtained in this work using stress-strain curves.	39
5	Comparison between extensometer results obtained by INCEFA-SCALE members on diagnostic tests and the results obtained in this work using stress-strain curves.	40
6	Comparison of the relative errors obtained in the FEA simulations for the extensometer amplitude measurement.	40
7	Comparison of the Chaboche constitutive model parameter sets.	46
8	History effect parameters extracted from Zhang's thesis [17]. The Q_m and Q_0 values have been corrected, as they are wrong in [17].	46
9	Obtained ε_{VM} results at the notch root on Framatome's diagnostic test, using Zhang's parameter set without history effect and the parameter set 2 from CEA to describe the Chaboche constitutive model.	52
10	Comparison between extensometer results obtained by INCEFA-SCALE members on the diagnostic test using Framatome's specimen and the ones with Zhang's parameter set without history effect and the parameter set 2 from CEA to describe the Chaboche constitutive model.	52
11	Comparison of the relative errors obtained in the FEA simulations for the extensometer amplitude measurement, using the best parameter sets found.	52
12	Obtained optimized parameter set for the Chaboche constitutive model, compared with Zhang's parameters.	57
13	Relative errors found for the FEA results in various specimens from the INCEFA-SCALE project.	63
14	Comparison with results obtained by INCEFA-SCALE members on diagnostic tests, with different target ε_{VM} at the notch root, compared with the results obtained in this work using the optimized parameters of the Chaboche constitutive model.	64
15	Presentation of numerical results obtained in specimens from various laboratories participating in the INCEFA-SCALE project, using the optimized parameters of the Chaboche constitutive model.	64

List of Symbols

Material Properties

E Young modulus

G Shear modulus

ν Poisson's ratio

Solid Mechanics Symbols

σ Stress

σ_{ij} Normal stress component

τ_{ij} Shear stress component

σ_{mean} Mean stress

U Displacement vector

u Displacement in the x direction

v Displacement in the y direction

w Displacement in the z direction

K Stress intensity factor

σ_Y Yield strength

a Crack length

σ_{max} Maximum stress

σ_{min} Minimum stress

$\Delta\sigma$ Stress range

ε Strain

ε_{ij} Strain components

s Deviatoric stress tensor

s_{ij} Deviatoric stress components

X Backstress tensor

C_i Kinematic hardening modulus

γ_i Recovery coefficient

$\dot{\gamma}$ Equivalent plastic strain rate

λ Plastic multiplier

R Isotropic hardening modulus

σ_{VM} Von Mises equivalent stress

ε_{VM} Von Mises equivalent strain

$\mathbf{dev}(\varepsilon)$ Deviatoric strain tensor

$\Delta\varepsilon$ Strain range

Geometrical Properties

D Nominal diameter

d Reduced diameter

r Notch radius

Optimization Framework Symbols

f Objective function

g Constraint function

\mathbf{x} Design vector

χ Design space

\mathbf{X} Objective space

\mathbb{P} Pareto front

P_t Population at a given instant t

N Population size

\mathcal{F}_i i th front in objective space

n_{gen} Number of generations

d_i Crowding distance of the i th individual

η_{SBX} Crossover operator parameter controlling the PDF of the offspring

η_{PM} Mutation operator parameter controlling the PDF of the offspring

Number Sets

\mathbb{R} Real numbers

\mathbb{N}^* Natural numbers excluding zero

Other symbols

t Time

δ Relative error

F Force

List of Acronyms

- EAF** — Environmentally Assisted Fatigue
- NPP** — Nuclear Power Plant
- CAD** — Computer-Aided Design
- CEA** — Commissariat à l'Énergie Atomique et aux Énergies Alternatives
- EDF** — Électricité de France
- SI** — International System of Units
- NRC** — United States Nuclear Regulatory Commission
- LWRs** — Light Water Reactors
- R&D** — Research and Development
- NSGA-II** — Non-Dominated Sorting Genetic Algorithm II
- DoE** — Design of Experiment
- PSO** — Particle Swarm Optimization
- PDF** — Probability Density Function
- SBX** — Simulated Binary Crossover
- FEA** — Finite Element Analysis
- RMSE** — Root Mean Square Error
- POUL** — Periodic Over-Underload
- POL** — Periodic Overload
- PUL** — Periodic Underload

1 Introduction

In modern society, the nuclear power is of pivotal importance for the global energy landscape of certain countries. As of 2021, 69% of the total energy generated by France was due to nuclear energy [1], and many other European countries fall into the same dependence. Nuclear energy has been around since the 20th century, and the average age of nuclear reactors worldwide is 31.9 years, with an average age of 35.6 years in Europe [2].

Considering the age of nuclear reactors, it is important to assess the possibility of component failure due to *Environmentally Assisted Fatigue* (EAF). For this reason, the European Commission HORIZON2020 program supports the INCEFA-SCALE [3] (INcreasing safety in nuclear power plants by Covering gaps in Environmental Fatigue Assessment – focusing on gaps between laboratory data and component SCALE) project, which is an international project counting on the collaboration of multiple research institutes, universities and industrial partners. It is the direct successor of the INCEFA-PLUS [4] program, which operated between 2015 and 2020.

Studying and comprehending the gaps in the current knowledge of EAF is crucial, because this process can lead to the deterioration of structural components. It has been observed that the current EAF methodologies do not provide an acceptable framework to work with, and this is mainly attributed to the laboratory-to-scale knowledge gap [3]. The primary objective of the INCEFA-SCALE project is to enhance the ability of correctly predicting the lifetimes of *Nuclear Power Plant* (NPP) components by filling the knowledge gap that exists when addressing the transferability of laboratory-scale tests to real component geometries and loads, in a way that international guidelines can be reviewed for fatigue assessment in the nuclear sector.

The INCEFA-SCALE project is focused in gathering and analyzing experimental data on solid, hollow and notched specimens, in order to better comprehend how environmental factors can affect the component's lifetime. These environmental factors can vary from temperature to the surrounding fluid, such as water with different chemical compositions or air. In addition, the project aims at developing numerical models and simulation tools to predict fatigue life and mechanical behavior of the pieces studied. In doing so, the collaborators of the INCEFA-SCALE project can assure the sharing of knowledge and good practices when it comes to researching on EAF in the nuclear industry on an international landscape.

In the context of the INCEFA-SCALE project, the present work is dedicated to study the effects of specimen geometry and load evolution when characterizing the EAF phenomenon in SAE 316L stainless steel, one of the most important materials in NPPs.

Considering the plan of the present study, a theoretical framework and a presentation of the material of interest are found in Section 2. Additionally, the Chaboche constitutive model is presented, as this is the mathematical model used in the numerical simulations.

Furthermore, in Section 3 the open source software Salome Meca is introduced, which combines Salome [5], a powerful open-source *Computer-Aided design* (CAD) and post-processor software developed by *Commissariat à l'Énergie Atomique et aux Énergies Alternatives*(CEA) and *Électricité de France*(EDF), with `code_aster` [6], an open source finite elements numerical solver developed by EDF to conduct numerical analysis on a multitude of physical phenomena.

After the presentation of the theoretical and computational tools used for the research, in Section 4 we have a in depth description of multi-objective optimization and evolutionary algorithms. This section is of pivotal importance, as it introduces the reader to mathematical notions of multi-objective optimization, in addition to explaining the NSGA-II algorithm [7], which is the evolutionary algorithm used to build the optimization framework that will be used for the identification of optimal parameters for the Chaboche constitutive model. For further reading on the subject, one can refer to [8, 9], which covers more general cases in which uncertainty is involved, as well as constraint functions. The notations used in this work are inspired by these two works.

The optimized parameters are going to be further used to compare numerical results with experimental ones on real scale specimens. The development of an optimized numerical model that can represent the real scale behavior of components is extremely important, as it can be used to predict the mechanical response of more complex components under cyclic loads and avoid costs with real life experiments.

In the sequence, all the obtained results are presented in Section 5, together with explanations on how `code_aster` has been implemented, important parameter values, meshes used, among other aspects related to the numerical studies. This work focuses on implementing all the theoretical framework developed to study different geometries of notched specimens under different loads, in order to determine if the stress concentration is correctly captured by the numerical model, as well as the elongation of the specimen through time. After this, a small subsection on the study on the implementation of the optimized parameter set in a variable amplitude loading scenario is presented, comparing with experimental results from EDF.

Finally, a brief conclusion is presented in Section 6, so as to analyze the results obtained and discuss regarding future work that can be done on the topic, especially due to the time constraints found during the duration of the internship at EDF.

2 Theoretical section on fatigue

This section is destined to highlight the principles behind fatigue assessment, starting with the historical context and motivation behind the development of this field of research. Further on, we will delve in the development of the theory behind fatigue failure assessment and analysis, in order to comprehend the main theoretical tools. In the sequence, the material of interest for the INCEFA-SCALE project, the 316L stainless steel, is presented. At last, the main constitutive model used in this work, the Chaboche model, is presented in more details, as well as important physical quantities to be used in the present study.

2.1 Historical context and motivation

In the 19th century, the industrial revolution brought major advancements to the industry and society. During this period, there was a shift from a mainly agrarian economy to an economy heavily based on the mass production of goods, driven by mechanized manufacturing in the industries.

With the advent of the steam engine, key investments were made to the rail systems, and the steam-powered locomotives were of pivotal importance for transportation, be it of goods, coal, materials or travelers. It is important to note that in the rail system as well as in many other industries at the time, machines were mainly based on axles and rotating pieces, that were subjected to cyclic loads and deformations.

But not only machinery pieces were victims of mechanical failure. In 1829, a German mining official called Wilhelm August Julius Albert described the process of designing the first wire rope, documenting his testing procedures. He is thought to be the first person to document bending fatigue tests of wire ropes with a scientific basis [10].

Regarding railway systems, numerous axle failures were documented and these catastrophic failures led to a significant number of deaths and material loss. One of the first documented cases of a catastrophic failure in rail transportation was the accident of the train Versailles-Paris in may 8, 1842. This accident is responsible for killing dozens of people and the cause of the accident is attributed to a mechanical failure in the axle of the first locomotive, which was ruptured in two different spots [11, 12].



Figure 1: Lithograph of the Versailles-Paris railway accident in may 8, 1842. Courtesy of the Bibliothèque Nationale de France.

It was in this context that the German engineer August Wöhler conducted systematic alter-

nating bending tests on railway axles [12].

Wöhler realized that even a load far below the ultimate strength of a material could lead to a rupture of the specimen, if this load were to be applied in a cyclic manner [13]. The fatigue damage could not be seen, and this was thought to be a mysterious phenomenon for engineers at the time.

His contributions led to the creation of the S-N curve, also referred to as the Wöhler curve. The S-N curve establishes a relationship between the cyclic stress amplitude and the number of cycles needed in order for a piece to fail due to fatigue. Moreover, Wöhler created the concept of endurance limit, which is the asymptotic value of stress as the number of cycles increases. This is the limit below which there will never be any failure due to fatigue, meaning that a piece subjected to a stress amplitude smaller than the endurance limit will have an "infinite" life-time, and this is considered the unlimited endurance [12].

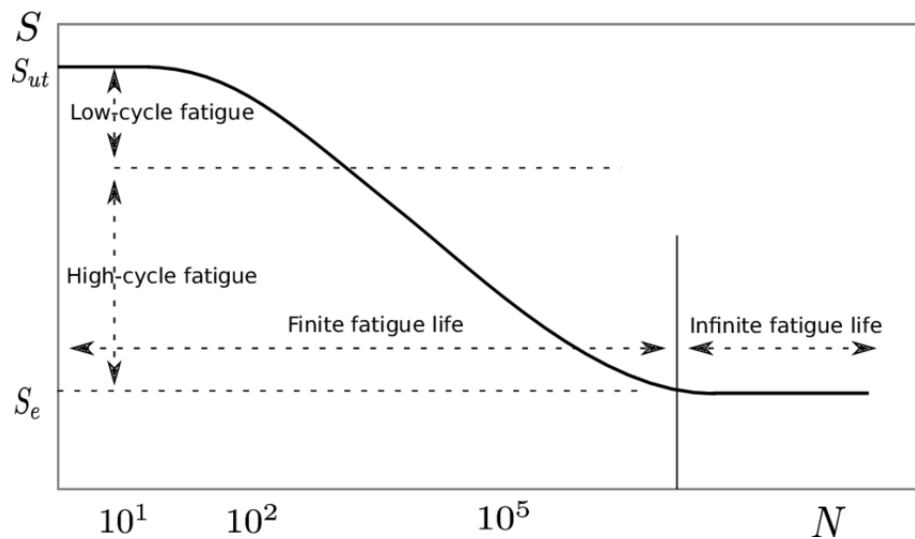


Figure 2: Typical S-N curve, or Wöhler curve. Credits to [14].

Wöhler studied cyclic loads with mean stress $\sigma_{mean} = 0$, thus the S-N curves studied by him represented the relationship between the maximum stress and the number of cycles needed for fatigue failure. Further studies on the influence of σ_{mean} were conducted by Gerber (1874) and by Goodman and Haigh (1899). Relevant empirical laws were proposed by Basquin (1910) and Gough and Pollard (1926), in parallel to other studies being conducted at the time concerning micro-mechanisms of fatigue [12].

During the 20th century, many other catastrophic failures due to fatigue occurred, and not only in the railway engineering domain but also in the aeronautics domain. One of the best examples of a catastrophic failure due to fatigue in the aeronautical sector is the failure of two de Havilland Comet I aircraft, the first commercial jet airliner, in 1954. The cause of the failures was attributed a crack propagation due to cyclic pressurization of the cabin, being originated from stress concentration in the square-shaped windows of the cabin [15]. These failures drive the research field of fatigue failure, so as to improve the safety and reliability of day to day transport, as well as in the main sectors of the industry.

2.2 Fundamentals of fracture mechanics and fatigue

Mechanical fatigue is one of the main mechanisms for which catastrophic failures occur, as discussed in the previous subsection. It is defined as a delayed fracture under cyclic loading [16], and the failure results from a cumulative damage to the material. As Wöhler discovered, fatigue failure occurs at levels of stress far below the ultimate strength, and it initiates with cracks in

areas with high stress concentration, such as sharp corners and edges. The cyclic loading causes the crack to grow, leading ultimately to a rupture or fracture of the piece.

This way, it is important to address the field of fracture mechanics, in order to comprehend crack growth in materials subjected to cyclic loads. For such, the present overview is heavily based on the PhD thesis of Wen Zhang [17]. The main points are going to be presented for better comprehension.

2.2.1 Characterization of the crack tip

When it comes to fracture mechanics and crack growth, it is necessary to comprehend what is a crack and especially how to characterize the crack tip. This is relevant because fatigue is a phenomenon that consists in crack initiation, crack propagation and material fracture when subjected to a cyclic loading.

The crack is the region where material gets ruptured, and it is considered to be locally plane, meaning that a crack presents a local plane of symmetry [17]. The crack tip is a very distorted region at the end of the crack, where the atomic bonds are completely broken. This type of distortion is then more severe than a vacancy or a dislocation [18].

When considering the presence of a symmetrical plane, it is possible to decompose the crack opening into three elementary modes, that corresponds to the three main modes of fracture:

- Opening mode (mode I): In this mode the tensile stress is perpendicular to the crack plane;
- Sliding mode (mode II): Characterized by shear stress that is parallel to the plane of the crack and perpendicular to the direction of the crack;
- Tearing mode (mode III): this mode is defined by a shear stress that is acting parallel to both the plane of the crack and to the crack front.

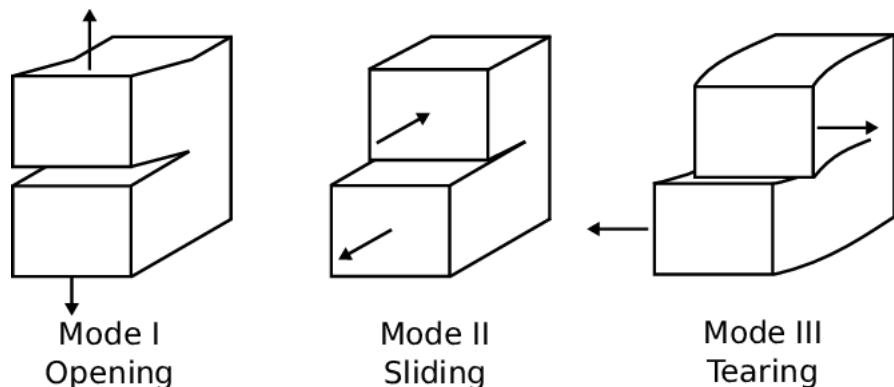


Figure 3: Illustration of the three crack opening modes: opening mode (mode I), sliding mode (mode II) and tearing mode (mode III). Credits to [19].

Before continuing, it is important to set some notations. In this work, E , G and ν will refer to the Young modulus, the shear modulus and the Poisson's ratio of the material, respectively. The Young modulus is commonly referred to as the modulus of elasticity of a material. These three material properties are related by the following equation, when in elastic regime:

$$E = 2G(1 + \nu) \quad (1)$$

In addition, the stress tensor σ is considered to be a symmetrical second order tensor containing normal and shear stresses, denoted respectively by σ_{ij} and τ_{ij} , being i and j used to

indicate the directions. The complete tensor can be represented as shown in Equation 2, and Figure 4 illustrates the direction of each stress component.

$$\sigma = \begin{bmatrix} \sigma_{xx} & \tau_{xy} & \tau_{xz} \\ \tau_{yx} & \sigma_{yy} & \tau_{yz} \\ \tau_{zx} & \tau_{zy} & \sigma_{zz} \end{bmatrix} \quad (2)$$

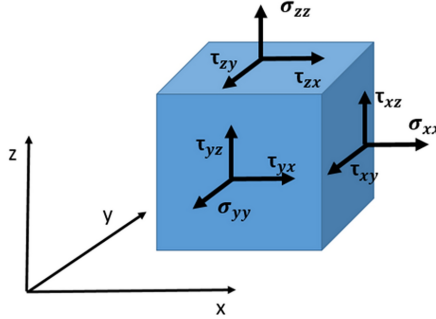


Figure 4: Illustration of the components of the stress tensor σ , indicating the direction of all components. Credits to [20].

Additionally, the displacement vector denoted by $U = (u, v, w) \in \mathbb{R}^3$ contains the displacement u , v and w , that are in the x , y and z directions, respectively.

When considering a crack in an infinite plane with an isotropic linear elastic material, with an external loading being applied to the body, Westergaard [21], Williams [22] and Irwin [23] are considered to be the first ones to express the elastic stress field analytically in the crack tip region. By considering the coordinate system in Figure 5, the stress field for an elastic cracked body at (r, θ) can be described by the use of a 1st order Taylor series expansion [24], such as in Equation 3.

$$\sigma_{ij} = \frac{K}{\sqrt{2\pi r}} W_{ij}(\theta) + \text{higher order terms} \quad (3)$$

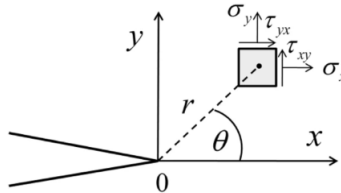


Figure 5: Illustration of the polar coordinate system at the crack tip. Credits to [25].

In Equation 3, K is the stress intensity factor, with its unit in the *International System of Units* (SI) being $\text{Pa}\cdot\text{m}^{1/2}$, while f_{ij} is a non-dimensional function of the angle θ . As the distance from the crack tip r goes to zero, then $\sigma_{ij} \rightarrow +\infty$, and thus a stress singularity state is achieved [26]. In reality, at small values of r we encounter ourselves in the plastic zone, due to the stress exceeding the yield strength of the material σ_Y , and thus the linear elastic solution is not suitable anymore.

By examining the modes of crack opening, it is possible to see that modes I and II can be seen as two-dimensional problems of the theory of elasticity, which are divided as symmetric and skew-symmetric, respectively, with respect to the crack plane [24]. Moreover, mode III can be seen as a two dimensional pure shear (or torsion) problem, thus we need to analyze it in the z

direction as well, when referring to Figure 5 for notation. The resulting stress and displacement fields, omitting the higher order terms, are given below [17, 24]:

Mode I:

$$\left\{ \begin{array}{l} \sigma_{xx} = \frac{K_I}{\sqrt{2\pi r}} \cos\left(\frac{\theta}{2}\right) \left[1 - \sin\left(\frac{\theta}{2}\right) \sin\left(\frac{3\theta}{2}\right) \right] \\ \sigma_{yy} = \frac{K_I}{\sqrt{2\pi r}} \cos\left(\frac{\theta}{2}\right) \left[1 + \sin\left(\frac{\theta}{2}\right) \sin\left(\frac{3\theta}{2}\right) \right] \\ \sigma_{zz} = \nu(\sigma_{xx} + \sigma_{yy}) \\ \tau_{xy} = \frac{K_I}{\sqrt{2\pi r}} \sin\left(\frac{\theta}{2}\right) \cos\left(\frac{\theta}{2}\right) \cos\left(\frac{3\theta}{2}\right) \\ \tau_{xz} = 0 \\ \tau_{yz} = 0 \\ u = \frac{K_I}{G} \sqrt{\frac{r}{2\pi}} \cos\left(\frac{\theta}{2}\right) \left[1 - 2\nu + \sin^2\left(\frac{\theta}{2}\right) \right] \\ v = \frac{K_I}{G} \sqrt{\frac{r}{2\pi}} \sin\left(\frac{\theta}{2}\right) \left[2 - 2\nu - \cos^2\left(\frac{\theta}{2}\right) \right] \\ w = 0 \end{array} \right. \quad (4)$$

Mode II:

$$\left\{ \begin{array}{l} \sigma_{xx} = -\frac{K_{II}}{\sqrt{2\pi r}} \sin\left(\frac{\theta}{2}\right) \left[2 + \cos\left(\frac{\theta}{2}\right) \cos\left(\frac{3\theta}{2}\right) \right] \\ \sigma_{yy} = \frac{K_{II}}{\sqrt{2\pi r}} \sin\left(\frac{\theta}{2}\right) \cos\left(\frac{\theta}{2}\right) \cos\left(\frac{3\theta}{2}\right) \\ \sigma_{zz} = \nu(\sigma_{xx} + \sigma_{yy}) \\ \tau_{xy} = \frac{K_{II}}{\sqrt{2\pi r}} \cos\left(\frac{\theta}{2}\right) \left[1 - \sin\left(\frac{\theta}{2}\right) \sin\left(\frac{3\theta}{2}\right) \right] \\ \tau_{xz} = 0 \\ \tau_{yz} = 0 \\ u = \frac{K_{II}}{G} \sqrt{\frac{r}{2\pi}} \sin\left(\frac{\theta}{2}\right) \left[2 - 2\nu + \cos^2\left(\frac{\theta}{2}\right) \right] \\ v = \frac{K_{II}}{G} \sqrt{\frac{r}{2\pi}} \cos\left(\frac{\theta}{2}\right) \left[-1 + 2\nu - \sin^2\left(\frac{\theta}{2}\right) \right] \\ w = 0 \end{array} \right. \quad (5)$$

Mode III:

$$\left\{ \begin{array}{l} \sigma_{xx} = 0 \\ \sigma_{yy} = 0 \\ \sigma_{zz} = 0 \\ \tau_{xy} = 0 \\ \tau_{xz} = -\frac{K_{III}}{\sqrt{2\pi r}} \sin\left(\frac{\theta}{2}\right) \\ \tau_{yz} = \frac{K_{III}}{\sqrt{2\pi r}} \cos\left(\frac{\theta}{2}\right) \\ u = 0 \\ v = 0 \\ w = \frac{K_{III}}{G} \sqrt{\frac{2r}{\pi}} \sin\left(\frac{\theta}{2}\right) \end{array} \right. \quad (6)$$

The concept of the stress intensity factor is not only a way of quantifying the amplitude of the crack tip singularity, but also a way to describe the initiation of crack growth or fracture.

Typically, the stress intensity factor in mode I is denoted by K_{IC} , and it stands for the fracture toughness, which is the ability of a material to resist fracture when a crack is already present. The IC subscript indicates that this is the critical stress intensity factor value for the mode I, and this parameter is determined through standardized tests. In fatigue problems, an important parameter is the $\Delta K = K_{max} - K_{min}$, which is basically the difference between the maximum and minimum values of K in a cyclic loading scenario.

Most industrial materials in reality exhibit elastic-plastic behavior, thus the elastic crack tip field is valid only when plasticity is confined to a small region [17].

2.2.2 Fatigue crack growth

When a material is subjected to a cyclic loading, even with $\sigma < \sigma_Y$, a crack can form due to surface imperfections, stress concentration, vacancies and many other similar defects within the material. The crack is formed due to the cumulative microscopic damage that arises from the repeated stress cycles.

During the crack propagation phase, each loading cycle can accumulate more and more damage in the crack, and since the crack tip is in a plastic zone, the deformation is permanent, leading to a progressively bigger crack. Between 1960 and 1970, Paris et al. [27, 28] showed that fracture mechanics was an essential tool for the characterization of cracks and crack growth, proposing the renowned Paris Law for the characterization of fatigue crack growth rate under small constant amplitude cyclic load [17].

considering a crack length of a and a number N of cycles, then Paris law is used to determine the rate of fatigue crack growth, and it is written as follows:

$$\frac{da}{dN} = C(\Delta K)^m \quad (7)$$

Here C and m are material constants. Paris law represents the stable growth region of a fatigue crack, and in the log scale, this law indicates a linear behavior. In Figure 6 we can see the different crack growth regimes as ΔK varies. In addition, in Figure 7 we can observe the evolution of the crack through the load cycles.

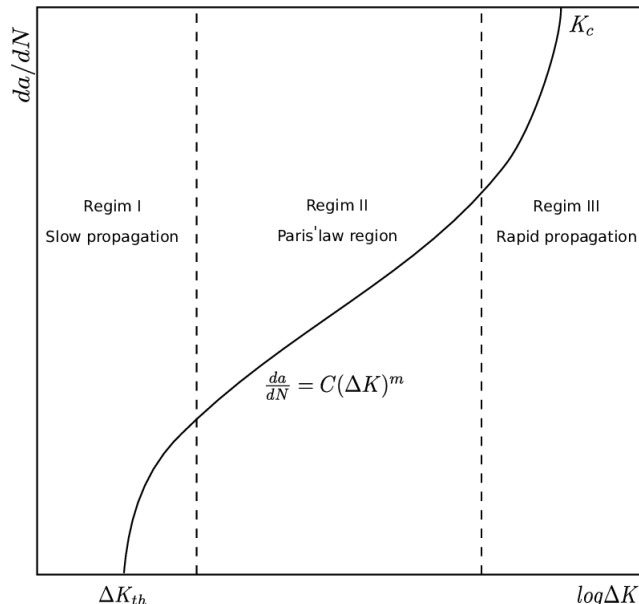


Figure 6: Crack growth regimes according to the Paris Law. Credits to [14].

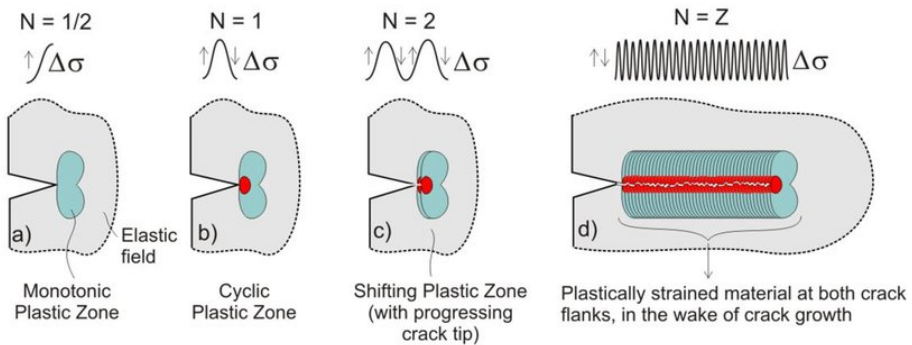


Figure 7: Schematic view of crack growth evolution through the load cycles. Credits to [29].

The stress intensity factor increases as the crack grows, leading to a final catastrophic failure when ΔK exceeds the mateial's fracture toughness. This represents the final stage of the crack growth, as it leads to the final fracture.

Different stages of fatigue life can be identified when looking in the evolution of the stress amplitude through all cycles in a fatigue test, when conducting strain-controlled push pull tests, with $\sigma_{max} = -\sigma_{min}$. Consider Figure 8, extracted from [17]. This figure illustrates the different stages of fatigue life.

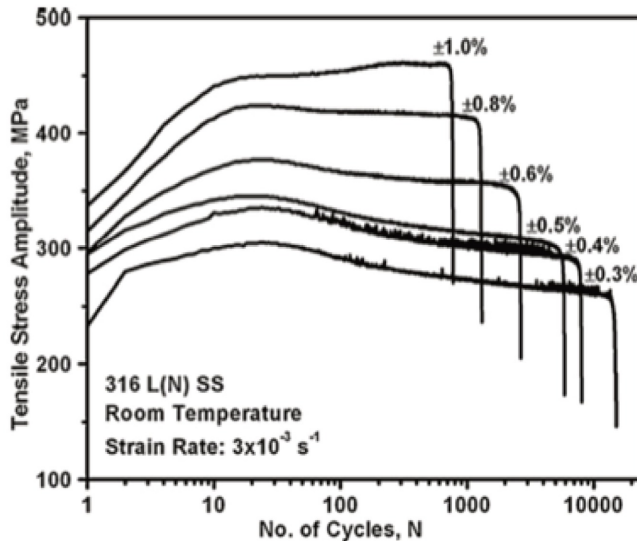


Figure 8: Experimental data on the cyclic hardening and softening phenomena in the 316L stainless steel, in strain-controlled cyclic tests. Credits to [17].

After repeated cyclic loads are applied to the material, we can see from the figure that there is an increase in the measured stress amplitude $\Delta\sigma/2$ in the early fatigue life. As the stress amplitude increases, the hardening phenomenon takes place, and at the peak it marks a the entering of the maximum hardening stage of fatigue life. During hardening, the material experiences an expressive amount of plastic deformation, with dislocation movement, making the material more resistant to further deforming as consequence of the increase dislocations and strain hardening.

From Figure 8, an initial hardening stage is noticeable, peaking at the maximum hardening stage of fatigue life, which can easily be seen for the smaller strain amplitude tests. After this,

there is a stabilization, where the stress amplitude does not change much. For smaller strain amplitudes, the stress is reduced, entering the softening stage earlier, which is a stage in fatigue life marked by a reduction in the material strength and increase of accumulated damage, leading to crack growth.

An important stage in fatigue life is the half life stage, where the number of cycles is half the total number of cycles needed to attain rupture. It is crucial to understand the material behavior in this stage of fatigue life due to the fact that most real life machinery components are in this stage of fatigue life. Lastly, there is the final fracture stage, where there is a sudden drop in stress and the rupture of the specimen is made evident.

Many factors can influence the crack growth, such as the stress range $\Delta\sigma = \sigma_{max} - \sigma_{min}$, the load frequency, the intrinsic material properties and the environment as well. This is where EAF knowledge comes in hand, as the INCEFA-SCALE project is highly interested in the effects of the environment in the fatigue life of real life components in NPPs, since the environment could alter the fatigue life due to corrosive reactions, temperature induced stress, radiation, among other factors.

These different environment factors can lead to mechanisms that degrade the material's properties, diminishing the components useful lifetime.

One of the main reports on EAF is the NUREG/CR-6909 Revision 1 report [30] issued by the *United States Nuclear Regulatory Commission* (NRC). It provides an evaluation of how environments within *Light Water Reactors* (LWRs) impact the fatigue life of materials in NPPs. The report refines the concept of environmental correction factors, used to correct the fatigue life prediction of materials, accounting for the effects of the environment, being thus essential for real scale projects and designs to ensure safety standards throughout operational life of components. It is a milestone in the regulatory framework, guiding recommendations for the nuclear sector.

2.3 The 316L stainless steel

The material of interest for the INCEFA-SCALE project is the 316L stainless steel, which is a widely used material in the nuclear sector due to its excellent corrosion resistance, mechanical strength, ductility, among other properties. This steel complies with a high number of international standards for materials to be used in the nuclear sector, and it has a record of being used for many years, being a critical material for pressure vessels, heat exchangers and pipes, providing safety and reliability to NPPs. In addition, the 316L stainless steel has low activation properties, thus it does not become as much radioactive when exposed to high levels of radiation, hence its use in nuclear waste storage as well. Its chemical composition can be found in Table 1. Additionally, some of the main mechanical properties of the 316L stainless steel can be visualized in Table 2. More info on the material can be read in [31].

Element	% Present
C	≤ 0.03
Cr	16.50-18.50
Ni	10.00-13.00
Mo	2.00-2.50
Mn	2.00
Si	1.00
N	0.10
P	0.045
S	0.015

Table 1: Chemical composition of the 316L stainless steel. Credits to [31]

	Density at 20°C [kg/m ³]	8000
	Thermal conductivity at 20°C [W/(m·K)]	15
Modulus of elasticity [GPa]	20°C	200
	200°C	186
	400°C	172
	500°C	165
	Specific thermal capacity at 20°C [J/(kg·K)]	500
	Electrical resistivity at 20°C [(\Omega·mm ²)/m]	0.75

Table 2: Reference data on a few physical properties of the 316L stainless steel. Credits to [31].

2.4 The Chaboche Constitutive Model

In 1979, Chaboche, Dang Van and Cordier [32] developed a study focused in the 316L stainless steel, proposing an elastic-plastic constitutive model with mixed non-linear isotropic and kinematic hardening [17]. This same model is also able to account for the history effect in materials, and the equations describing the model will be discussed briefly. It is a widely used model to study materials under cyclic loading, being it an extension of classical plasticity theories found in the literature, as it adds different mechanisms to take into account the hardening and softening effects. All equations of the Chaboche constitutive model are presented in Table 3

In essence, the strain ε is decomposed in two contributions, being them the elastic contribution ε^e and the plastic contribution ε^p . It is important to remember that the strain itself is a second order tensor as well as the stress tensor σ , meaning that the components of ε can be written as ε_{ij} , being i and j the indices to indicate the direction of the strain component.

In the equations, s stands for the deviatoric stress tensor, while X is the backstress tensor, which itself represents the kinematic hardening.

The backstress tensor can be decomposed as a sum of components, and each one's temporal evolution can be written as

$$\dot{X}_i = \frac{2}{3}C_i(p)\dot{\varepsilon}^p - \gamma_i X_i \dot{p}$$

In this equation, C_i and γ_i stands for the kinematic hardening modulus and the recovery coefficients, respectively, being both material specific parameters. C_i controls the rate of hardening, while γ_i controls the dynamic recovery rate.

The equations describing the kinematic hardening modulus and the recovery coefficients can be seen in sequence. The parameters k and w are coefficients of the model, and we consider $(k, w) = (1, 0)$ throughout this study. Meanwhile, b is the material constant that controls the isotropic hardening, being present in the kinematic hardening equations as well. Moreover, \dot{p} and $\dot{\lambda}$ stands for the equivalent plastic strain rate and the plastic multiplier, respectively. When considering the Von Mises plasticity criterion, $\dot{p} = \dot{\lambda}$.

In addition, we have that C_i^∞ and γ_i^∞ are the kinematic hardening modulus and recovery coefficients when $p \rightarrow \infty$. Considering the Isotropic hardening, R stands for isotropic hardening modulus.

The model contained in Table 3 accounts for the history effect in the 316L steel, as highlighted in the Non-linear isotropic hardening section, where the usual isotropic hardening described by $R(p) = R_\infty + (R_0 - R_\infty)e^{-bp}$ is replaced. In addition, the field threshold presented is also to account for the history effect, because otherwise a the Von Mises plasticity criterion would have been considered. A more in depth description of the model and its numerical implementation can be read in [33], an official document from the `code_aster` documentation.

Strain partition	$\varepsilon = \varepsilon^e + \varepsilon^p$
Hooke's law	$\sigma = \frac{E\nu}{(1+\nu)(1-2\nu)} Tr(\varepsilon^e) I_d + \frac{E}{(1+\nu)} \varepsilon^e$
Field threshold	$f(\sigma, X, p) = J_2(\sigma - X) - (R(p) + R_0) \leq 0$ with $J_2(\sigma - X) = \sqrt{\frac{3}{2}(s - X) : (s - X)}$ and $s = \sigma - \frac{1}{3}Tr(\sigma)I_d$
Plastic flow	$\dot{\varepsilon}^p = \dot{\lambda} \frac{\partial f}{\partial \sigma} = \frac{3}{2} \dot{\lambda} \frac{s - X}{J_2(\sigma - X)}$ $f = 0$
Non-linear kinematic hardening	$X = \Sigma(X_i)$ $\dot{X}_i = \frac{2}{3} C_i(p) \dot{\varepsilon}^p - \gamma_i X_i \dot{p}$ with $C_i(p) = C_i^\infty (1 + (k - 1)) e^{-wp}$ $\gamma_i(p) = \gamma_i^0 (a_\infty + (1 - a_\infty)) e^{-bp}$ and $\dot{p} = \sqrt{\frac{2}{3} \dot{\varepsilon}^p : \dot{\varepsilon}^p}$ where i represents each kinematic hardening component
Non-linear isotropic hardening	$\dot{R} = b(Q - R)\dot{p}$ $Q(q) = Q_0 + (Q_m - Q_0)(1 - e^{-2\mu q})$ $F = \frac{2}{3} J_2(\varepsilon^p - \xi) - q \leq 0$ $d\xi = \frac{1-\eta}{\eta} dqn^*$ <p>n^* corresponds to the normal direction of surface F</p>

Table 3: Breakdown of Chaboche elastic-plastic cyclic model equations. Table extracted from [17].

In this work, the history effect is used only in a section where different parameter sets for the Chaboche constitutive model are compared, regarding experimental hysteresis cycles. The main focus will be on determining the adjusted, or optimal, parameter set to the Chaboche constitutive model without history effect.

2.5 Important measures

In order to continue the work, it is important to clearly illustrate two important mechanical quantities that are going to be computed many times in this report, which are the Von Mises equivalent stress and strain.

The Von Mises criterion can be formulated in terms of its equivalent stress σ_{VM} , where $\sigma_{VM} < \sigma_Y$. Its expression extracted from [34] is

$$\sigma_{VM} = \sqrt{\frac{3}{2} s_{ij} s_{ij}} = \sqrt{\frac{(\sigma_{xx} - \sigma_{yy})^2 + (\sigma_{yy} - \sigma_{zz})^2 + (\sigma_{zz} - \sigma_{xx})^2 + 6(\tau_{xy}^2 + \tau_{yz}^2 + \tau_{zx}^2)}{2}} \quad (8)$$

Here $s_{ij} = \sigma_{ij} - \frac{1}{3}Tr(\sigma)\delta_{ij}$, being δ_{ij} the kronecker delta. This is the same deviatoric stress tensor from the equations describing the Chaboche constitutive model. It is a fairly common

practice to combine all stress components into a single equivalent magnitude. In addition, the Von Mises equivalent strain extracted from [34] is

$$\varepsilon_{VM} = \sqrt{\frac{2}{3}\text{dev}(\varepsilon)_{ij}\text{dev}(\varepsilon)_{ij}} \quad (9)$$

Here $\text{dev}(\varepsilon)_{ij} = \varepsilon_{ij} - \frac{1}{3}\text{Tr}(\varepsilon)\delta_{ij}$ is the deviatoric strain tensor. The Von Mises equivalent strain is often called the equivalent plastic strain, which was denoted as p in the equations describing the Chaboche constitutive model. It is a quantity to describe the magnitude of work hardening in any given material. In a similar fashion to σ_{VM} , it combines all components into a single scalar quantity, which makes it easy to compute and simplify the post-treatment operations.

3 Computational tools

This section is dedicated to briefly introduce the numerical software used in this work, as much of the study is dedicated to building a reliable numerical model to simulate real life behavior or real-scale specimens under cyclic loads, for the interest of the INCEFA-SCALE project.

It is important to say that the software used in this work is developed by EDF and for the interest of EDF workers, meaning that interpreting the results in order to replicate them in other numerical software involves also comprehending how to implement certain aspects of the developed model, with key differences in syntax and implementation logic.

3.1 Salome Meca

In the present work, we rely heavily on the use of the Salome Meca software. As briefly presented in the introduction, Salome Meca is a an open source software that combines two powerful open source tools for numerical simulations on solid mechanics, which are Salome [5] and `code_aster` [6]. The Salome Meca software has been developed by EDF and CEA *Research and Development* (R&D) teams, being it a part of the larger Salome platform, integrating a wide variety of tools, for CAD development, meshing, pre and post-processing, creating a very helpful environment for the user. In addition to the Salome software, we have the `code_aster` finite element solver, a powerful tool to conduct numerical analysis on a broad range of physical phenomena, ranging from structural mechanics, to thermal and fluid simulations as well.

Moreover, `code_aster` has the capacity to solve multi-physics problems, coupling different physical phenomena in more complex problems, such as thermo-mechanical simulations.

In addition, Salome Meca can integrate Python, C++, C or Fortran code [35]. This way, conducting parametric studies and uncertainty quantification works with Salome Meca is not as difficult, since it can be easily implemented using Python's wide range of libraries. If desired, `code_aster` is also compatible with complementary codes written in Fortran.

The ease of implementation for complementary codes with Salome Meca is extremely useful for automating diverse tasks or even mesh generation, enabling the creation of more complex workflows. Finally, it is also possible to use Python or other computational languages to couple the `code_aster` solver with other numerical solvers, enabling richer studies.

4 Fundamentals of evolutionary algorithms in multi-objective optimization

In order to search for the best combination of Chaboche constitutive model parameters and to enhance the quality of the finite elements results obtained during this work, a multi-objective optimization campaign had to be done. Thus, the theory behind the whole process is to be presented in this section. Throughout this section, major inspiration was given by the chapter two of [9], as it is a very didactic work for those with no basis on the subject. In addition, some parts of the text used is also contained [8], which is a research project report written by the same author of the current work. Some changes in notation have been introduced to make the subject clearer for the reader. In addition to the introductory text on multi-objective optimization, a thorough explanation of the *Non-Dominated Sorting Genetic Algorithm II* (NSGA-II) algorithm [7] is presented, as it is the main evolutionary algorithm used in this research.

4.1 Deterministic multi-objective optimization

Consider a set of input parameters as being a *Design of Experiment* (DoE), and every DoE can be used to compute a number of output results. From this data, it is possible to compute statistical measures and consider them as *Objective Functions* f_i , $\forall i \in \mathbb{N}^*$ or *Constraint Functions* g_i , $\forall i \in \mathbb{N}^*$, where the constraints take the form $g_i \leq 0$. Since the current research does not deal with constrained optimization, we are only going to consider the objective functions.

Every DoE has its own *Design Vector* \mathbf{x} , which contains the output results computed from the input parameters contained in the DoE. Moreover, we consider that every DoE resides in the *Design Space* χ . For example, a DoE $a \in \chi$ will have a design vector named \mathbf{x}_a , which contains the output data, measured considering the parameters contained in a .

In order to compute the objective functions for a DoE, we must use the design vector as argument, so it is reasonable to collect these statistical measures in vectors, which resides in the objective space. Consider that \cdot_f represents a vector obtained by evaluating the respective design vector using the objective functions of a given problem. This vector is going to be called the objective vector. Therefore, given a DoE $a \in \chi$, we have a design vector \mathbf{x}_a and thus, by considering m objective functions, we have an objective vector $a_f \in \mathbb{R}^m$, given by the following equation:

$$a_f = \begin{Bmatrix} f_1(\mathbf{x}_a) \\ f_2(\mathbf{x}_a) \\ f_3(\mathbf{x}_a) \\ \vdots \\ f_{m-1}(\mathbf{x}_a) \\ f_m(\mathbf{x}_a) \end{Bmatrix} \quad (10)$$

We are going to consider that $a_f \in \mathbf{X} \subset \mathbb{R}^m$, where \mathbf{X} is the set containing all objective vectors, named the objective space. By considering that we want to minimize multiple objective functions, then it is necessary to rank the DoEs in such a way that we can find the best, or optimal, designs.

Consider two vectors $w, v \in \mathbb{R}^n$. The classical Pareto dominance is presented, using specific notation that must be preserved:

$$\begin{aligned} w \succ v \text{ (} w \text{ dominates } v \text{)} &\iff \forall j \in \llbracket 1, n \rrbracket, w_j \leq v_j \text{ and } \exists j \in \llbracket 1, n \rrbracket, w_j < v_j \\ w \succ\! \succ v \text{ (} w \text{ strictly dominates } v \text{)} &\iff \forall j \in \llbracket 1, n \rrbracket, w_j < v_j \\ w \sim v \text{ (} w \text{ is indifferent to } v \text{)} &\iff w \not\succ v \text{ and } v \not\succ w \end{aligned} \quad (11)$$

This dominance rule can be extended to compare two DoEs $\alpha, \beta \in \chi$ under the optics of their objective vectors.

Knowing that all DoEs resides in the design space χ and all objective vectors reside in the objective space \mathbf{X} , we define the set $\mathbb{P}(\mathbf{X})$ as being the set containing all the *Pareto-Optimal* designs in χ , naming it the *Pareto Front* of the problem with respect to \mathbf{X} . We can formally define the Pareto front in the non-constrained scenario as follows:

$$\mathbb{P}(\mathbf{X}) = \{\alpha \in \chi \mid \nexists \beta \in \chi, \beta_f \succ \alpha_f\} \quad (12)$$

In Equation 12, α_f and β_f are the objective vectors of $\alpha, \beta \in \chi$. In essence, the Pareto front collects the best DoEs in a multi-objective scenario, where a compromise between getting better results in one objective rather than others is always present. The Pareto-optimal designs are the only ones that are not dominated among all designs. In the following figure, an example of a Pareto front in a bi-objective optimization scenario can be seen.

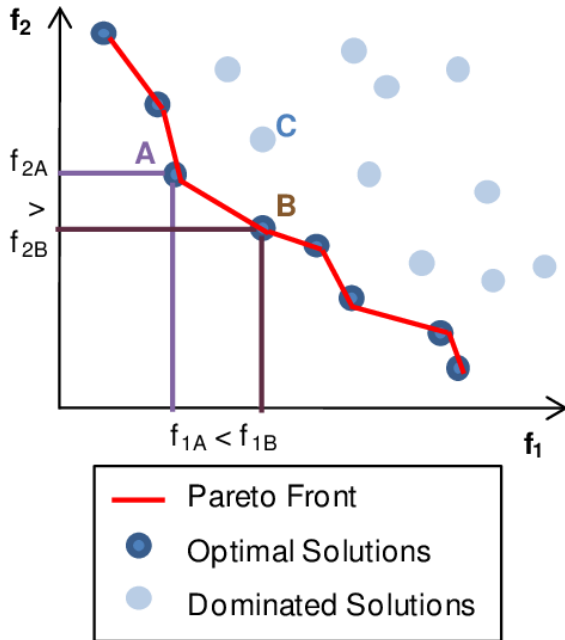


Figure 9: Example of a Pareto front in a bi-objective optimization problem. Credits to [36].

In summary, a deterministic multi-objective optimization problem with m objectives, for $m \in \mathbb{N}^*$, is described by the following:

$$\begin{aligned} \text{minimize: } \alpha_f &= \{f_1(\mathbf{x}_\alpha), f_2(\mathbf{x}_\alpha), \dots, f_m(\mathbf{x}_\alpha)\}^T \in \mathbf{X} \subset \mathbb{R}^m \\ \text{by changing: } \alpha &\in \chi \end{aligned} \quad (13)$$

By changing the DoEs, we obtain new input parameters to compute the design vectors \mathbf{x} , thus obtaining new objective vectors to analyze in objective space \mathbf{X} . The main point of a multi-optimization problem is to search the Pareto-optimal designs.

One important point is that this is a simplistic way to summarize multi-objective optimization. We can have also constrained multi-objective problems, where we introduce inequality constraint functions in the form $g(\mathbf{x}) \leq 0$ or equality constraint functions, such as $h(\mathbf{x}) = 0$, which would lead to a more complex problem in general because we would have to analyze the feasibility of solutions. For the purposes of this work, these details are not highlighted, as we do not deal with constraint functions.

4.2 Evolutionary algorithms

4.2.1 Introduction to evolutionary algorithms

When dealing with multi-objective optimization problems, it is fairly common to deal with conflicting objectives, and the complexity of the problems is very high. To deal with this gamma of mathematical problems, metaheuristics have gained great acceptance in the research field, and among the several metaheuristics currently available, evolutionary algorithms are some of the most popular ones [37]. Evolutionary algorithms are designed to emulate the development of a population based on the same principles of natural selection, where the crossover of genetic information and mutation generate different individuals. These algorithms promote the survival of the fittest for new generations, depending on the objectives of the problem. In the context of a multi-objective optimization problem, the genes are the input parameters, or decision variables, of each design in the design space.

A special attention must be given to not mistake an evolutionary algorithm with a genetic algorithm, although they are pretty similar. In fact, genetic algorithms are a subset of evolutionary algorithms, meaning that all genetic algorithms are evolutionary algorithms, but not the other way around. Typically, genetic algorithms works with a binary encoding of the input parameters to represent the DoEs in design space χ and focus on the use of crossover and mutation as the main operators to explore the design space. Meanwhile, evolutionary algorithms rely on a wider variety of representations for the designs and the field of evolutionary algorithms is broader, in the sense that the mechanisms for which an initial population evolves depends a lot on the application involved and the algorithm used. Genetic algorithms were first developed by John Holland [38] in 1975, and his work was a landmark, since he was able to demonstrate how to model complex adaptation mechanisms computationally, and these notions evolved to the field of evolutionary algorithms, enabling researchers to solve highly non-linear optimization problems. More on genetic algorithms can be read on [39].

A great example of the use of evolutionary algorithms to provide high performance and unconventional solutions in complex engineering scenarios is that of the evolved antenna from NASA's Space Technology 5 (ST5) mission [40, 41]. A figure of one of the prototypes of the antenna launched to space in the ST5 mission is displayed below.

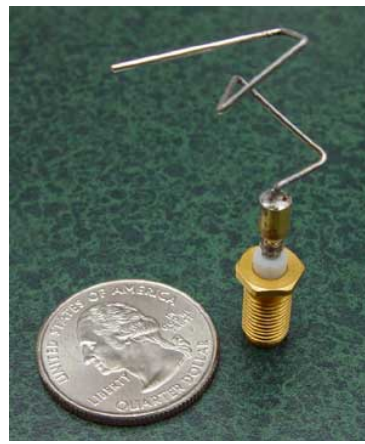


Figure 10: One of the evolved ST5-33-142-7 antenna prototypes developed by NASA for the Space Technology 5 (ST5) mission. Credits to [40].

4.2.2 Motivation

Methods to approach multi-optimization problems have been around since the 1950s and a wide variety of methodologies to approach multi-optimization problems have been developed. Some notable examples are the weighted sum method [42] that converts a multi-objective problem into

a single-objective problem, *Particle Swarm Optimization* (PSO) [43] that explores the design space by assigning positions and velocities to a number of particles in χ , and updating it, among many others. Many mathematical programming methods have limitations, such as the difficulty of determining the Pareto front when its shape is concave or disconnected, while others require differentiability of the objective and constraint functions, in constrained multi-objective scenarios, in addition to sometimes generate only a single solution from each run. [37].

In contrast, evolutionary algorithms uses a population of designs, commonly named individuals, meaning that several Pareto-optimal designs can be found in a single run of the algorithm. Moreover, evolutionary algorithms are suited to determine the shape of the Pareto front even in concave or discontinuous cases. Additionally, in evolutionary algorithms there is no need to know the gradient of the objective functions, meaning that they are good algorithms when dealing with black-box optimization, as well as with noisy, discontinuous and non-differentiable objective functions. Finally, evolutionary algorithms are easy to implement and they are great to maintain diversity of solutions, due to crossover and mutation operators for every generation, and this is of pivotal importance to exploration of the design space and avoiding premature convergence.

4.2.3 Non-dominated Sorting Genetic Algorithm II (NSGA-II)

In the context of the present research, time constraints were significant. To tackle this issue, a very well known multi-objective optimization evolutionary algorithm was selected to conduct the research in the context of the INCEFA-SCALE project's interests. The selected algorithm is the NSGA-II algorithm, which is a modified version of the NSGA algorithm [44]. The main differences between these two algorithms is that the NSGA non-dominated sorting algorithm has a computational complexity of $\mathcal{O}(MN^3)$, where M and N stands for the number of objectives and the population size, respectively, while NSGA-II has a non-dominated sorting algorithm with computational complexity of $\mathcal{O}(MN^2)$ [7], due to the fact that NSGA-II sorting algorithm is elitist and conserves the already found Pareto-optimal designs through generations [45]. The NSGA-II algorithm is a very solid algorithm and widely used in many real world engineering applications.

A brief summary of the NSGA-II algorithm is presented, inspired by the reference article that introduces this algorithm [7]. For more in depth understanding, it is advised to read the reference article in details. At first, consider a multi-objective optimization problem where each DoE $x \in \chi$ has n parameters to define it. A population P_0 of N individuals, with $N \in \mathbb{N}^*$, is generated, by using an assigned *Probability Density Function* (PDF) to determine each one of the n parameter values of each DoE. A recommended approach is to use a uniform PDF to ensure random individuals are selected in a uniform manner. Then, all m objective functions are computed for all N individuals, for $m \in \mathbb{N}^*$.

The second step is to sort all individuals in objective space \mathbf{X} , using the non-domination criteria. Each individual is assigned a rank, based on how close they are to the Pareto front. Rank 1 individuals are the non-dominated ones, the rank 2 individuals are the ones that are dominated only by rank 1 individuals, and so forth. To collect all individuals of each rank in unique sets, the fronts \mathcal{F} are used, such that \mathcal{F}_i contains all individuals of rank i . In a naive manner, one could identify \mathcal{F}_1 by comparing all individuals between themselves, which would require $\mathcal{O}(MN)$ comparisons for each individual, summing to $\mathcal{O}(MN^2)$ comparisons to find \mathcal{F}_1 . The same procedure can be done to find \mathcal{F}_2 , and at most it would require $\mathcal{O}(MN^2)$ computations. Therefore, in the worst case scenario, it would be necessary to realize $\mathcal{O}(MN^3)$ computations, with $\mathcal{O}(N)$ storage required. In the NSGA-II algorithm, however, another path is used, to reduce the computational burden associated with the non-dominated sorting.

For each individual, two values are computed: the domination count n_p , which is the total number of individuals dominating an individual p , and S_p , the set of individuals dominated by p . Doing this requires $O(MN^2)$ comparisons. In \mathcal{F}_1 , the domination count is equal to zero for

all individuals, thus for each DoE p with $n_p = 0$, we visit S_p and we reduce the domination count of every DoE by one, and let us call q the DoE inside S_p , without loss of generality. In doing so, if for q the domination count becomes zero, we collect this individual in a separate list Q . The individuals inside Q forms \mathcal{F}_2 , and this same procedure gets repeated to identify \mathcal{F}_3 and so on, until all fronts are identified.

For each DoE with rank equal to 2 or higher, $n_p \leq N - 1$, therefore each DoE p will have its n_p value reduced at most $N - 1$ times, until it becomes zero. When n_p reaches zero, this DoE will not be visited anymore, as the rank will have been assigned. Since there are a maximum possible value of $N - 1$ individuals like this, then the total computational complexity is of $\mathcal{O}(N^2)$, meaning that the overall complexity of the sorting algorithm is of $\mathcal{O}(MN^2)$, and hence the name of fast non-dominated sorting algorithm. It is important to highlight that although the time complexity has been reduced, the storage requirement increases to $\mathcal{O}(N^2)$. The pseudocode representing the procedure of the fast non-dominated sorting algorithm extracted from [7] is presented in Algorithm 1.

Algorithm 1 Fast Non-Dominated Sorting Algorithm

```

1: for  $p \in P$  do
2:    $S_p \leftarrow \emptyset$ 
3:    $n_p \leftarrow 0$ 
4:   for  $q \in P$  do
5:     if  $p \succ q$  then
6:        $S_p \leftarrow S_p \cup \{q\}$  {Add  $q$  to the set of solutions dominated by  $p$ }
7:     else
8:        $n_p \leftarrow n_p + 1$  {Increment the domination counter of  $p$ }
9:     end if
10:   end for
11:   if  $n_p = 0$  then
12:      $p_{\text{rank}} \leftarrow 1$ 
13:      $\mathcal{F}_1 \leftarrow \mathcal{F}_1 \cup \{p\}$ 
14:   end if
15: end for
16:  $i \leftarrow 1$ 
17: while  $\mathcal{F}_i \neq \emptyset$  do
18:    $Q \leftarrow \emptyset$  {Used to store the members of the next front}
19:   for  $p \in \mathcal{F}_i$  do
20:     for  $q \in S_p$  do
21:        $n_q \leftarrow n_q - 1$ 
22:       if  $n_q = 0$  then
23:          $q_{\text{rank}} \leftarrow i + 1$ 
24:          $Q \leftarrow Q \cup \{q\}$ 
25:       end if
26:     end for
27:   end for
28:    $i \leftarrow i + 1$ 
29:    $\mathcal{F}_i \leftarrow Q$ 
30: end while

```

In order to maintain a good diversity of individuals in every generation, NSGA-II implements the crowding distance measure for every individual, which is a way to quantify the density of

neighbors around each individual with the same rank. The less crowded is the region around a point, then the higher is the crowding distance, making this individual preferable, specially when exploring new regions in objective space. This way, the algorithm is not only ranking individuals by their ranks, but also by their crowding distance inside each rank, so that this can information can be used to select individuals with same rank, and thus a mating pool can be created for the crossover operation that follows.

Let d_i be the crowding distance of individual i , with $i \in \llbracket 1, \ell \rrbracket$, being ℓ the number of individuals inside the front being analyzed. Initially, we set $d_1 = d_\ell = \infty$, and then we can compute the crowding distance $\forall i \in \llbracket 2, \ell - 1 \rrbracket$. Initially the crowding distance is set to zero, then we must visit each one of the m objectives involved in the multi-objective problem and compute the relative distance between the values of the objective functions of the neighboring individuals, which we'll name $\xi_{k,i}$ here, for the k th objective function. Being $f_{k,i}$ the k th objective function for the i th individual, consequently the expression of $\xi_{k,i}$ is given by the following equation:

$$\xi_{k,i} = \frac{f_{k,i+1} - f_{k,i-1}}{\max(f_k) - \min(f_k)} \quad (14)$$

Thus, the final crowding distance of each individual other than individual 0 and individual N is given by the following expression:

$$d_i = \sum_{k=1}^m \xi_{k,i} \quad (15)$$

A figure illustrating in a two-dimensional objective space is displayed right below. This is a way to clearly see what the crowding distance quantifies, as it is intimately related to how close one individual is to their neighboring points.

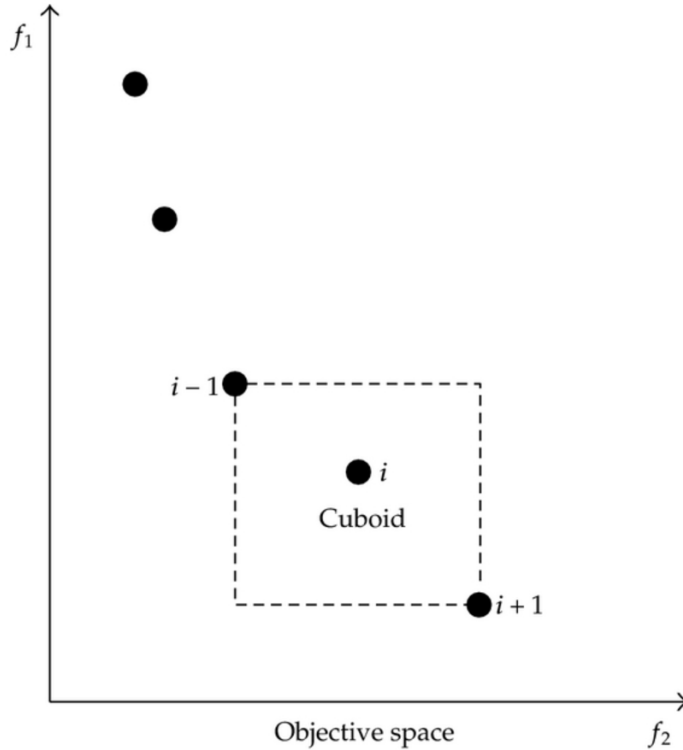


Figure 11: Visual representation of the procedure to compute the crowding distance for the i th individual inside a rank. Credits to [46]

After sorting individuals within the ranks based on their crowding distance in a descending order, the mating pool is created for the crossover operations. For such, NSGA-II uses binary tournament selection based on the rank and the crowding distance. Two individuals are compared, and the individual with lower rank is preferable. If the ranks are equal, consequently the individual with higher crowding distance is preferable.

Genetic operators are used for the crossover and the mutation steps. Many different operators are available for these purposes, but the most popular ones are presented, as they are used in the implementation of the NSGA-II algorithm in this work.

For the crossover operator, the *Simulated Binary Crossover* (SBX) [47, 48] operator is used. It is a real-parameter crossover operator based on the same principles of the single-point binary crossover. It relies on the use of a hyper-parameter named the distribution index η_{SBX} , which controls the spread of the offspring by shaping the PDF of the offspring solutions. It is a way to shape how closely related is the offspring to the parent designs. A low value of η_{SBX} means that there the offspring PDF is flattened, resulting in a higher probability of generating a offspring that is far from the parents, thus promoting exploration of design space. In contrast, a high η_{SBX} results in the opposite, thus favoring the exploitation of the design space and refining the already studied regions in χ . For each pair of individuals selected to undergo crossover, a random number between 0 and 1 is generated, and if this number is smaller than the probability of crossover, than the crossover operator is applied. This is a way to also control the genetic variability of a population.

The main advantages of the SBX are that it has been found to work well in many test problems with a continuous design space [49], in addition to maintaining good diversity of solutions and also providing a control of the exploration of the design space, by the altering the η_{SBX} value. The main disadvantage of the SBX crossover operator is that it is computationally expensive, as it requires more complex calculations. Further details on the principles of the SBX operator can be found in [47, 48, 49].

Regarding the mutation operator, polynomial mutation has been selected. As with any other mutation operator, it promotes exploration by randomly selecting individuals of the population and changing its genes, based on a probability of mutation. This operator is designed to work well with real-valued parameters.

For each individual of the population, a random number between 0 and 1 is generated, and if this number is smaller than the probability of mutation, than this individual is selected to undergo mutation, similarly to what happens in the crossover stage. The selected genes to be mutated are perturbed according to a polynomial distribution, and this distribution depends on the distribution index η_{PM} , which is a user-defined hyper-parameter.

The distribution index plays a major role in the shape of the polynomial distribution used to induce perturbation of the genes, similarly to η_{SBX} . Low values of η_{PM} results in a flatter PDF, and thus the new mutated gene is likely to be far from the original value, promoting exploration of design space and preventing premature convergence, thus avoiding local optima. Meanwhile, a high value of η_{PM} will make the PDF sharper, making the difference between the new and the old gene smaller, promoting exploitation instead of exploration. A brief explanation on the functioning of the polynomial mutation can be found in [50].

After creating a new population out of the initial one, with the same N number of individual, we combine both populations into a total population of size $2N$. Let Q_0 be the offspring population generated from P_0 , and $R_0 = P_0 \cup Q_0$ the total population at iteration 0. Within R_0 , we initially apply Algorithm 1, to perform the non-dominated sorting, then we must perform the crowding distance sorting inside every front in order to extract the next parent generation, P_1 , with N individuals again. This can be generalized for any iteration t , as illustrated in Figure 12. The algorithm repeats this procedure until a stopping criterion is met, such as a maximum number of generations or a satisfactory convergence parameter is met.

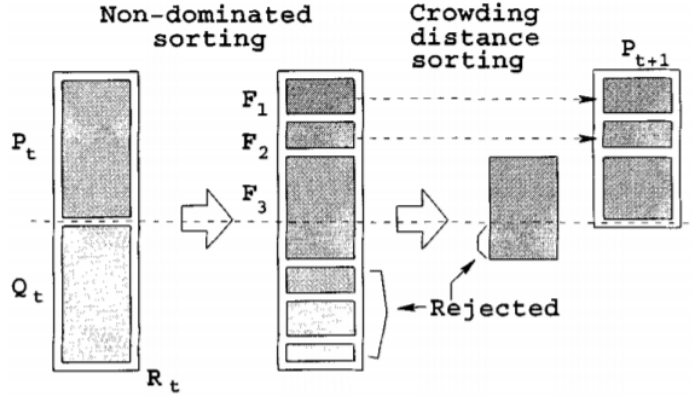


Figure 12: NSGA-II algorithm procedure to extract new generation. Credits to [7].

The pseudocode representing the NSGA-II algorithm procedure is presented in Algorithm 2, and it is an altered version of the one contained in [7], where a maximum number of generations is used as stopping criterion, which is the method used in the continuation of this research as well.

Algorithm 2 NSGA-II Procedure

```

1:  $t \leftarrow 0$  {Set generation counting variable}
2:  $n_{\text{gen}} \leftarrow K$  {Set total number of generations as  $K$ , for  $K \in \mathbb{N}^*$ }
3: while  $t < n_{\text{gen}}$  do
4:   Compute  $Q_t$  from  $P_t$  {SBX and polynomial mutation}
5:    $R_t \leftarrow P_t \cup Q_t$  {Combine parent and offspring population}
6:   Compute  $\mathcal{F} = (\mathcal{F}_1, \mathcal{F}_2, \dots)$  {Algorithm 1}
7:    $P_{t+1} \leftarrow \emptyset$ 
8:    $i \leftarrow 1$ 
9:   while  $|P_{t+1}| + |\mathcal{F}_i| \leq N$  do
10:    Sort  $\mathcal{F}_i$  by crowding distance {Equation 15}
11:     $P_{t+1} \leftarrow P_{t+1} \cup \mathcal{F}_i$ 
12:     $i \leftarrow i + 1$ 
13:   end while
14:   Sort  $\mathcal{F}_i$  by crowding distance {Equation 15}
15:    $P_{t+1} \leftarrow P_{t+1} \cup \mathcal{F}_i[1 : (N - |P_{t+1}|)]$  {Add the first  $(N - |P_{t+1}|)$  elements of  $\mathcal{F}_i$ }
16:    $t \leftarrow t + 1$ 
17: end while

```

4.3 Implementing NSGA-II in the context of this work

Considering the context of the current study, it is advantageous to use such evolutionary algorithm to tackle the problem of determining a set of mechanical parameters of the Chaboche constitutive model, which is the one used in this work, to build a numerical model for which we obtain results that are accurately close to the experimental data, obtained by the contributors of the INCEFA-SCALE project. It is of the interest of all partners of the project to find such a model, in order to obtain reliable results and predictions to study real life 316L steel components behavior within the framework of NPPs, when subjected to EAF.

5 Results and discussion

In the present section, all the results obtained during the internship are presented, as to highlight the work developed at EDF and discuss the results. It is important to emphasize that all experimental data and simulations consider the 316L steel at 300°C and with air as the environment fluid only. Additionally, when dealing with a cyclic loading, we consider a frequency of 1 Hz.

5.1 Notched Specimen

Firstly, notched specimens are studied. Notched specimens are specimens containing special geometric features that are destined to generate stress concentration regions, and this practice is very common when dealing with fatigue life tests. Figure 13 illustrates the geometry of the notched specimens considered in this study. The three design parameters defining the notched specimen are [51]:

- The nominal diameter D , fixed by the laboratory, varying between 6 and 9 millimeters in the frame of the INCEFA-SCALE project;
- The reduced diameter d , controlling the stress concentration between nominal and reduced section;
- The radius of the notch r , governing the triaxiality state in the notch area.

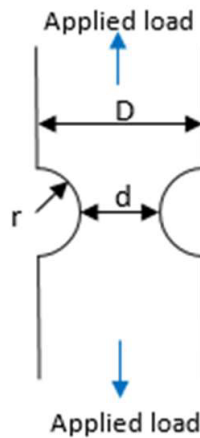


Figure 13: Illustration of notched specimen with its geometrical parameters D, r and d . Credits to [52].

5.1.1 Comparison with INCEFA-SCALE results

Using as reference the progress report [51] written by the INCEFA-SCALE contributors, whose lead author is EDF, we can validate the numerical model developed with `code_aster` by comparing some simulation results with the experimental data and with the simulation results obtained by both CEA and Framatome France, which are two companies contributing in the INCEFA-SCALE project.

The initial validation of the developed `code_aster` framework was given by using the concept of cyclic stress-strain curve, or reduced curve, to simplify the simulations and to conduct them in the same manner Framatome France has conducted. A cyclic stress-strain curve is nothing more than a curve in which every point represents the point of maximum stress for a hysteresis loop with a given strain amplitude $\Delta\varepsilon/2$. Figure 14 illustrates this concept.

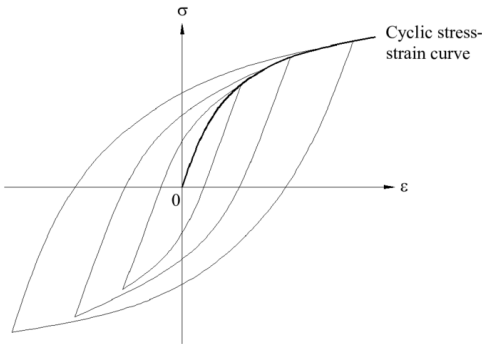


Figure 14: Illustration of the cyclic stress-strain curve concept, used to simplify numerical simulations. Credits to [53].

Conducting numerical simulations on a single traction load being exerted in the piece can reduce the required computational time significantly, as it eliminates the burden associated with the cyclic computations needed to achieve stability. However, it is important to note that this method only works for comparing with experimental measurements taken at the maximum stress level, which would represent the final time step of the simulation.

For this work, two cyclic stress-strain curves were provided for validation of the numerical code and discussion. One is the reduced curve used by Framatome France in their own numerical simulations, and the other one was determined at EDF by using data points in the stress-strain space for different tests and distinct specimens from the contributors of the INCEFA-SCALE project. By gathering these points, two linear fits were built following the least mean squares method, to construct a bi-linear curve. Figure 15 represents the procedure used.

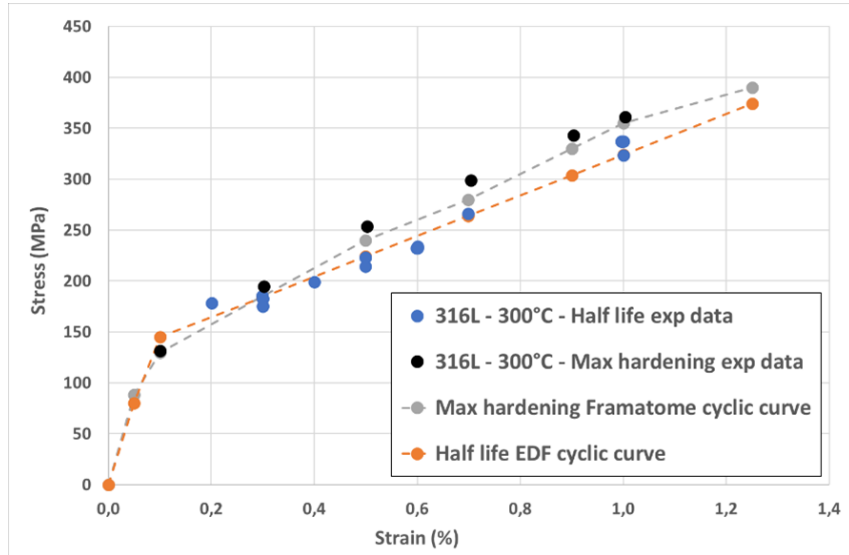
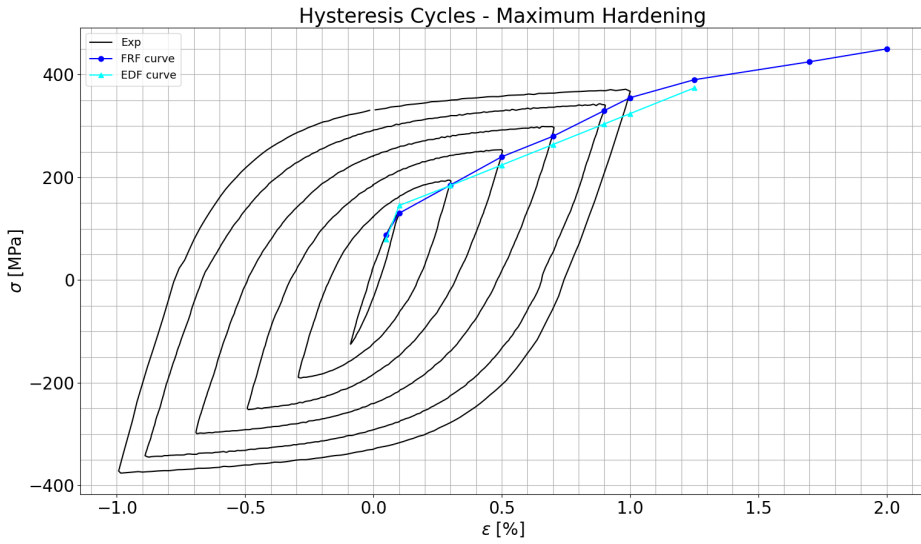
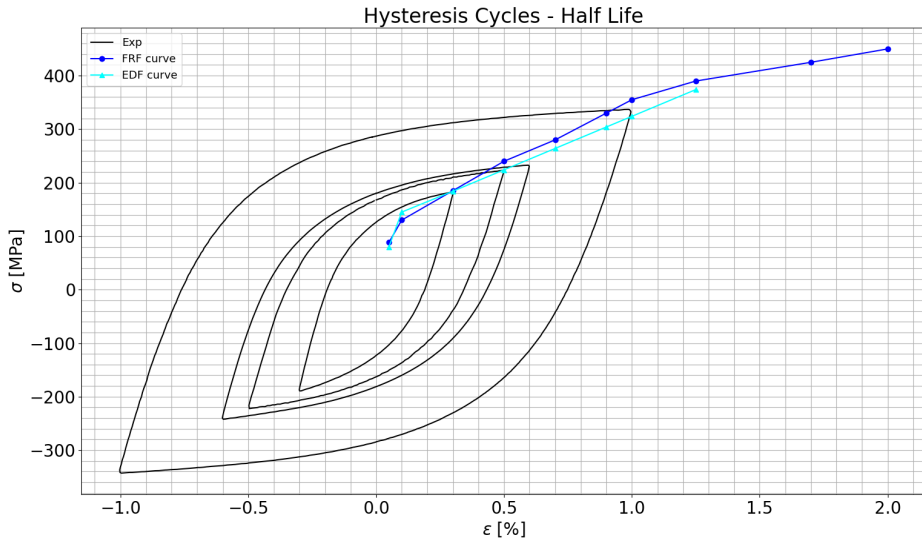


Figure 15: Illustration containing a wide variety of experimental data points from contributors of the INCEFA-SCALE project, used to build the EDF bi-linear cyclic stress-strain curve.

In Figure 16, the cyclic stress-strain curves from Framatome France and EDF are compared with the experimental data on stabilized hysteresis cycles of the the 316L steel with cycles of different $\Delta\varepsilon/2$ values, available at maximum hardening and at half-life stages of fatigue life.



(a) Reduced stress-strain curves provided by Framatome France (FRF) and EDF for the numerical simulations, compared with experimental hysteresis cycles of the 316L steel at maximum hardening stage.



(b) Reduced stress-strain curves provided by Framatome France (FRF) and EDF for the numerical simulations, compared with experimental hysteresis cycles of the 316L steel at half-life stage.

Figure 16: Reduced stress-strain curves provided by Framatome France (FRF) and EDF for the numerical simulations, compared with experimental data in different fatigue life stages.

When defining the material within the `code_aster` syntax, it suffices to include the keyword `TRACTION` with the traction curve as argument, being the traction curve exactly the cyclic stress-strain curve. This is done to introduce non-linear behaviour on the material. In addition, when calling the solver to run the simulation, one should use the non-linear behavior defined by

the keyword `VMIS_ISOT_TRAC`, which considers the Von Mises elasto-plasticity behavior relation with non-linear isotropic strain-hardening. In addition, this mechanical behavior should be made explicit inside the `STAT_NON_LINE` operator, responsible for computing the mechanical quasi-static evolution for non-linear cases. All the needed documentation to better comprehend the operators and the syntax of `code_aster` can be found in the official website [54].

The technical drawings of the complete specimens used in the present work are highlighted in Appendix A. During the numerical campaign however, only the useful section of the specimens are used, as it diminishes the computational burden associated with the simulations and also permits a finer mesh to be used. The specimens considered are from Framatome France, EDF and Kaunas University of Technology (KTU), illustrated in Figures A.1, A.2 and A.3, respectively.

The meshes generated for each geometry were bi-quadratic, as we are dealing with a mechanics finite elements simulation. In addition, quadrilateral elements are better suited for such analysis, as they yield a better accuracy when we consider only mechanical phenomena playing a role in the temporal evolution of the model. In addition, quadrilateral elements can achieve a good accuracy with a smaller number of elements, additionally to being able to better handling element distortion in structured meshes. More on the topic can be read on [55]. The meshes used for the numerical simulations with the cyclic stress-strain curves are illustrated in Figure 17. The red dots in each mesh represent the point in the mesh where the vertical displacement is measured to compare with the results from Framatome France and CEA, that are contained in [51].

In the experimental setup of the fatigue life tests, an extensometer is placed on the side of the specimen, and its position vary depending on the laboratory that conducted the experiment. The important measure to take experimentally is the extensometer gage amplitude at maximum stress, used for further comparisons.

Given an extensometer gage length L , then the position of interest in the numerical model to measure the vertical displacement is at $y = L/2$, being y the vertical axis. After taking the result of vertical displacement at this point, due to the symmetry it suffices to multiply the result by two to obtain the numerical value of the extensometer amplitude.

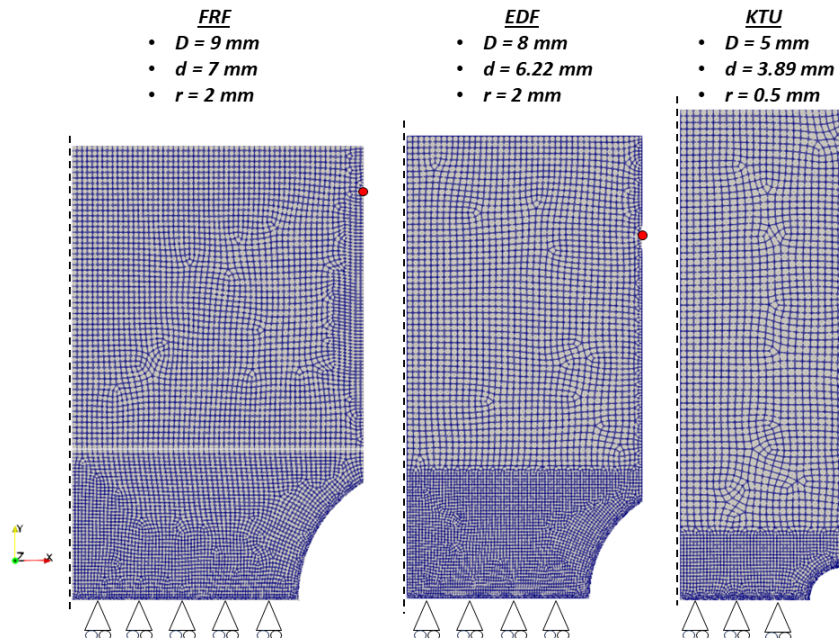


Figure 17: Illustration of the meshes used for the numerical simulations on the notched specimens, together with the respective design parameters defining each geometry. The red dots highlight the position of the extensometer measurement sought.

One can see that the mesh contains only one quarter of the useful section of the specimen, and this was done so that the generated mesh could be as fine as possible. The origin in the frame of reference of each numerical model is the bottom left corner of the mesh, which is located exactly in the middle of the full-scale specimen. The x and y axis are oriented from left to right and from bottom to top, respectively, starting from the designated origin.

Specific boundary conditions were considered, so that the mesh could represent the bulk behavior of the specimen. Firstly, axial symmetry is considered within `code_aster`, by inserting the argument named `MODELISATION = 'AXIS'` inside the `AFFE_MODELE` operator. This ensures that the y axis is the axis of rotational symmetry of the specimen. Moreover, in the bottom edge of every specimen, no displacement is considered in the vertical direction, in order to represent the symmetry with the other half of the specimen.

The tests conducted by the INCEFA-SCALE members aimed at achieving a certain level of Von Mises equivalent strain at the notch root, and thus the tests were piloted by applied load on the specimen, since there was no real way to measure the strain at the notch in the experimental setup. Therefore, the extensometer gage amplitude measure is really the only comparable data. When it comes to the ε_{VM} value obtained at the notch, this is a numerical result and cannot be compared with real life experiments. These tests are called diagnostic tests, and they serve as base for the other labs participating in the project to compare the obtained results.

By using both Framatome and EDF cyclic stress-strain curves, simulations considering a single traction load were conducted, where the force evolves linearly with relation to the time of the simulation, achieving its maximum at $t = 0.25$ s, for $t \in [0, 1]$. The results were obtained for comparison with the ones in [51], which are the experimental results and numerical results from Framatome France and CEA. This preliminary analysis is crucial to validate the code used, and check that `code_aster` has been well implemented, as well as corroborating with the project by validating existing results.

The collection of results can be found in Tables 4 and 5. In these tables, FRF stands for Framatome France. For the tests, the extensometer gage length was of 12 mm, 12.5 mm and 10 mm for the Framatome, EDF and KTU specimens, respectively, meaning that the vertical displacement was measured in the numerical model at $y = 6$ mm, $y = 6.25$ mm and $y = 5$ mm, respectively.

Lab	Step	F [N]	Target $\varepsilon_{VM}[\%]$	$\varepsilon_{VM}[\%]$ -FRF curve	$\varepsilon_{VM}[\%]$ -EDF curve
FRF	-	8908	0.6000	0.6011	0.5956
EDF	1	4737	0.2000	0.2003	0.1773
	2	6108	0.4000	0.4006	0.3511
	3	7147	0.6000	0.5995	0.6009
KTU	1	1521	0.2000	0.2002	0.1961
	2	2107	0.4000	0.4009	0.3446
	3	2447	0.6000	0.6016	0.5440

Table 4: Von Mises equivalent strain results obtained in this work using stress-strain curves.

It is possible to notice that Framatome's curve is better suited to capture the Von Mises equivalent strain at the notch root, however it is important to recall that in the real experimental setup it is not possible to measure the strain at this location. In order to compare the numerical results obtained via *Finite Element Analysis* (FEA) with the experimental measurement for the extensometer amplitude, the relative error was used, and it is computed as in Equation 16. In the relative error equation, Δy stands for the difference between the two symmetrical y coordinates of the specimen, measuring thus the extensometer gage amplitude at maximum stress.

5 RESULTS AND DISCUSSION

Lab	Step	$F[\text{N}]$	Ext. amplitude[mm]	FEA-FRF[51]	FEA-CEA[51]	FEA-FRF curve	FEA-EDF curve
FRF	-	8908	0.0240	0.0257	0.0259	0.02553	0.02177
EDF	1	4737	0.0080	0.0095	0.0112	0.00948	0.00926
	2	6108	0.0126	0.0171	0.0171	0.01732	0.01436
	3	7147	0.0238	0.0272	0.0220	0.02709	0.02356
KTU	1	1521	0.0054	0.0051	0.0058	0.00501	0.00550
	2	2107	0.0100	0.0089	0.0104	0.00891	0.00816
	3	2447	0.0168	0.0125	0.0132	0.01255	0.01063

Table 5: Comparison between extensometer results obtained by INCEFA-SCALE members on diagnostic tests and the results obtained in this work using stress-strain curves.

$$\delta_y = \frac{\Delta y^{\text{FEA}} - \Delta y^{\text{exp}}}{\Delta y^{\text{exp}}} \quad (16)$$

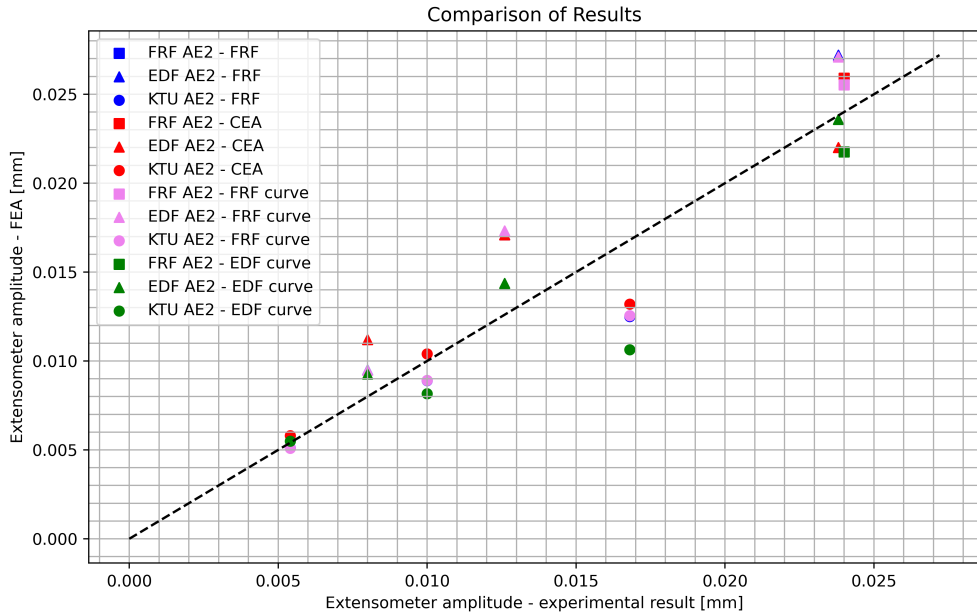
The collection of relative errors computed with relation to the experimental extensometer amplitude measurement can be found in Table 6. We can see that the errors computed with this work's implementation of `code_aster` are fairly close to the ones found with the FEA conducted by Framatome and CEA, especially when comparing the results obtained using the Framatome stress-strain curve and the available ones from [51], which sums up to comparing the third and fifth columns.

Lab	Step	$\delta_y[\%]$ -FRF	$\delta_y[\%]$ -CEA	$\delta_y[\%]$ -FRF curve	$\delta_y[\%]$ -EDF curve
FRF	-	7.08	7.92	6.38	-9.31
EDF	1	18.75	40.00	18.53	15.77
	2	35.71	35.71	37.47	13.96
	3	14.29	-7.56	13.82	-0.89
KTU	1	-5.56	7.41	-5.65	1.80
	2	-11.00	4.00	-10.87	-18.41
	3	-25.60	-21.43	-25.32	-36.71

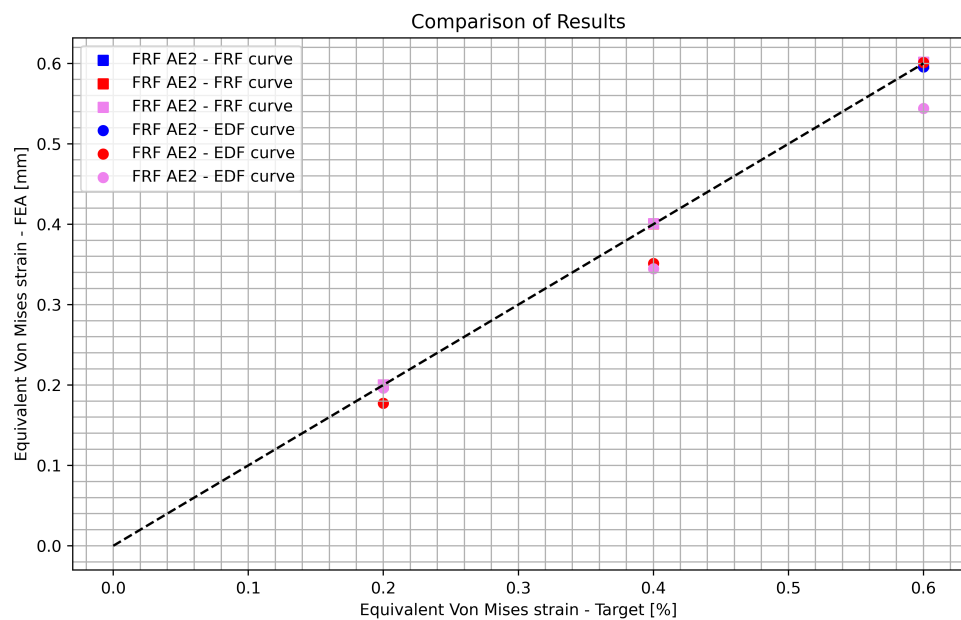
Table 6: Comparison of the relative errors obtained in the FEA simulations for the extensometer amplitude measurement.

An important remark is that although the errors seems to be big, the extensometer measurements are actually very small, then even the slightest change will produce a high error, and there are also associated experimental errors than can play a major role in the comparison. Hence, even with this level of error, the order of magnitude of the FEA results is the same as the experimental measurement. Figure 18 illustrates the proximity of all numerical results and also their accuracy. In this figure, FRF AE2, EDF AE2 and KTU AE2 are the technical nomenclatures of the specimens presented in Figures A.1, A.2 and A.3, respectively. This nomenclature was already in use in official INCEFA-SCALE reports, such as in [51].

The Von Mises equivalent stress and strain in the bottom edge of the specimens can be observed in Figures 19, 20 and 21. Throughout all the numerical simulations conducted in this study, the exponential behavior can be observed in all of them. In addition, when comparing the different steps in the EDF and KTU tests, it is possible to note that the stress grows steeper and steeper, as the maximum load force F increases. In these images, only the Framatome stress-strain curve was considered, as it provided more accurate numerical results.



(a) Comparison of numerical and experimental results of extensometer amplitude in diagnostic tests.



(b) Comparison of numerical results of Von Mises equivalent strain in diagnostic tests.

Figure 18: Comparison of numerical and experimental results of extensometer amplitude and Von Mises equivalent strain, in diagnostic tests.

5 RESULTS AND DISCUSSION

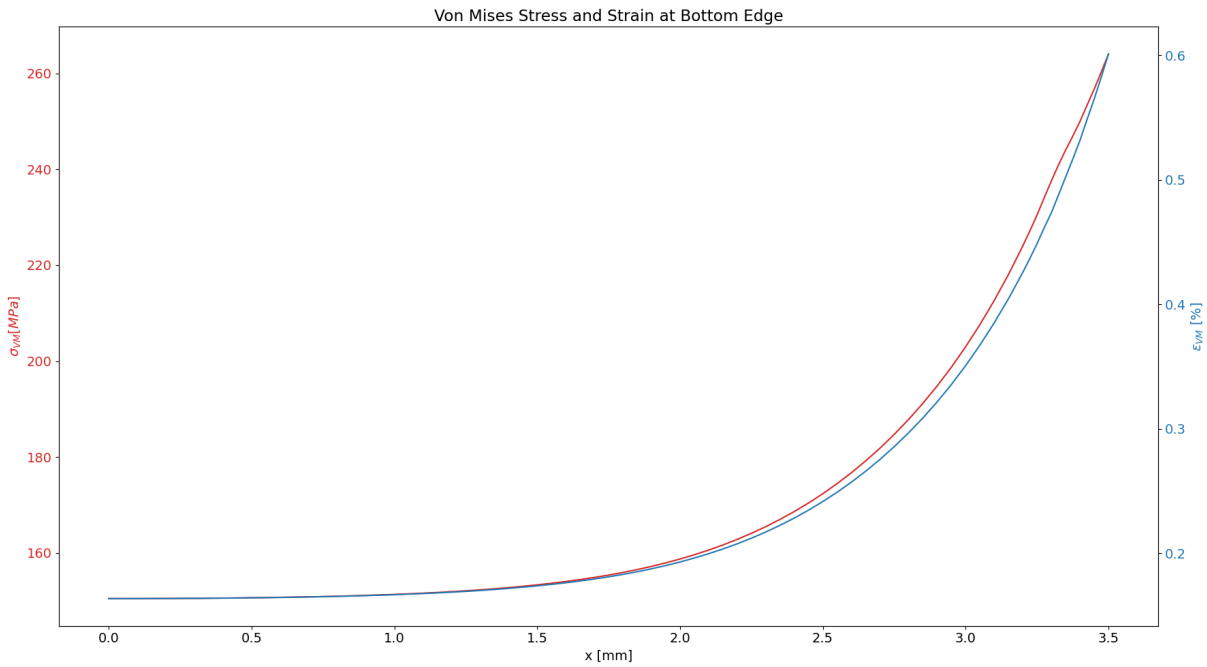
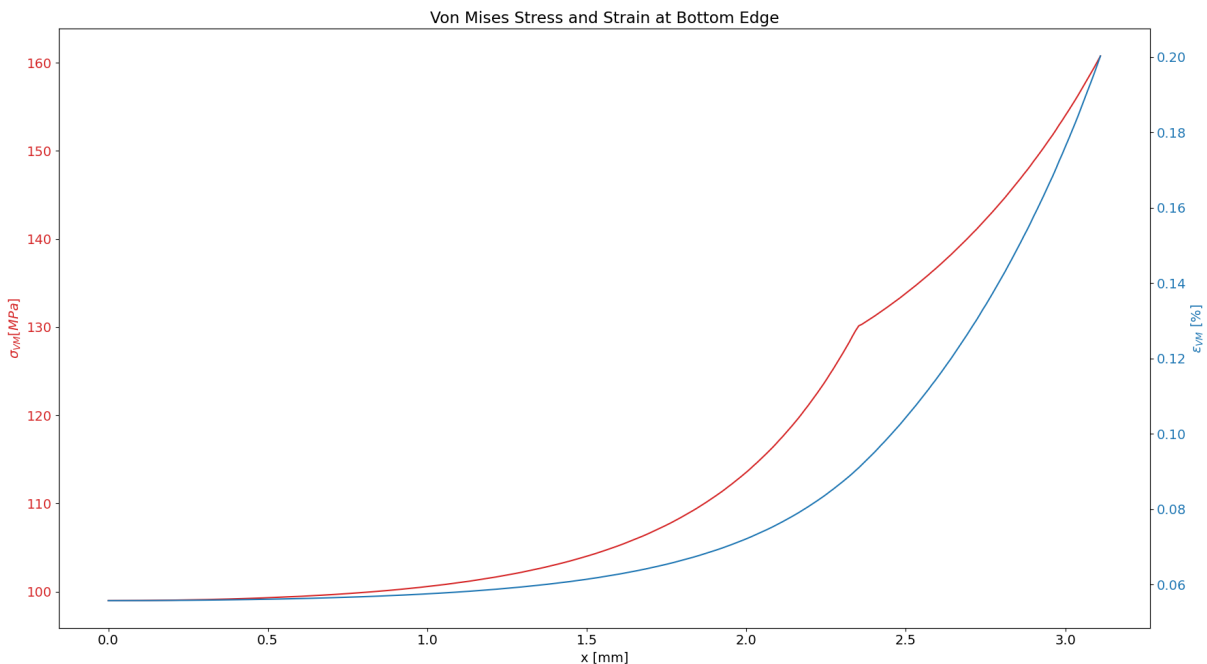
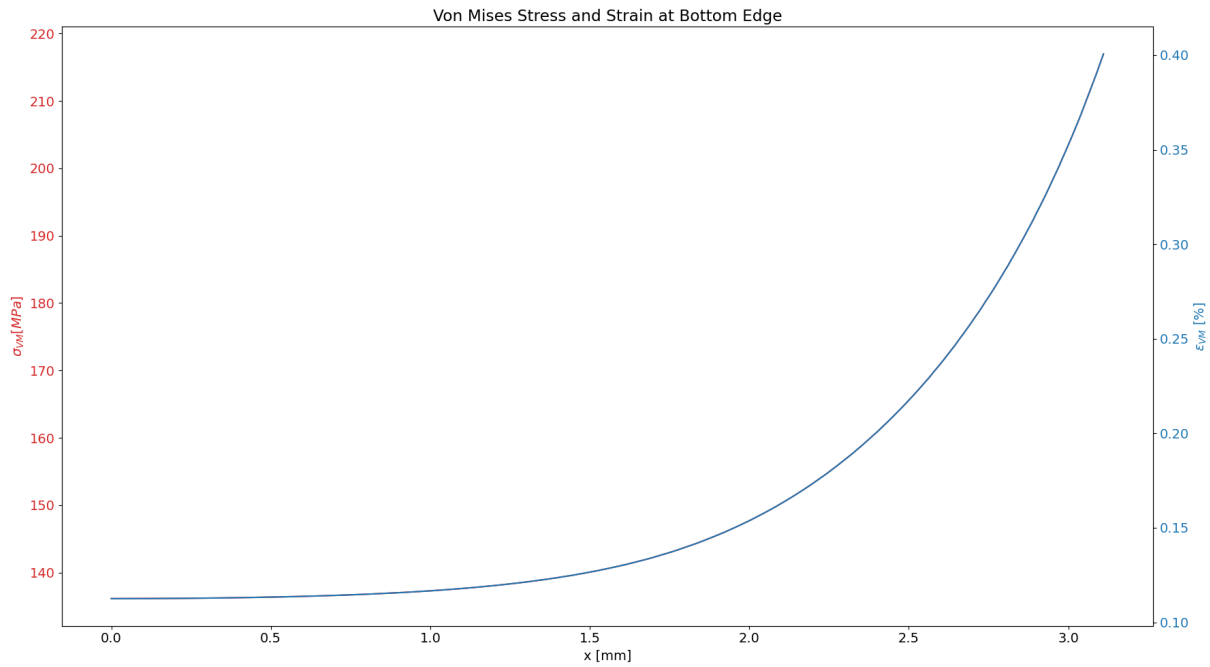


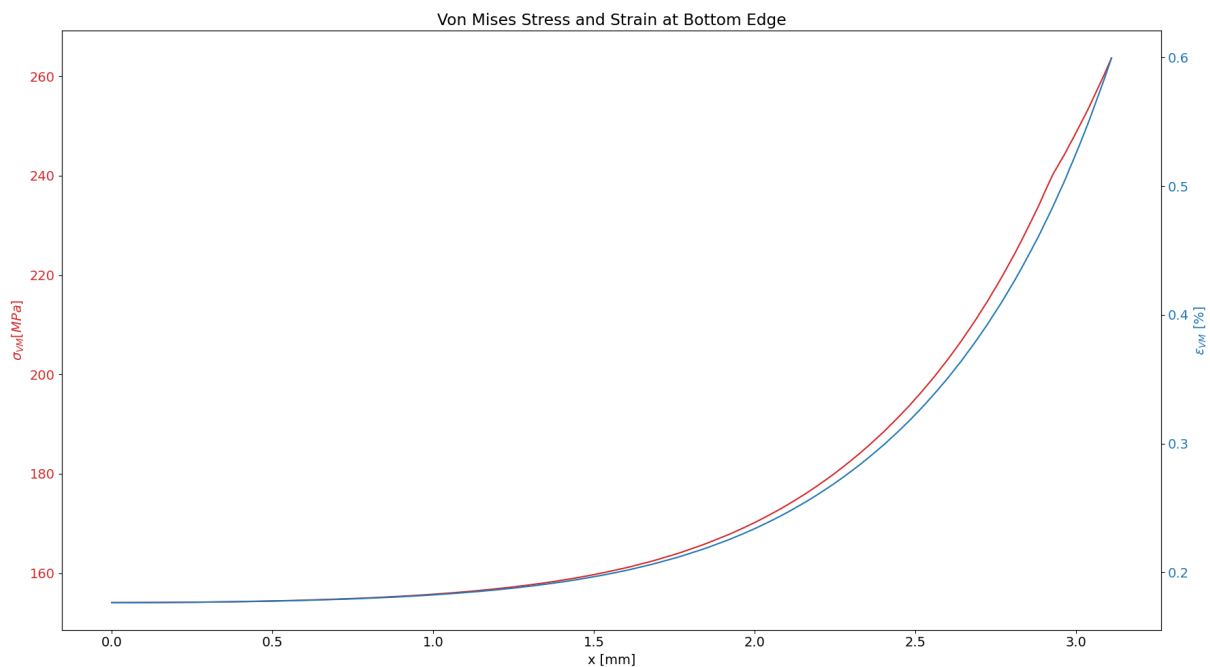
Figure 19: Von Mises equivalent stress and strain at bottom edge for the diagnostic test of the Framatome Specimen.



(a) Von Mises equivalent stress and strain at bottom edge for the diagnostic test of the EDF Specimen in step 1.



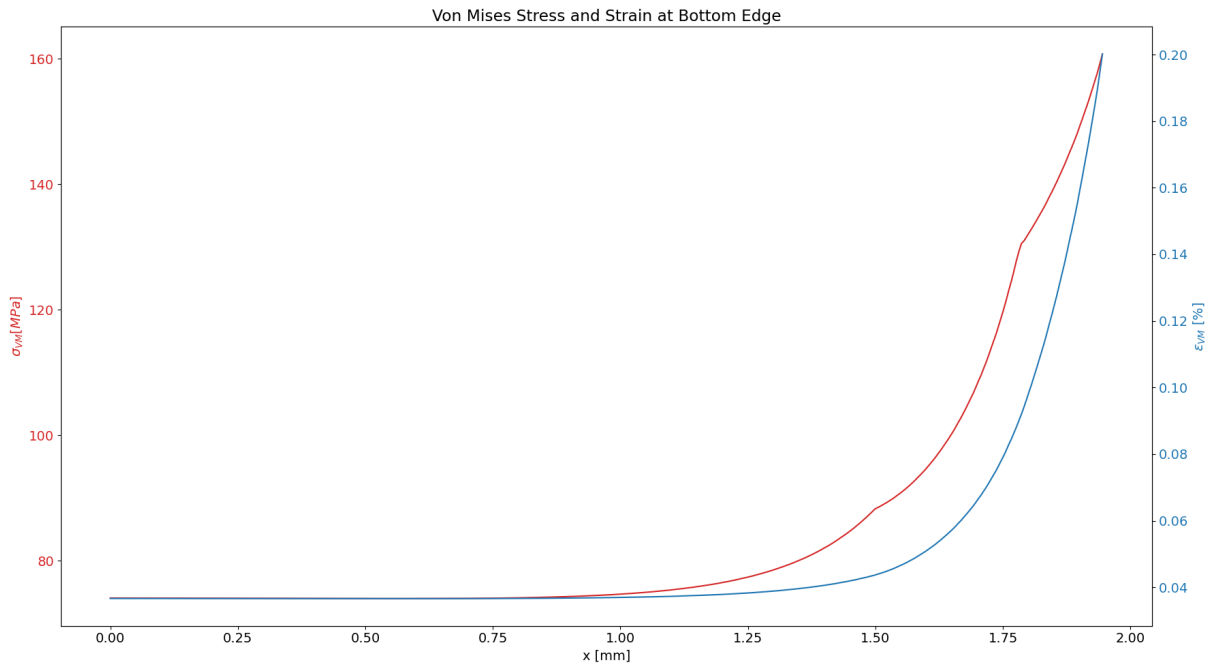
(b) Von Mises equivalent stress and strain at bottom edge for the diagnostic test of the EDF Specimen in step 2.



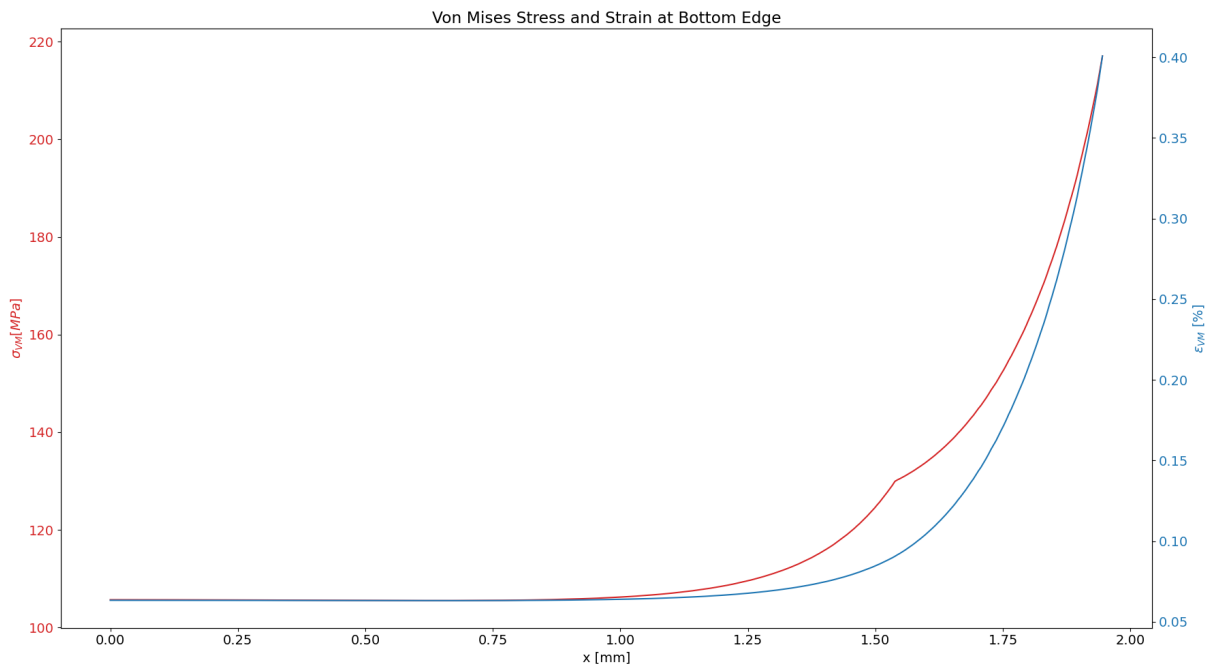
(c) Von Mises equivalent stress and strain at bottom edge for the diagnostic test of the EDF Specimen in step 3.

Figure 20: Von Mises equivalent stress and strain at bottom edge for the diagnostic test of the EDF Specimen in all steps.

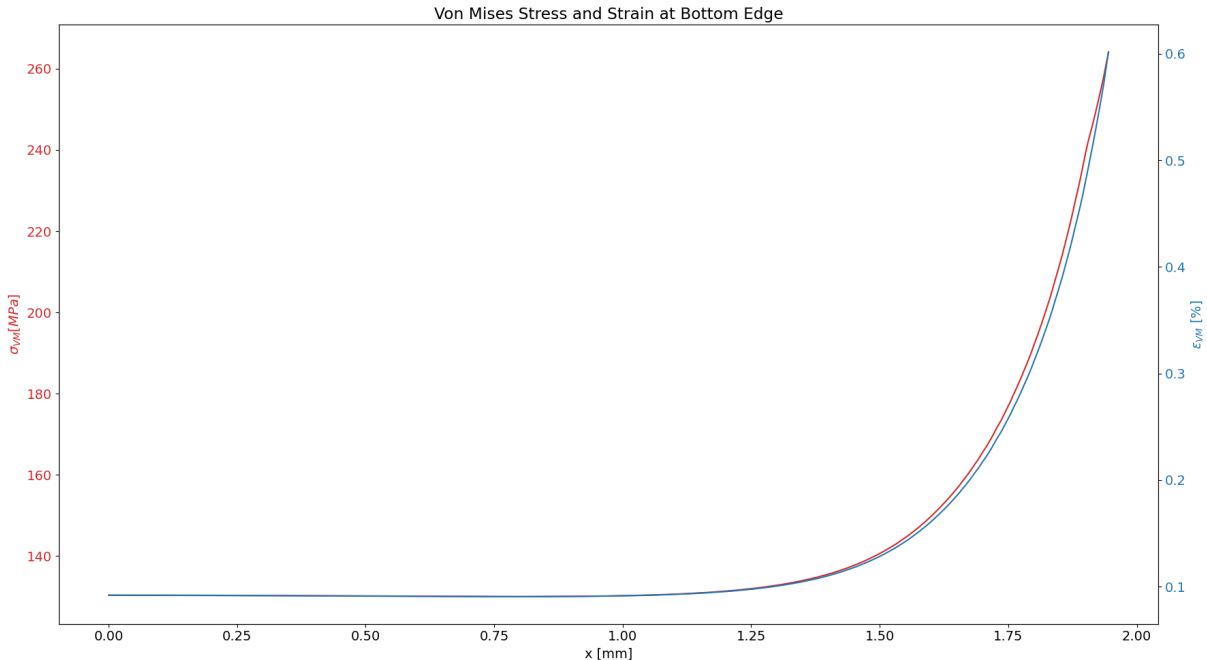
5 RESULTS AND DISCUSSION



(a) Von Mises equivalent stress and strain at bottom edge for the diagnostic test of the KTU Specimen in step 1.



(b) Von Mises equivalent stress and strain at bottom edge for the diagnostic test of the KTU Specimen in step 2.



(c) Von Mises equivalent stress and strain at bottom edge for the diagnostic test of the KTU Specimen in step 3.

Figure 21: Von Mises equivalent stress and strain at bottom edge for the diagnostic test of the KTU Specimen in all steps.

5.1.2 Comparison of studied parameter sets within INCEFA-SCALE

There is a high interest in developing a unique numerical model that can be used for both low and high strain values, instead of having multiple numerical models to represent different states of the studied material depending on the expected deformation. Thus, initial inspiration was provided by the work of Zhang [17], and many simulations were conducted using this numerical model, to understand how well it could describe the mechanical behavior of the 316L steel.

Using the Chaboche constitutive model, a comparison of parameter sets is conducted in order to determine if an existing set of parameters already studied would fit the current work. The parameter sets used are the ones developed by CEA in the INCEFA-SCALE modeling plans report [51] and the Zhang's [17] parameter set. The parameters used are presented in the following table, where the history effect of the Chaboche model is neglected. As a recall, all simulations are considered at 300°C with air as the environment fluid around the specimen. The parameters considered are the Young modulus E , the Poisson's ratio ν , the kinematic hardening modulus C_1 and C_2 , the recovery coefficients γ_1 and γ_2 , the initial value of the isotropic hardening modulus R_0 and the material constant that controls the isotropic hardening b .

It is important to recall that Zhang's parameters have been optimized to describe the behavior of the 316L steel at maximum hardening, while the objective of this numerical study is to determine a good parameter set of the Chaboche constitutive model for the half-life stage of fatigue life. In addition, Zhang's parameter set with the history effect is also considered in this initial moment, using the saturation and initial values of the isotropic hardening parameter Q from the constitutive model. They are denoted as Q_m and Q_0 . In addition, the μ and η parameters that plays a role in the exponential behavior of the evolution of Q are also included. Their values in the Zhang's parameter set are highlighted in Table 8.

In order to compare all the parameter sets presented between themselves, a simple cubic mesh was used, with only one volumetric element. This elementary mesh will further be used, so we will refer to it as the cubic mesh. All the nodes are identified in Figure 22, as the boundary

	Parameters	Zhang	CEA-1	CEA-2	CEA-3	CEA-4
Elasticity	E [GPa]	160	160	160	160	180
	ν	0.3	0.3	0.3	0.3	0.3
Kinematic Hardening	C_1 [MPa]	170000	90000	136000	182000	87000
	γ_1	1500	1000	1200	1600	1000
	C_2 [MPa]	25000	34200	36400	32400	34100
	γ_2	200	214	303.194	303.194	212
Isotropic Hardening	R_0 [MPa]	110	800	5	55	5
	b	10	1	1	0.25	4

Table 7: Comparison of the Chaboche constitutive model parameter sets.

	Parameters	Zhang
History effect	μ	16
	η	1
	Q_0 [MPa]	-50
	Q_m [MPa]	250

 Table 8: History effect parameters extracted from Zhang’s thesis [17]. The Q_m and Q_0 values have been corrected, as they are wrong in [17].

conditions are applied to the nodes. The objective of using such a simple mesh is to reduce the computational time required to run all simulations, since it is necessary to run a numerical simulation with a high number of cycles to ensure stabilization for each strain amplitude $\Delta\varepsilon/2$, for which experimental data is available for comparison.

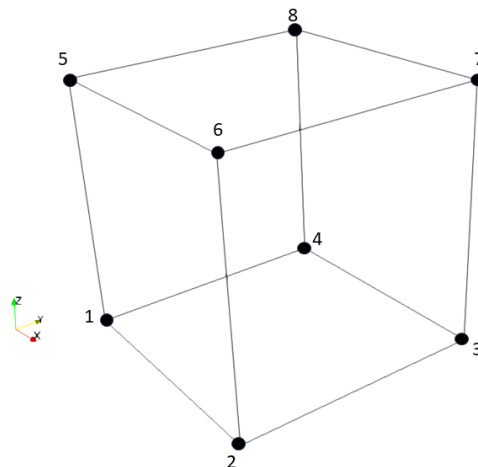


Figure 22: Elementary cube used to compare all the parameter sets used to describe the 316L steel in the numerical simulations, with all nodes identified.

The boundary conditions considered for this simulation campaign were the following:

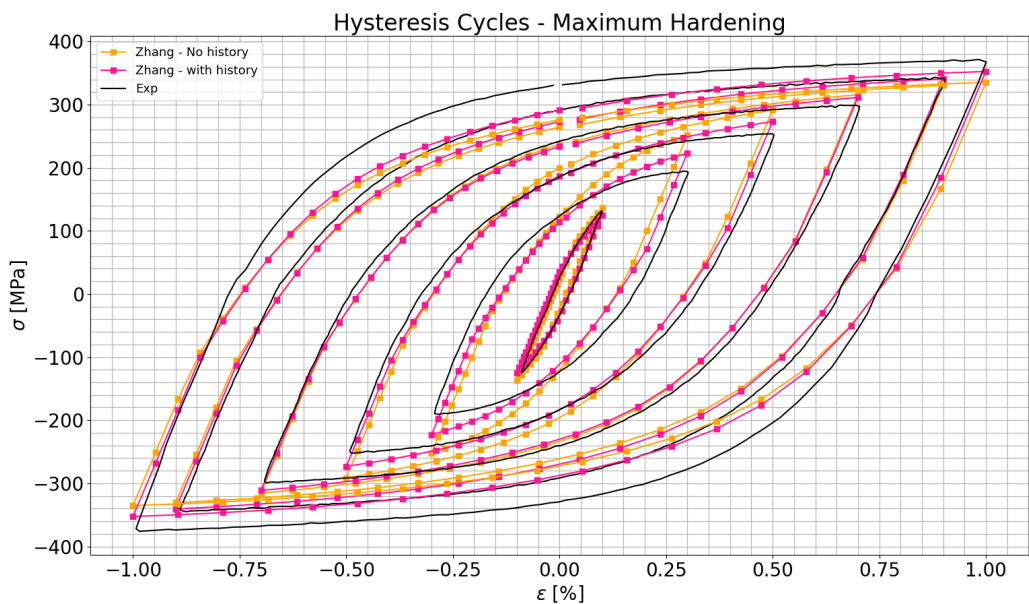
- Nodes 1, 2, 3 and 4: no displacement in the z direction;
- Nodes 1, 2, 5 and 6: no displacement in the y direction;
- Nodes 1, 4, 5 and 8: no displacement in the x direction;
- Nodes 5, 6, 7 and 8: imposed displacement in the z direction.

The strain amplitudes considered for the comparison with all the experimental data are 0.1, 0.3, 0.5, 0.6, 0.7, 0.9 and 1.0%, and since this is a simple test, when referring to the strain, consider ε as the standard notation, but considering the axis orientation, in reality this strain is ε_{zz} . Since this is an elementary cubic volume, each side of the cube has unit length, thus imposing a displacement makes it easy to impose the desired strain, and thus control the test this way. All simulations conducted on the cubic mesh consisted of 100 cycles, in order to guarantee stabilization. A smaller number of cycles could have been used, but the choice of 100 cycles was simply to ensure convergence, since the computational time necessary for these simulations was not high. Firstly, a comparison using Zhang's parameter sets with and without the history effect are presented in figure 23.

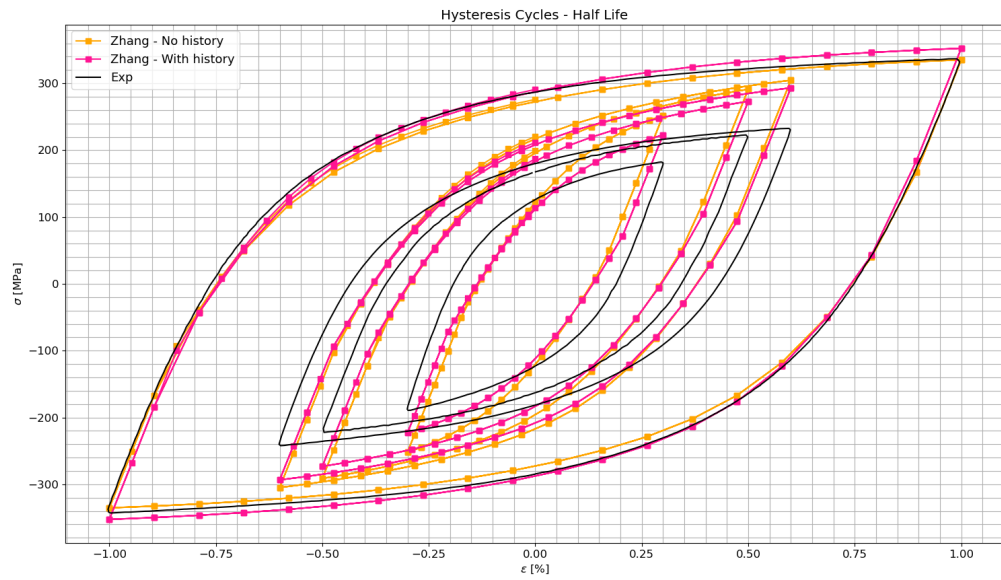
From these results, clearly Zhang's parameters describe the 316L steel at maximum hardening stage more accurately. In the maximum hardening stage, adding the history effect to the mechanical model improves the accuracy of the numerical simulation, however the general shape of the hysteresis loops are still not as accurate for the strain amplitudes of 0.3, 0.5 and 1.0%.

Moreover, at half life stage, both models are not accurate to represent the strain amplitudes of 0.3, 0.5 and 0.6%, but they are both accurate at strain amplitude of 1.0%. Nevertheless, the model without history effect outperformed the one with history effect when comparing with the experimental data with strain amplitude of 1.0%.

Concerning the CEA parameter sets, a comparison was performed to determine which is the best parameter set at maximum hardening and at half life stages of fatigue life. Firstly, all parameter sets were compared to the experimental data at once, and it was observed that the parameter set 1 was not well suited to represent the 316L steel behavior, as shown in Figure 24, so this parameter set will not be considered for further comparisons.

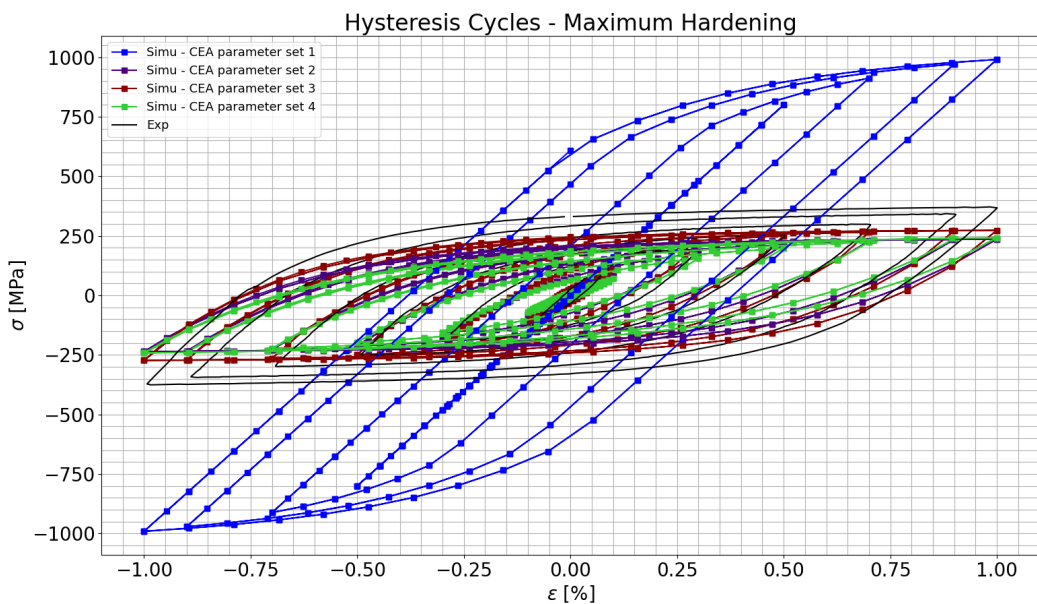


(a) Comparison between Zhang's parameter sets, with and without the history effect, and experimental data at maximum hardening stage of fatigue life.

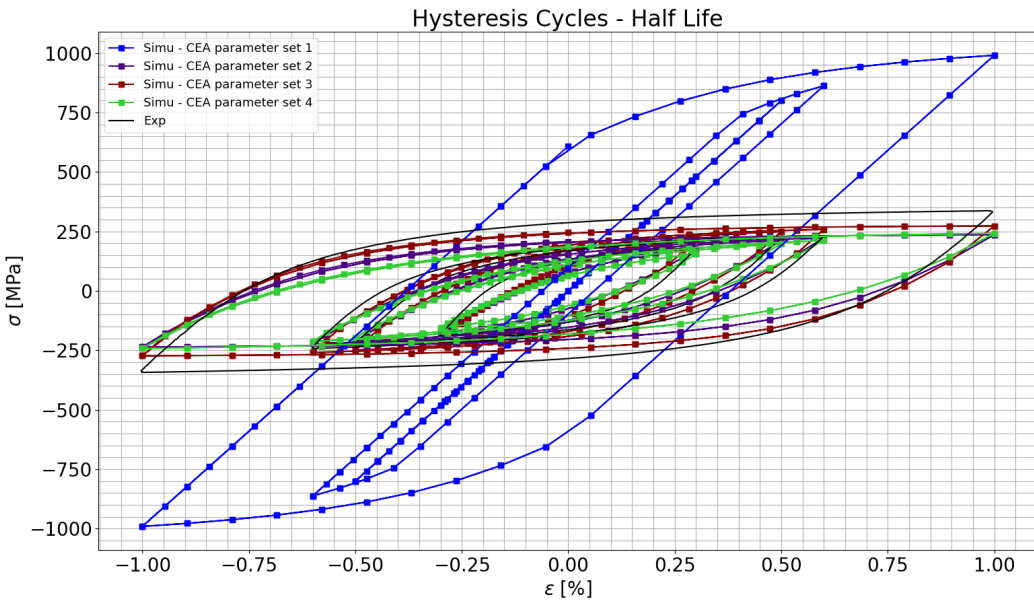


(b) Comparison between Zhang's parameter sets, with and without the history effect, and experimental data at the half life stage of fatigue life.

Figure 23: Figure comparing simulation results with experimental data using Zhang's parameter sets, with and without history effect at different stages of fatigue life.



(a) Comparison between CEA parameter sets and experimental data at maximum hardening stage of fatigue life.



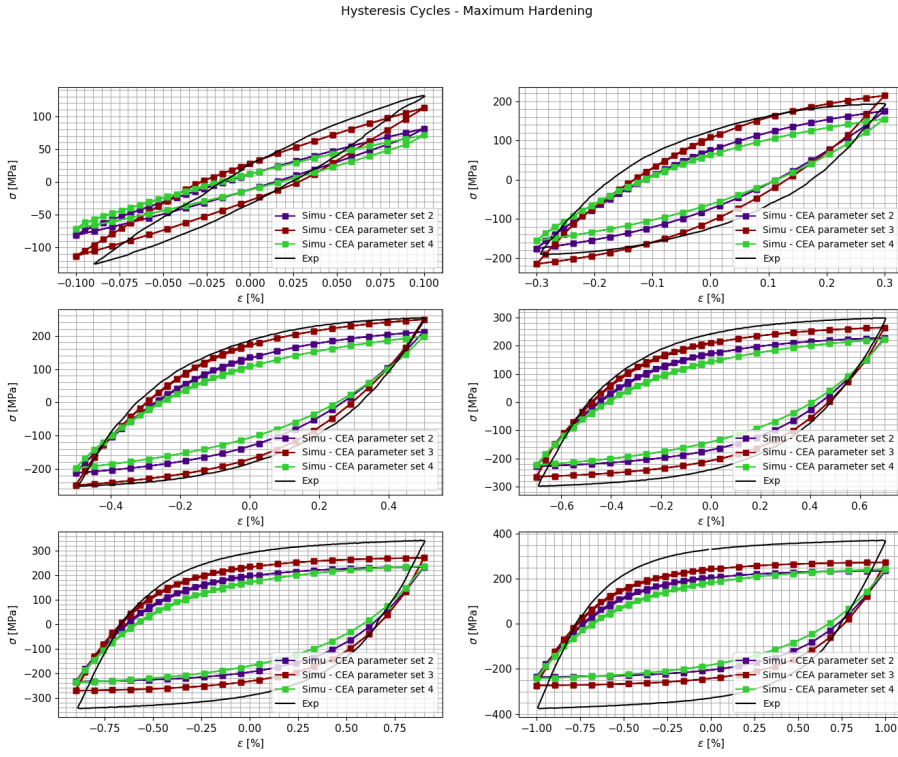
(b) Comparison between CEA parameter sets and experimental data at half life stage of fatigue life.

Figure 24: Figure comparing simulation results with experimental data using CEA parameter sets.

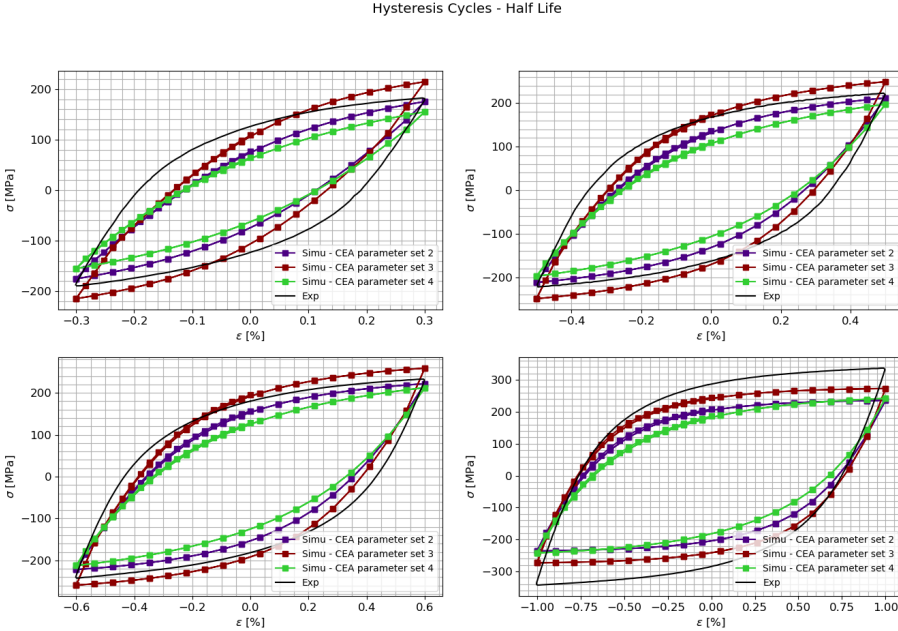
In order to study the performance of each parameter set for all strain amplitude levels at maximum hardening and half life stages, Figure 25 can be used. We can conclude that the parameter set 3 is the most accurate at maximum hardening, while at half life the parameter set 2 is the most appropriate, with the exception of the results at $\Delta\varepsilon/2 = 1.0\%$, where parameter set 3 outperforms the parameter set 2. Nevertheless, the parameter sets that were considered the best for the comparison with Zhang's parameters were parameter set 3 and 2, for the maximum hardening and half life stages of fatigue life, respectively.

From Figure 26, it is possible to compare the best parameter sets for both stages of fatigue life and draw conclusions. At maximum hardening, the Zhang's parameter set with history effect is more accurate than the parameter set 3 proposed by CEA in [51]. Meanwhile, for the half life stage, we see no good agreement between the computational model and the experimental data for all strain amplitudes. What is observed is that either the model is accurate at higher strain amplitudes, or accurate at lower strain amplitudes. This has proven to be a very difficult point of approach perceived by CEA in the modeling progress report [51], since the perfect numerical model would be able to represent the material behavior at different levels of deformation with confidence. However, different mechanisms are involved when dealing with low and high deformation.

5 RESULTS AND DISCUSSION

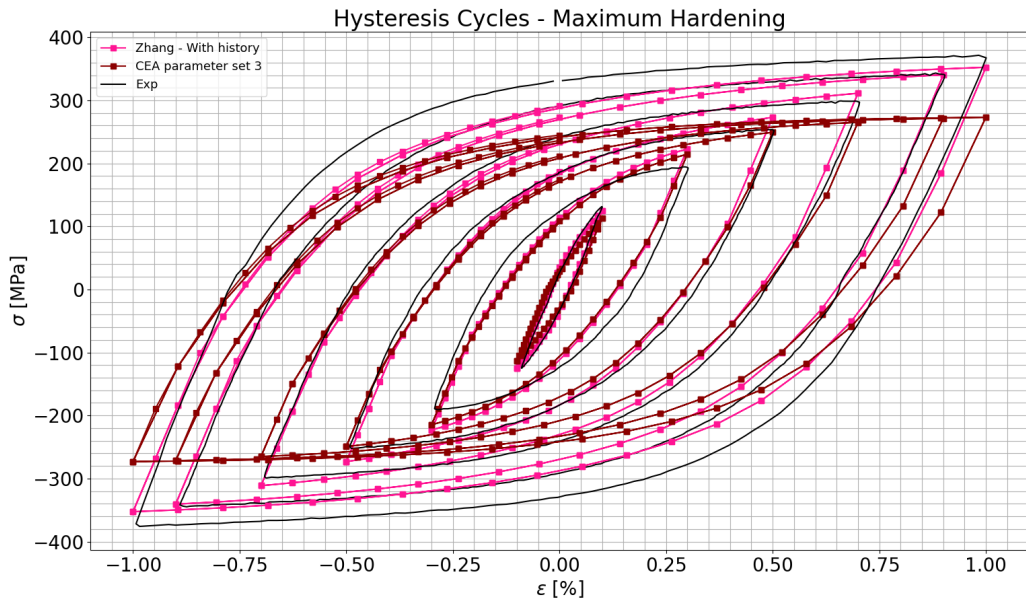


(a) Comparison between CEA parameter sets and experimental data at maximum hardening stage of fatigue life, with separate plots for each strain amplitude.

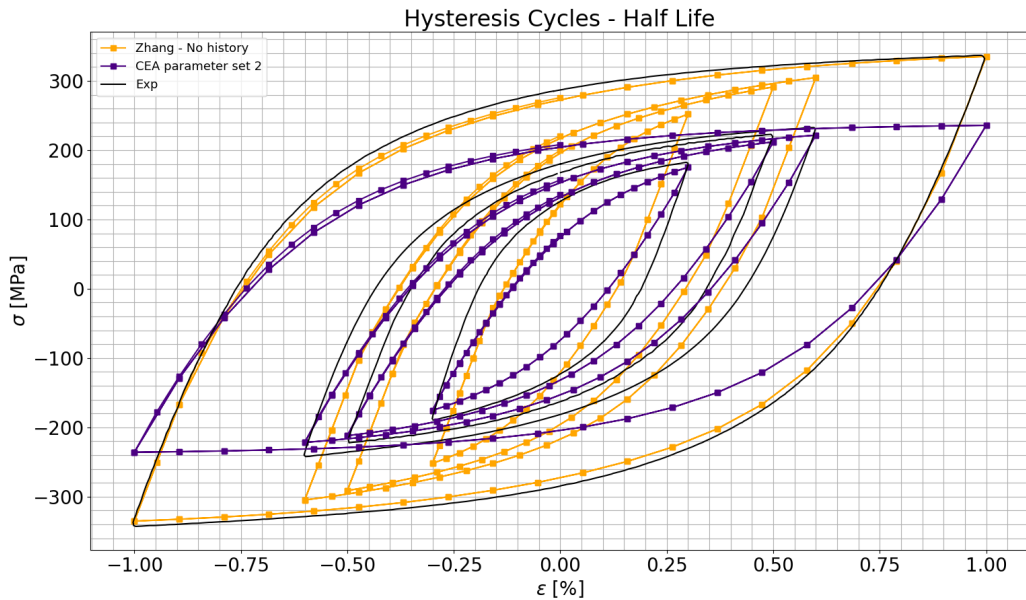


(b) Comparison between CEA parameter sets and experimental data at half life stage of fatigue life, with separate plots for each strain amplitude.

Figure 25: Figure comparing simulation results with experimental data using CEA parameter sets, with separate subplots for each strain amplitude.



(a) Comparison between best parameter sets for the maximum hardening stage of fatigue life.



(b) Comparison between best parameter sets for the half life stage of fatigue life.

Figure 26: Comparison of simulation results from the best parameter sets for both fatigue life stages studied.

The following steps of the work focuses only on studying the behavior of the 316L steel at half life stage, however the methodology implemented could be used to study the maximum hardening stage as well. It is of the interest of the INCEFA-SCALE contributors to draw attention to the half life behavior of the material, as this is the stage that most real life components in the nuclear sector are found. With the aim of finding an appropriate numerical model that can accurately describe the behavior of real scale specimens, the best parameter sets found for the half life

stage are tested using Framatome's specimen (Figure A.1), under the same loading conditions considered during the preliminary analysis where the `code_aster` framework was validated. The results using both numerical models can be found in Tables 9 and 10. From these results, it is possible to see that there is a major disagreement between the numerical and the experimental results obtained. The relative errors found can be read on Table 11.

Lab	Step	$F[\text{N}]$	Target $\varepsilon_{\text{VM}}[\%]$	$\varepsilon_{\text{VM}}[\%]$ -Zhang	$\varepsilon_{\text{VM}}[\%]$ -CEA 2
FRF	-	8908	0.6	0.3427	0.8696

Table 9: Obtained ε_{VM} results at the notch root on Framatome's diagnostic test, using Zhang's parameter set without history effect and the parameter set 2 from CEA to describe the Chaboche constitutive model.

Lab	Step	$F[\text{N}]$	Ext. amplitude[mm]	FEA-FRF[51]	FEA-CEA[51]	FEA-Zhang	FEA-CEA 2
FRF	-	8908	0.0240	0.0257	0.0259	0.01637	0.03139

Table 10: Comparison between extensometer results obtained by INCEFA-SCALE members on the diagnostic test using Framatome's specimen and the ones with Zhang's parameter set without history effect and the parameter set 2 from CEA to describe the Chaboche constitutive model.

Lab	Step	$\delta[\%]$ -FRF	$\delta[\%]$ -CEA	$\delta[\%]$ -Zhang	$\delta[\%]$ -CEA 2
FRF	-	7.08	7.92	-31.79	30.78

Table 11: Comparison of the relative errors obtained in the FEA simulations for the extensometer amplitude measurement, using the best parameter sets found.

In conclusion, both numerical models fail to describe correctly the behavior of the 316L steel when compared with the experimental data at half life stage. Thus, an optimization of the Chaboche constitutive model parameters must be performed to find a more accurate numerical model. For this, the framework presented in Section 4 will be used, so as to implement the NSGA-II algorithm to find an optimal parameter set.

5.1.3 Optimization of the Chaboche model parameters

When implementing the NSGA-II algorithm, it is of pivotal importance to draw attention to the definition of the objective functions and the algorithm parameters that will be considered. For the optimization campaign, only the cubic mesh is considered, as the numerical model should be able to accurately represent the 316L steel behavior in such simple geometry, before going to the full-scale specimens. Additionally, using the cubic mesh diminishes the computational burden associated with the optimization process, since it demands a high number of objective function evaluations.

By defining objective functions that quantifies the error between numerical and experimental results, it is possible to run the NSGA-II algorithm to minimize all these objective functions. In the current work, the objective functions built correspond to the *Root Mean Square Error* (RMSE) function with 4 points of the hysteresis loop at any given strain amplitude $\Delta\varepsilon/2$, being them the points closest to $\varepsilon = 0.0\%$ with $\sigma > 0$ and with $\sigma < 0$, the point of maximum stress and the point of minimum stress. In reality, the objective function could use as many points as desired, however to reduce the computational burden and to reduce the complexity of the implementation, only 4 points were considered.

For instance, given a set of strain amplitudes $\{(\Delta\varepsilon/2)_1, (\Delta\varepsilon/2)_2, \dots, (\Delta\varepsilon/2)_m\}$, for $m \in \mathbb{N}^*$, then the m th objective function writes out as:

$$f_m = \sqrt{\sum_{i=1}^4 \frac{(\sigma_{exp,i} - \sigma_{simu,i})^2}{4}} \quad (17)$$

Where $\sigma_{exp,i}$ and $\sigma_{simu,i}$ are the corresponding stress measured at the point i of the hysteresis loop for the experimental data and via FEA, respectively. This enumeration of points in a stabilized hysteresis loop can be seen in Figure 27.

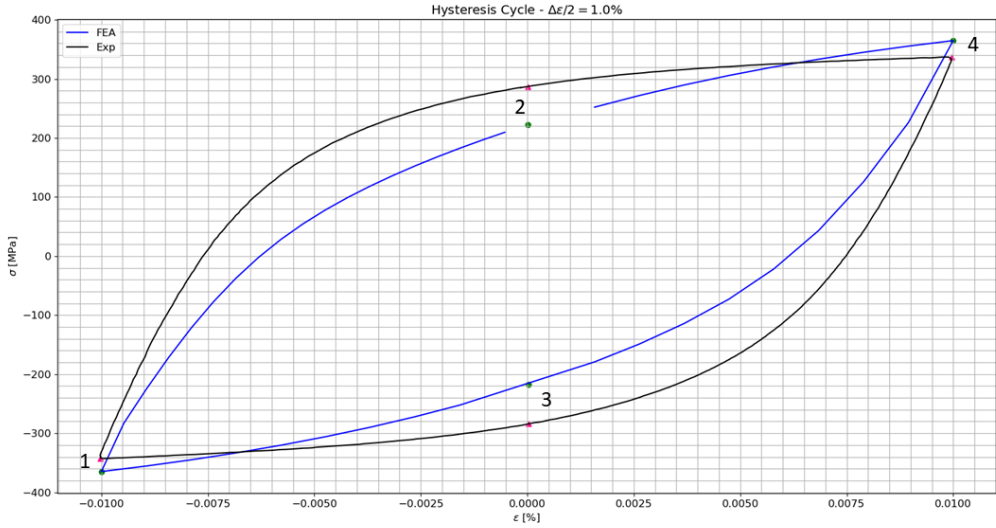


Figure 27: Enumeration of points of interest to compute objective functions with Equation 17, with FEA result with arbitrary set of parameters.

Consider the points in Figure 27 to be denoted as $P_{exp,i}$ and $P_{FEA,i}$, for $i \in \llbracket 1, 4 \rrbracket$, for the experimental and the FEA loops, respectively. For $i = 1$ and $i = 4$ we have:

$$\begin{aligned} P_{exp,1} &= (\min(\varepsilon_{exp}), \min(\sigma_{exp})) \\ P_{FEA,1} &= (\min(\varepsilon_{FEA}), \min(\sigma_{FEA})) \\ P_{exp,4} &= (\max(\varepsilon_{exp}), \max(\sigma_{exp})) \\ P_{FEA,4} &= (\max(\varepsilon_{FEA}), \max(\sigma_{FEA})) \end{aligned}$$

One could argue that $P_{exp,1}$ and $P_{exp,4}$ are not defined in the best manner, since the experimental errors could lead to finding a stress different than the minimum or maximum when you consider the minimum or maximum strain, however it is important to recall that the hypothesis behind the definition of points 1 and 4 are simply there to simplify the analysis. This approximation does not mislead the research, since the deviation is negligible, and it still serves the purpose of being a manner for which we can compare both curves and quantify the numerical error in the simulations. Regarding the FEA results, indeed the point of minimal stress is the point of minimal strain and the point of maximum stress is the point of maximum strain.

Regarding points 2 and 3, a different procedure was necessary to extract a point that could be used for comparison. Let $\varepsilon_{exp}^+ = \{\min |\varepsilon_{exp}| \mid \sigma_{exp} > 0\}$ and $\varepsilon_{exp}^- = \{\min |\varepsilon_{exp}| \mid \sigma_{exp} < 0\}$. Thus, $P_{exp,2} = (\varepsilon_{exp}^+, \sigma_{exp}(\varepsilon_{exp}^+))$ and $P_{exp,3} = (\varepsilon_{exp}^-, \sigma_{exp}(\varepsilon_{exp}^-))$. We select these points because the

experimental data does not have a measure exactly at $\varepsilon_{exp} = 0.0\%$, meaning that the closest point must be considered. The corresponding FEA points of the hysteresis loop are obtained via linear interpolation, considering the neighboring ε_{FEA} points of ε_{exp}^+ and ε_{exp}^- .

With these 4 points, Equation 17 is able to quantify how far away is the numerical result from the experimental one, by taking into account the error at the extreme points and also control the shape of the hysteresis loop via the error at ε_{exp}^+ and ε_{exp}^- . When minimizing the objective function thus, the aim is to minimize the error at the extremities and to adjust the shape of the obtained hysteresis loop via FEA.

Additionally, each DoE $a \in \chi$ is written as $a = \{R_0, b, C_1, C_2, \gamma_1, \gamma_2\}^T$. It is possible to observe that this is the set of parameters defining the Chaboche constitutive model without history effect, and for all the DoEs the young modulus E and the Poisson's ratio ν has been fixed at 160 GPa and 0.3, respectively. This is due to the fact that after analyzing the experimental data, it has been found that $E = 160$ GPa is the most appropriate value to represent the elastic behavior of the 316L steel, while $\nu = 0.3$ is the most common used value for this parameter, being the one used for the Zhang parameter set and the CEA parameter set 2, which were the most accurate parameter sets studied in Section 5.1.2, as well as being the most agreed upon value for this material.

Inspired by all studied parameter sets, the range where each of the parameters could vary was defined, and thus a formal mathematical formulation of the problem could be written as follows:

$$\begin{aligned}
 & \text{minimize: } a_f = \{f_1(\mathbf{x}_a), \dots, f_m(\mathbf{x}_a)\}^T \in \mathbf{X} \subset \mathbb{R}^m \\
 & \text{by changing: } R_0 \in [50, 150] \text{ MPa} \\
 & \quad b \in [4, 12] \\
 & \quad C_1 \in [120000, 200000] \text{ MPa} \\
 & \quad C_2 \in [15000, 30000] \text{ MPa} \\
 & \quad \gamma_1 \in [1000, 2000] \\
 & \quad \gamma_2 \in [100, 300]
 \end{aligned} \tag{18}$$

After formulating the mathematical problem to be studied, we proceed by describing how the different parameters of the NSGA-II algorithm were chosen. By implementing the algorithm within the capabilities of the computational cluster from EDF named Cronos, the time required for the computations was diminished, as each objective function evaluation was performed independently, as single jobs submitted to the cluster, however there was still a time limit of 72 hours for the R&D team, meaning that some decisions had to be made in order to run such evolutionary algorithm, which affected the final results.

Due to the imposed time limit, the best combination for the number of generations n_{gen} and the population size N that would benefit both the exploration as well as exploitation was $(n_{gen}, N) = (20, 20)$, which is a fairly low number for both variables. Dealing with such a complex problem would in reality require a very high number of generations and a bigger population, to ensure better convergence towards the global minimum, however due to constraints found in the project, this choice had to be done.

Another choice that had to be done is regarding the number of cycles to obtain the stabilized hysteresis loop. Due to time constraints, only a small number of 3 cycles was considered for each strain amplitude each time the evaluation of an individual was conducted. A higher number of cycles would enhance the results, however it was found that for a number of cycles greater than 3, the difference in the simulation results was not as significant, thus we neglect this to save the computational time required for each individual evaluation.

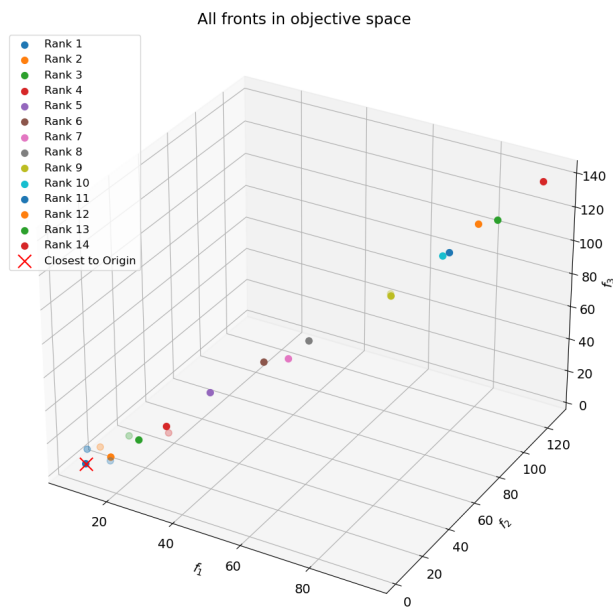
The parameters η_{SBX} and η_{PM} discussed in Section 4.2.3 vary throughout the simulations. This is done in order to ensure initial incentive to exploration, and then to promote the exploitation of the studied spaces in χ . The initial value for both parameters is 2 and it increases

linearly generation after generation up until 20, going from a low value to a high value in the common range of values for these parameters.

For all simulations, the probability of crossover and probability of mutations is 0.9 and 0.1, respectively, thus promoting higher variability due to the genetic information of the most fitted individuals, rather than allowing the mutation to interfere as much in the evolution of the population. All NSGA-II parameters could be altered to study how the algorithms converges towards a solution, however due to time constraints these were the only parameter values used for the algorithm throughout the study.

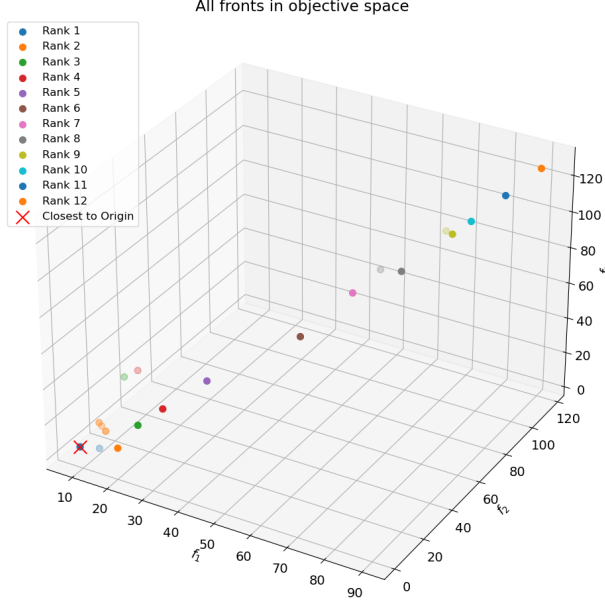
For the implementation of the optimization algorithm within Python, the DEAP [56] library was used, and a complete framework to work using the NSGA-II algorithm has been built for the interest of the researchers from the Ermes group at EDF. DEAP stands for Distributed Evolutionary Algorithms in Python, and this is a very popular library in the optimization community, for being able to implement a wide variety of evolutionary algorithms and with ease of implementation, allowing users to quickly build their frameworks for their research interests and customize many parameters freely. In addition, the DEAP library has an extensive documentation, making it easier for new users to learn and implement the algorithms on their own.

Initially, a value of $n_{\text{gen}} = 10$ was used for testing, with a population $N = 20$, and later on the value of n_{gen} is increased. After running the NSGA-II algorithm twice, it was possible to conclude the same that CEA concluded in the INCEFA-SCALE report [51]. As one tries to optimize the Chaboche constitutive model parameters to fit the FEA results to the experimental ones, either you have good results for bigger strain amplitudes or the opposite. It was observed good convergence of the numerical model towards the smaller strain amplitudes, while at $\Delta\varepsilon/2 = 1.0\%$ the optimized model is not accurate. Thus, the strain amplitude values considered to optimize were 0.3, 0.5 and 0.6%, meaning that the number of objectives was reduced by one, leading to now 3 objective functions to be minimized. The formulation of the problem remains analogous, with $m = 3$. After running one time with $n_{\text{gen}} = 10$ and twice with $n_{\text{gen}} = 20$, the best results out of all these runs were collected, and the distribution of points in objective space can be seen in Figure 28.

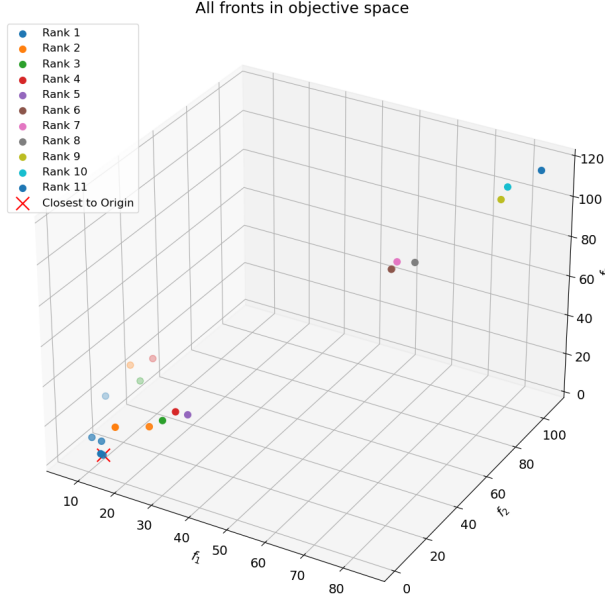


(a) Individuals plotted in the 3D objective space, for $(n_{\text{gen}}, N) = (10, 20)$.

5 RESULTS AND DISCUSSION



(b) Individuals plotted in the 3D objective space, for the first run with $(n_{\text{gen}}, N) = (20, 20)$.



(c) Individuals plotted in the 3D objective space, for the second run with $(n_{\text{gen}}, N) = (20, 20)$.

Figure 28: Illustration of all individuals in the three-dimensional objective space, for all runs of the NSGA-II algorithm.

From these optimization runs, it was possible to observe a big number of ranks in every population, thus not really identifying many individuals to compose the global \mathcal{F}_1 front. In addition, the individuals tend to converge to a straight line in all the optimization runs. The individual closest to the origin in all the runs is considered as the best one, in order to value how good the individual performed when compared with the experimental data in all analyzed strain amplitudes. After evaluating the aggregate of all populations, the best parameter set found is shown in Table 12, compared with Zhang's parameters without history effect:

	Parameters	Zhang	OPT
Elasticity	E [GPa]	160	160
	ν	0.3	0.3
Kinematic Hardening	C_1 [MPa]	170000	165244.7511
	γ_1	1500	1985.0713
	C_2 [MPa]	25000	20257.3104
	γ_2	200	210.9897
Isotropic Hardening	R_0 [MPa]	110	81.4267
	b	10	4.5444

Table 12: Obtained optimized parameter set for the Chaboche constitutive model, compared with Zhang's parameters.

Here, OPT stands for the optimal parameter set results. By using the optimized parameters to compare the hysteresis loops using the cubic mesh, we can compare again the obtained results with the experimental data, and this is represented in Figure 29. We can see excellent convergence for strain amplitudes of 0.5 and 0.6%, and a fairly accurate representation for the strain amplitude of 0.3%. The results are considered to be good for the test with the full-scale specimens from the laboratories contributing to the INCEFA-SCALE project. The result for $\Delta\varepsilon/2 = 1.0\%$ is presented as well, to illustrate how optimizing for smaller strain amplitudes affects the results for higher strain amplitudes.

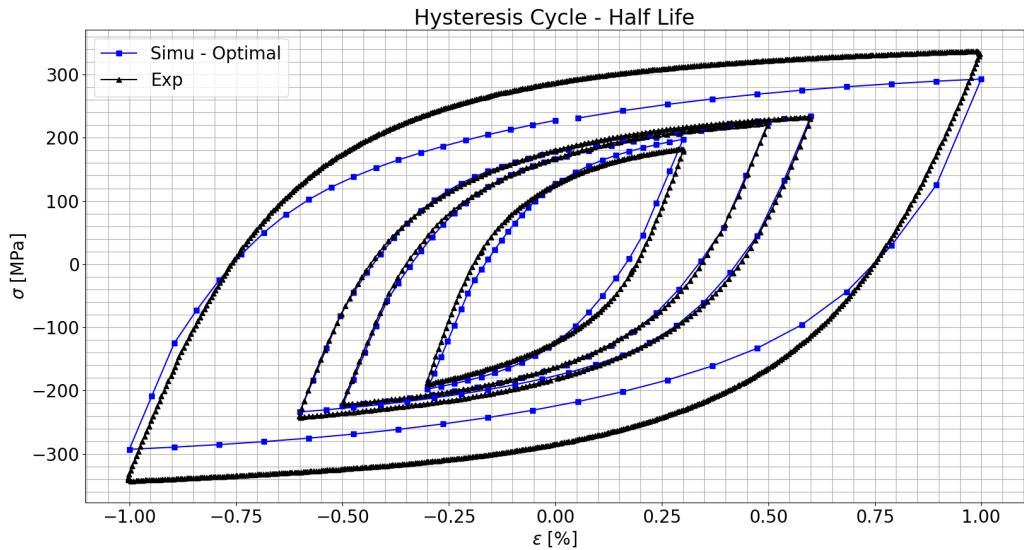


Figure 29: Hysteresis loops found using the optimized parameter set, compared with experimental data at half life stage of fatigue life.

From now, the optimal parameter set will be used to conduct another numerical campaign in the notched specimens described in Figure 17, in order to conduct a comparison between the results obtained by Framatome and CEA in the modeling plans report [51] and the ones obtained by using the optimized parameters.

5.1.4 Implementation of optimized parameters in diagnostic tests

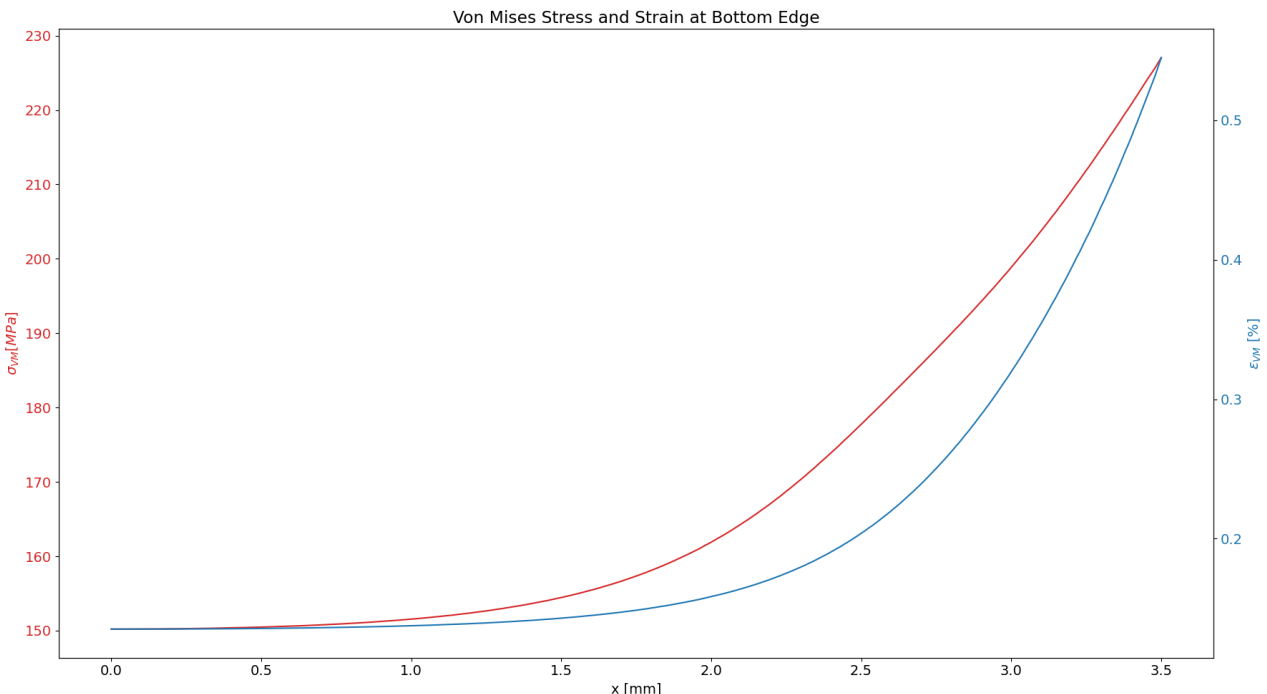
Using the optimized parameters in the notched specimens present in the diagnostic tests provides us the results found in Table 14. In this table, $\delta_{\varepsilon_{VM}}$ stands for the relative error in the measure of

5 RESULTS AND DISCUSSION

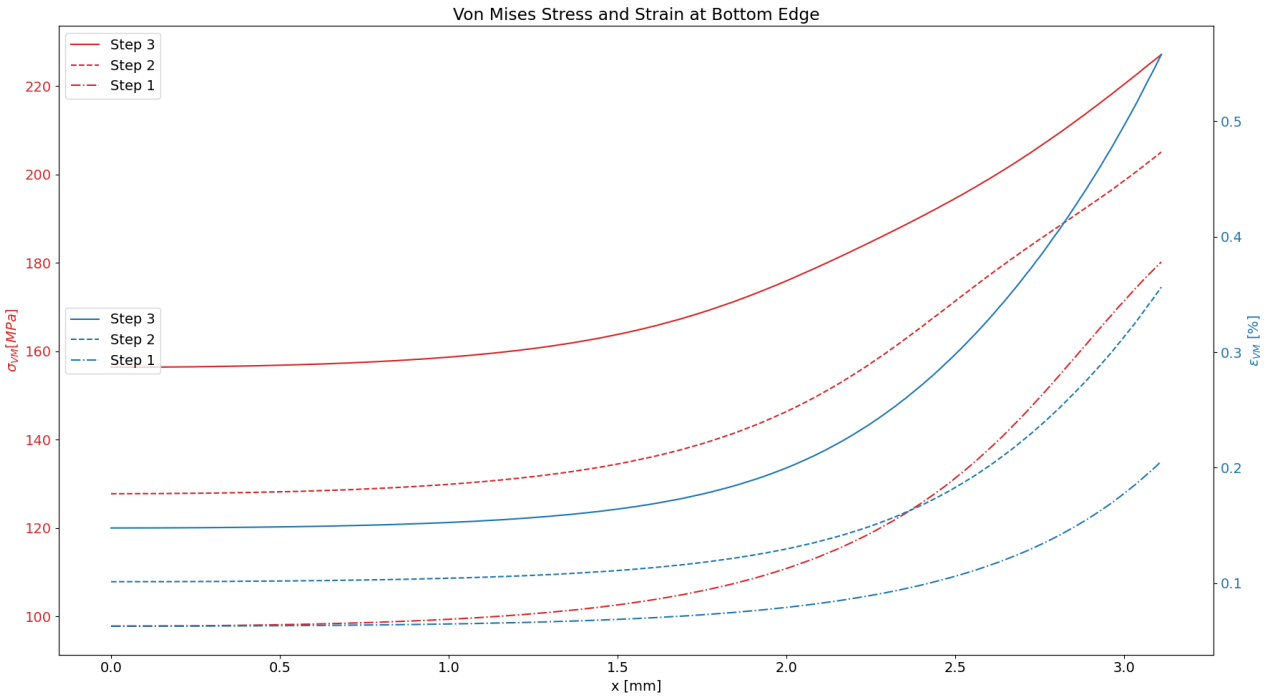
ε_{VM} in relation with the target ε_{VM} at the notch, meaning that it is formulated in an analogous manner to Equation 14. For these results to be obtained, 8 full cycles were considered in the Framatome specimen test and in each step of the KTU specimen test, however for the EDF specimen only 3 cycles per step could be implemented, as the computational time required with the available resources would exceed the time limit of 72 hours, imposed in the R&D team when using the Cronos cluster. The values contained in the strain and the extensometer amplitude measurements were rounded up to a fixed number of decimal places, however the relative errors δ were computed using the full numerical results and afterwards rounded up to 2 decimal places.

From these results, we can conclude that the optimized model achieves the same level of accuracy than the numerical models developed by Framatome and CEA, and it even gets more accurate results in some cases.

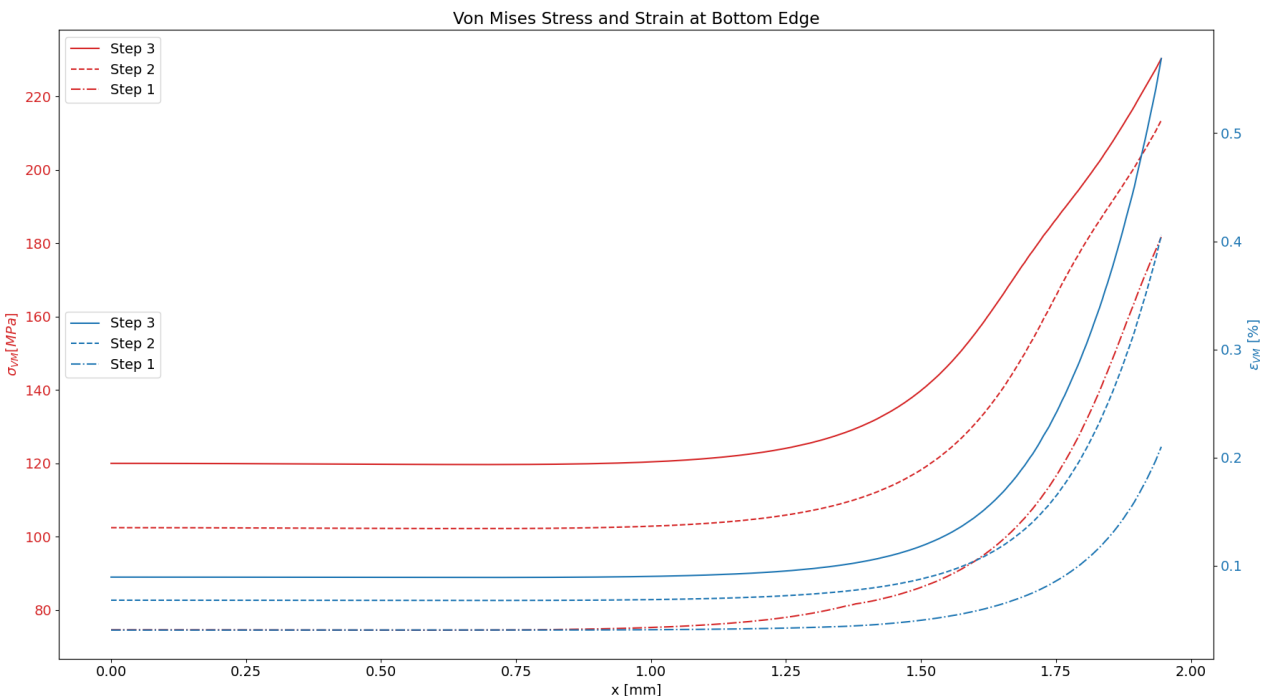
Considering yet the diagnostic tests, Figure 30 presents the evolution of the Von Mises equivalent stress and strain the bottom edge of all diagnostic specimens, while Figure 31 presents the obtained hysteresis loops at the final loop for all designated strain amplitudes $\Delta\varepsilon/2$. The hysteresis loops were obtained by artificially signing the Von Mises equivalent strain in order to represent the compression stage, thus whenever ε_{VM} is negative, in reality it is just a way of visualizing the compression stage of the test. This way, we can visualize if the resulting hysteresis loop is symmetrical or not.



(a) Von Mises equivalent stress and strain at bottom edge, using the optimized parameter set on the Framatome diagnostic test.



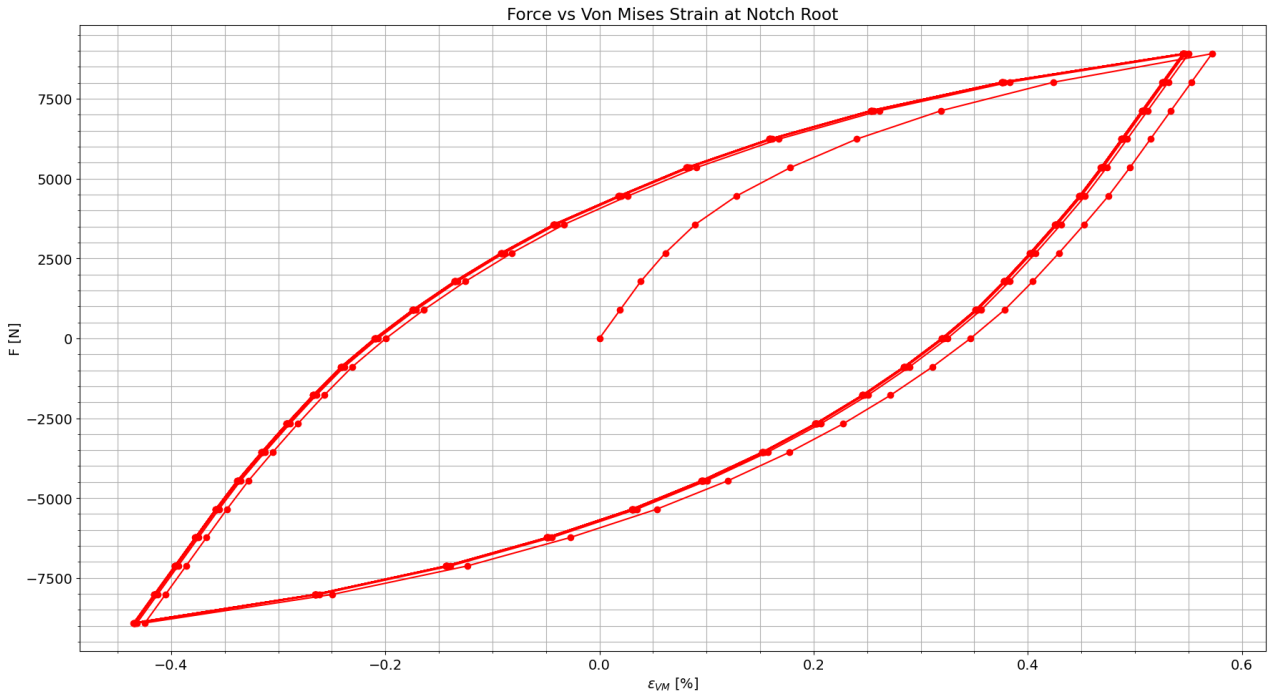
(b) Von Mises equivalent stress and strain at bottom edge, using the optimized parameter set on the EDF diagnostic test.



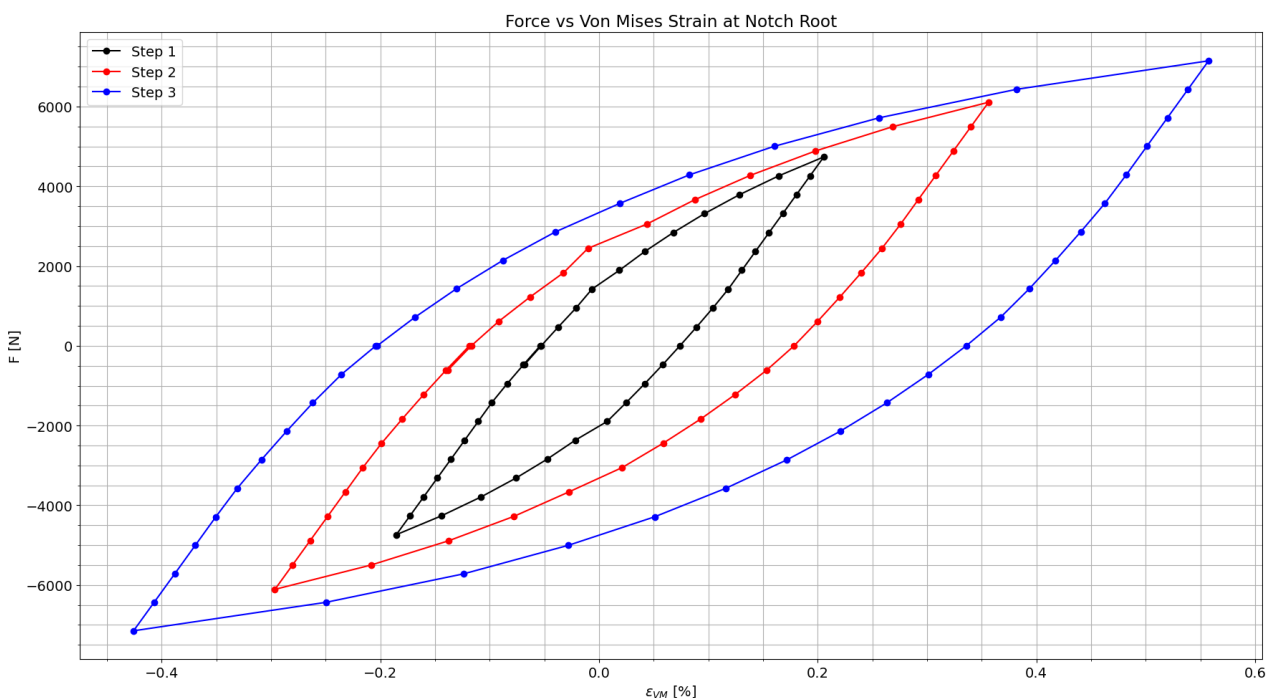
(c) Von Mises equivalent stress and strain at bottom edge, using the optimized parameter set on the KTU diagnostic test.

Figure 30: Von Mises equivalent stress and strain at bottom edge, using the optimized parameter set on all diagnostic tests.

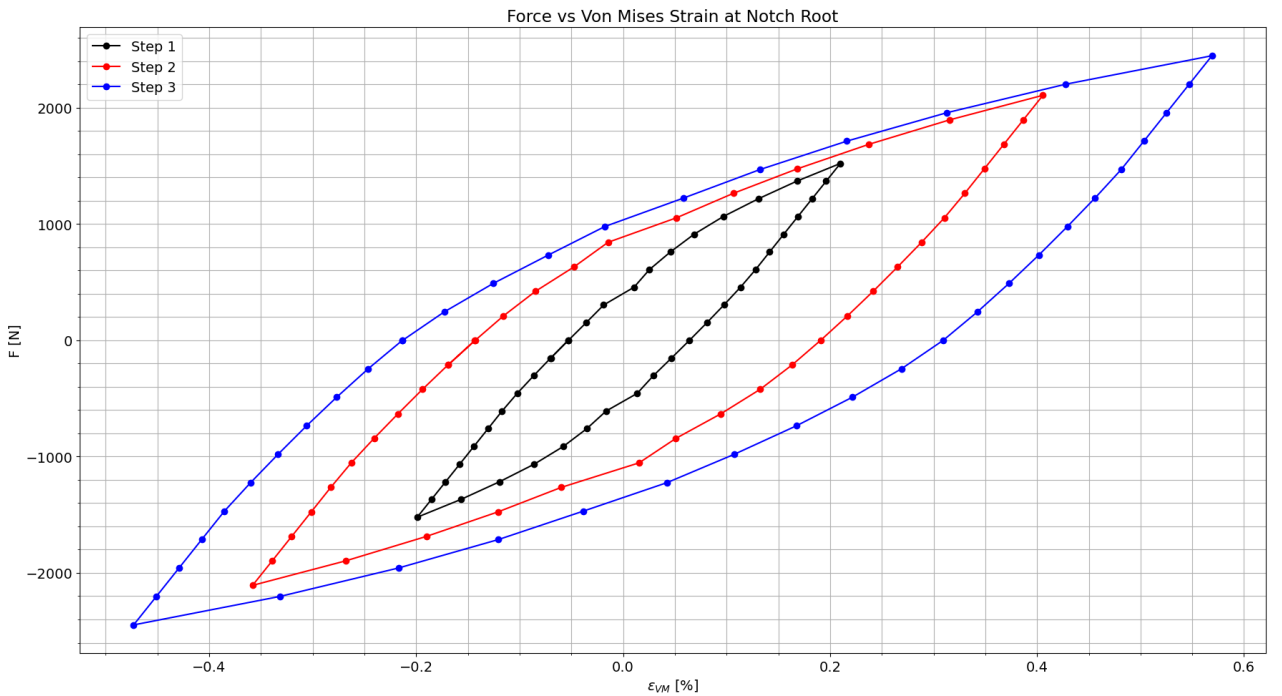
5 RESULTS AND DISCUSSION



(a) Hysteresis loop considering the applied force and the Von Mises equivalent strain, using the optimized parameter set on the Framatome diagnostic test.



(b) Hysteresis loop considering the applied force and the Von Mises equivalent strain, using the optimized parameter set on the EDF diagnostic test.



(c) Hysteresis loop considering the applied force and the Von Mises equivalent strain, using the optimized parameter set on the KTU diagnostic test.

Figure 31: Hysteresis loops using the optimized parameter set on all diagnostic tests, considering the applied force and the Von Mises equivalent Strain as key parameters.

From there results, it is possible to note a few things. First of all, the exponential behavior at the bottom edge observed with the Framatome specimen is different than the one observed using the stress-strain curve, regarding values and shape. The main reason for such discrepancy is that $\varepsilon_{VM} \neq 0.6\%$ at the notch root, meaning that the increase in stress and deformation at the notch root is not so steep, and the stress found is smaller as well.

In addition, although the exponential behavior is found for all the specimens, the levels of stress are not the same, but this could be simply due to the fact that the target strain value at the notch root was not reached.

Moreover, it is possible to note from the hysteresis loops that for higher strain values at the notch root, the loop becomes more and more anti-symmetrical.

In summary, the results found are very promising, as the accuracy of the FEA analysis have been improved in many cases, and all the optimization methodology followed in the study could easily be implemented in other scenarios to improve FEA results.

5.1.5 Implementation of optimized parameters in new specimens

Now, using the same set of optimized parameters, other specimens were studied, for which only a few or no numerical results were available for comparison. They are presented in Tables 15. In this table, the key geometrical parameters from Figure 13 (D, d, r) are presented.

In Table 15, VTT and UC stands for the Technical Research Centre of Finland and the University of Cantabria, respectively, being both of them contributors of the INCEFA-SCALE project.

When referencing the laboratories in the tables, it is important to recall that these are the laboratories conducting the experimental test. Framatome and KTU tests are always conducted with the specimens from Figures A.1 and A.3, respectively, while the tests conducted by EDF, VTT and the University of Cantabria utilizes the specimen illustrated in Figure A.2.

Some of the geometries considered in Table 15 were already illustrated in Figure 17, but now have been implemented with a different maximum load F . Moreover, Figure 32 presents the new meshes used in this step of the work, however the red dot indicating the point to measure vertical displacement has been omitted. Again, the meshes here are bi-quadratic, for the same reasoning as for the former meshes.

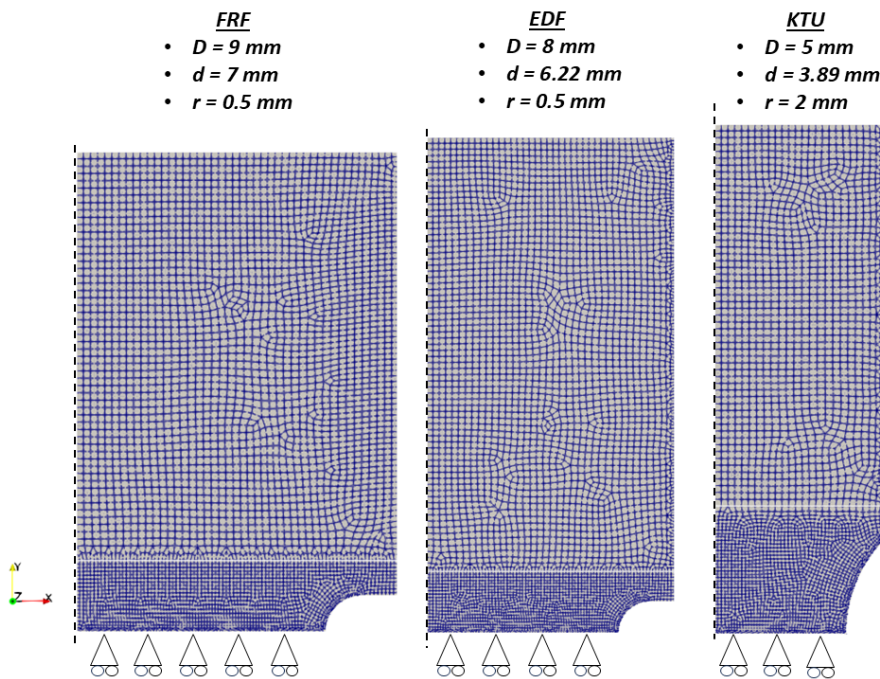


Figure 32: Illustration of the new meshes used for the numerical simulations on the notched specimens, together with the respective design parameters defining each geometry.

In Table 15, the extensometer gage length is made explicit, as some of the rows contains multiple results, measured at different positions of the specimens. It is also possible to notice that some of the experimental data is missing, and this is due to the fact that not all experimental tests and numerical simulations were conducted by the other members of the INCEFA-SCALE project by the writing of this report, thus the results obtained using the optimized parameters will serve as comparison parameter for all participants in the future of the project.

In Table 13 we can see the relative errors found in the obtained results from Table 15. Again, the cells of the table with no results are simply because there is no experimental data to compare with, thus there is no way to express the relative error. Nevertheless, we can see by using these two tables that the results obtained using the optimized parameters have the same order of magnitude as the ones found experimentally, and their computed errors are fairly close to the ones obtained via FEA by Framatome, or even better in some cases.

Lab	D[mm]	d[mm]	r[mm]	F[N]	$\delta[\%]$ -FRF	$\delta[\%]$ -OPT
FRF	9	7	2	6895	44.96	53.55
EDF/UC/VTT	8	6.22	2	5516	-/-/42.11	-/-/48.80
VTT	8	6.22	2	7147	32.92	14.47
KTU	5	3.89	0.5	1862	-	-
FRF	9	7	0.5	5167	10.4	23.66
FRF	9	7	0.5	7131	11.09	18.70
EDF/UC/VTT	8	6.22	0.5	4212	7.17/-/17.47	19.72/-/32.63
EDF/UC/VTT	8	6.22	0.5	5758	35.29/-/33.30	41.68/-/40.86
KTU	5	3.89	2	2245	26.99	8.828
KTU	5	3.89	2	2958	-	-

Table 13: Relative errors found for the FEA results in various specimens from the INCEFA-SCALE project.

In addition to these results, the Von Mises equivalent stress and strain at the bottom edge has been computed, as well as the stabilized hysteresis cycle for each one of the tests. There results are omitted in this report due to the high quantity of figures, and there is not much to be seen at final. The same exponential behavior has been obtained for σ_{VM} and ε_{VM} in the bottom edge of all tests, and again the hysteresis cycles are asymmetrical, and the asymmetry grows as ε_{VM} grows.

5.1.6 Conclusion on the notched specimens

In summary, `code_aster` has been well implemented and validated by using the simplistic stress-strain curves and comparing with previous results obtained by the partners of the INCEFA-SCALE project, shown in Section 5.1.1. Furthermore, in Section 5.1.2 a number of parameter sets for the Chaboche Constitutive model were compared, as they were good candidates presented in the INCEFA-SCALE project for the numerical representation of the 316L steel, however the models did not perform well when using the full-scale specimens meshes, thus leading the research to another direction.

To seek an accurate numerical model, the optimization framework with the NSGA-II algorithm was built, and the obtained optimized parameter set performed well both on the cubic mesh and the full-scale specimens meshes. Nonetheless, it is important to recall that by optimizing the parameters to represent the 316L steel behavior in high strains, it would jeopardize the performance at lower strain values. The obtained results are going to serve as future reference for the members of the project, when experimental tests take place for the remaining specimens.

5 RESULTS AND DISCUSSION

Table 14: Comparison with results obtained by INCEFA-SCALE members on diagnostic tests, with different target ε_{VM} at the notch root, compared with the results obtained in this work using the optimized parameters of the Chaboche constitutive model.

Lab	Step	$F[N]$	Target $\varepsilon_{VM}[\%]$	$\varepsilon_{VM}[\%]$ -OPT	$\delta_{\varepsilon_{VM}}[\%]$	Ext. amplitude[mm]	FEA-FRF[51]	FEA-CEA[51]	FEA-OPT	$\delta[\%]$ -FRF	$\delta[\%]$ -CEA	$\delta[\%]$ -OPT
FRF	-	8908	0.6000	0.5450	-9.18	0.0240	0.02570	0.02590	0.02210	7.08	7.92	-7.88
EDE	1	4737	0.2000	0.2060	2.75	0.0080	0.00950	0.01120	0.01070	18.75	40.00	33.73
EDE	2	6108	0.4000	0.3563	-10.93	0.0126	0.01710	0.01680	0.01710	35.71	35.71	33.10
EDE	3	7147	0.6000	0.5580	-7.08	0.0238	0.02720	0.02260	0.02360	14.29	-7.56	-0.87
KTU	1	1521	0.2900	0.2190	5.00	0.00504	0.00530	0.00580	0.00575	5.56	7.41	6.55
KTU	2	2107	0.4000	0.4060	1.43	0.0100	0.0089	0.0104	0.0099	-11.00	4.00	-1.20
KTU	3	2447	0.6000	0.5690	-5.17	0.0168	0.0125	0.0132	0.0127	-25.60	-21.43	-24.31

Lab	D[mm]	d[mm]	r[mm]	$F[N]$	Target $\varepsilon_{VM}[\%]$	$\varepsilon_{VM}[\%]$ -OPT	$\delta_{\varepsilon_{VM}}[\%]$	Ext. length[mm]	Ext. amplitude[mm]	FEA-FRF[51]	FEA-CEA[51]	FEA-OPT
FRF	9	7	2	6895	0.3000	0.2842	-5.27	12	0.008688	0.012594	0.013341	0.013341
EDE/UC/VTT	8	6.22	2	5516	0.3000	0.2788	-7.07	12.5/12.5/12.0	-/-/0.0090	-/-/0.0128	0.0138/0.0138/0.0134	0.0138/0.0138/0.0134
VTT	8	6.22	2	7147	0.6000	0.5487	-8.55	12	0.0198	0.0263	0.0227	0.0227
KTU	5	3.89	0.5	1862	0.3000	0.3128	4.27	10	-	0.0079	0.0079	0.0079
FRF	9	7	0.5	5167	0.3000	0.3155	5.17	12	0.006212	0.006862	0.007687	0.007687
EDE/UC/VTT	8	6.22	0.5	7131	0.6000	0.6197	3.28	12	0.011160	0.012398	0.013247	0.013247
EDE/UC/VTT	8	6.22	0.5	4212	0.3000	0.3148	4.93	12.5/12.5/12.0	0.006875/-/0.00600	0.007388/-/0.00705	0.008231/0.008231/0.00796	0.008231/0.008231/0.00796
KTU	5	3.89	2	2245	0.3000	0.2615	-12.83	10	0.009875/-/0.0096	0.013360/-/0.0128	0.013991/0.013991/0.0135	0.013991/0.013991/0.0135
KTU	5	3.89	2	2958	0.6000	0.6024	0.4	10	0.010800	0.013715	0.011753	0.011753

Table 15: Presentation of numerical results obtained in specimens from various laboratories participating in the INCEFA-SCALE project, using the optimized parameters of the Chaboche constitutive model.

5.2 Variable amplitude loading

The final study conducted in this work is that of the variable loading response of the 316L stainless steel. For this, a *Periodic Over-Underload* (POUL) test was conducted within `code_aster`, and a comparison with experimental data from EDF is presented.

The POUL test is a strain-controlled cyclic loading test with a mean stress equal to zero, initiating at a high strain value for a few cycles, and maintaining a low strain value for a high number of cycles. An illustration of the strain evolution can be seen in Figure 33. This type of test is of extreme importance, since real life components are rarely in use under constant amplitude cyclic loads.

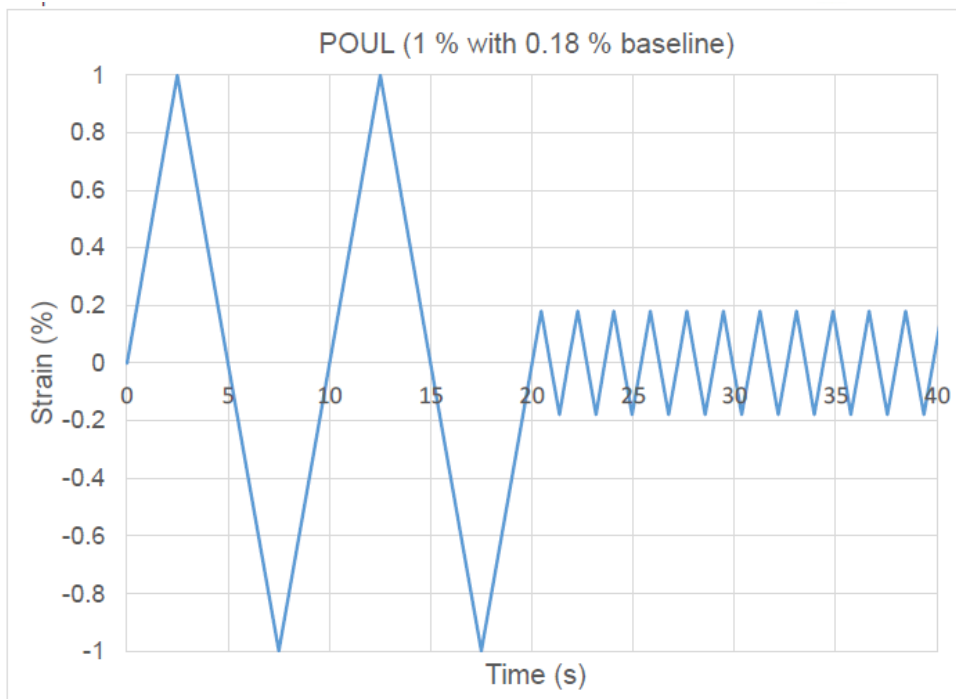


Figure 33: Illustration of the strain evolution in a POUL strain-controlled test.

The POUL test studied in this work consists in two cycles with $\Delta\varepsilon/2 = 1\%$ followed by a thousand cycles with $\Delta\varepsilon/2 = 0.18\%$, repeated until final failure of the piece. The specimen considered in the real life test is the one illustrated in Figure A.2, without any notch.

In order to proceed, a framework in `code_aster` combining the optimized parameter set determined in Section 5.1.3 and Zhang's parameters for the Chaboche constitutive model without history effect were considered. This strategy has been selected so that when $\Delta\varepsilon/2 = 1\%$ the simulation uses Zhang's parameters and when $\Delta\varepsilon/2 = 0.18\%$ it changes to the optimized parameter set, looking to improve the general accuracy of the numerical results. In this numerical analysis, the cubic mesh was used one more time, to reduce the computational burden.

In Figure 34 we can see the maximum and minimum stress after each cycle plotted, comparing the FEA results with the experimental results, obtained by EDF. The simulations were conducted using the cubic mesh, to reduce the computational burden with the high number of cycles in the test, and to avoid running 1000 cyclic simulations each time that $\Delta\varepsilon/2 = 0.18\%$.

Additionally, a limited number of cycles had to be selected. It was observed that after 20 cycles at $\Delta\varepsilon/2 = 0.18\%$ there was a great convergence, thus the same value is repeated until we obtain a total of 1000 cycles at $\Delta\varepsilon/2 = 0.18\%$, in order to compare the numerical results with the experimental ones visually.

Unfortunately, the approach used in this study was not efficient, as it does not replicate the progressive hardening observed in the real life test. The FEA results converge rapidly to a

repeating pattern. However, in the first cycles, it is possible to notice that σ_{min} is not so far from the experimental results, as well as for σ_{max} .

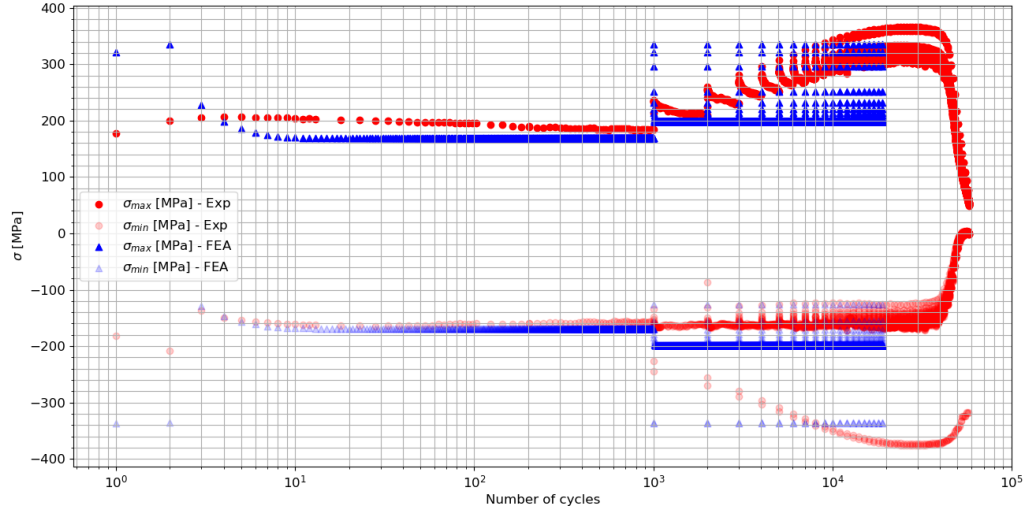


Figure 34: Illustration of the strain evolution in a POUL strain-controlled test.

5.2.1 Conclusion on the variable amplitude loading test

Not much time could be dedicated to this matter in the internship, but some conclusions can be drawn already from what has been tested.

Firstly, the approach of using multiple constitutive model parameters does appear to be promising, however the current study was not able to fully explore this methodology. More work can be done with more experimental data to back up. Since we find ourselves with a very high strain amplitude, the numerical model appears to saturate quickly, and to converge already in the second repetition of the cyclical pattern.

Further work can be done by including the history effect and performing an optimization of Chaboche's parameters at $\varepsilon = 0.18\%$, in order to have models that can better capture the 316 stainless steel behavior in this strain range.

In perspective, it is also possible to explore other constitutive models, such as those that consider more than 2 kinematic hardening components.

Last but not least, it is important to recall that the numerical simulation was conducted in the cubic mesh, so it would be great also to test on the useful section of the specimen, to see if the obtained results would turn out to be the same or not. Due to time constraints, this analysis was not possible during the time frame of the proposed internship program.

6 Conclusion and perspectives

Initially, the main objective of the research project was to conduct numerical simulations to reproduce the fatigue tests done by the INCEFA-SCALE contributors, so as to validate the use of `code_aster` to replicate the mechanical behavior of the specimens and to compare the obtained results with experimental data and FEA results from the partners of the project.

The specimens of the fatigue tests are made of 316L stainless steel. The Chaboche constitutive model has been chosen to be used throughout this work, in order to describe the mechanical behavior of the material in the numerical campaign.

After developing a framework using `code_aster`, validating it and implementing on real scale specimens, it was found that the Chaboche model parameters proposed by Zhang and CEA were not appropriate to describe the material behavior at multiple strain value ranges. Therefore, an optimization of these parameters was necessary. This led to the implementation of the NSGA-II evolutionary algorithm.

Although the optimization process returned parameters that performed well, regarding the accuracy of the model when compared with experimental data, many aspects could improve the obtained results. For instance, the number of generations and the population size in the NSGA-II should both be increased for future studies, because this could lead to more genetic variability and hence promote more exploration of the design space χ .

Another interesting approach would be to also use the optimization framework built to identify an optimized parameter set of the Chaboche constitutive model with history effect. This could potentially enhance the accuracy of the numerical simulations with variable amplitude loading.

Considering yet the optimization algorithm, another algorithm could have been chosen as well. Since this was a first study on the subject for the INCEFA-SCALE project, then a well known evolutionary algorithm was chosen. However, there is an infinitude of evolutionary algorithms to choose. A recommendation for future studies would be to implement a surrogate-assisted evolutionary algorithm, so as to reduce the computational time required for the objective function evaluations, using predictions from surrogate models, such as a Gaussian process or Kriging model. This can save a lot of time, allowing for an increased number of generations and a bigger population size.

Finally, this work served as proof of concept for the methodology implemented, providing many predictions for results that are yet to be determined experimentally in the INCEFA-SCALE project.

7 References

- [1] Institute, Nuclear Energy: *Top 15 nuclear generating countries*, 2022. https://www.nei.org/resources/statistics/top-15-nuclear-generating-countries?__cf_chl_tk=VGNV3JtHWUZSScYP2BJ6Z4Ye6DhN30mB9s47YLbjdqw-1718284065-0.0.1.1-3881, visited on 13 June, 2024.
- [2] gGmbH, GRS: *Nuclear energy worldwide 2024*, 2024. <https://www.grs.de/en/news/nuclear-energy-worldwide-2024>, visited on 13 June, 2024.
- [3] McLennan, Alec, Roman Cicero, Kevin Mottershead, Stephan Courtin, Zaiqing Que, and Sergio Cicero: *Incefa-scale (increasing safety in npps by covering gaps in environmental fatigue assessment-focusing on gaps between laboratory data and component-scale)*. In *Pressure Vessels and Piping Conference*, volume 86144, page V001T01A013. American Society of Mechanical Engineers, 2022.
- [4] Bruchhausen, Matthias, Alec McLennan, Roman Cicero, Caitlin Huotilainen, Kevin Mottershead, Jean Christophe le Roux, and Marc Vankeerberghen: *Incefa-plus project: Review of the test programme*. In *Pressure Vessels and Piping Conference*, volume 83815, page V001T01A015. American Society of Mechanical Engineers, 2020.
- [5] Bergeaud, Vincent and Vincent Lefebvre: *Salome. a software integration platform for multi-physics, pre-processing and visualisation*. 2010.
- [6] Levesque, JR: *The code aster: A product for mechanical engineers; le code aster: Un produit pour les mecaniciens des structures*. Epure, 1998.
- [7] Deb, K., A. Pratap, S. Agarwal, and T. Meyarivan: *A fast and elitist multiobjective genetic algorithm: Nsga-ii*. IEEE Transactions on Evolutionary Computation, 6(2):182–197, 2002.
- [8] Hailer, Raphael Alves: *Stochastic Optimization of X-ray Micro-CT Domain Size Using PuMA PRE - Research Project, ENSTA*. 2023.
- [9] Rivier, Mickael: *Low-cost methods for constrained multi-objective optimization under uncertainty*. PhD thesis, Institut Polytechnique de Paris, 2020.
- [10] Verreet, Dipl Ing Roland: *A short history of wire rope*, 2002.
- [11] Carol, Anne: *Mass Death and Funerary Transition: The Meudon Railway Disaster (France, 1842)*. Death Studies, pages 1–11, October 2023. <https://shs.hal.science/halshs-03836529>.
- [12] Maitournam, H.: *Intégrité et fatigue des structures*. Poly du cours MS203, ENSTA Paris, 2018.
- [13] Schijve, Jaap: *Fatigue of structures and materials*. Springer Science & Business Media, 2008.
- [14] Ahmadivala, Morteza: *Towards optimal maintenance planning of existing structures based on time-dependent reliability analysis*. PhD thesis, December 2020.
- [15] Withey, P.A.: *Fatigue failure of the de havilland comet i*. Engineering Failure Analysis, 4(2):147–154, 1997, ISSN 1350-6307. <https://www.sciencedirect.com/science/article/pii/S1350630797000058>.
- [16] Hou, Nan, Ning Ding, Shen Qu, Weimin Guo, Long Liu, Na Xu, Linan Tian, Huixia Xu, Xiangfeng Chen, Fahmi Zaiiri, et al.: *Failure modes, mechanisms and causes of shafts in mechanical equipment*. Engineering Failure Analysis, 136:106216, 2022.

- [17] Zhang, Wen: *Fatigue crack growth in large scale yielding condition*. PhD thesis, Université Paris Saclay (COMUE), 2016.
- [18] HOMSON, R.M.: *Chapter 26 - fracture*. In CAHN, Robert W. and Peter HAASEN† (editors): *Physical Metallurgy (Fourth Edition)*, pages 2207–2292. North-Holland, Oxford, fourth edition edition, 1996, ISBN 978-0-444-89875-3. <https://www.sciencedirect.com/science/article/pii/B9780444898753500314>.
- [19] Brunet, Joseph, Baptiste Pierrat, and Pierre Badel: *Review of current advances in the mechanical description and quantification of aortic dissection mechanisms*. IEEE Reviews in Biomedical Engineering, 14:1–1, January 2020.
- [20] Rupp, Marius, Marc Eichhorn, and Christelle Kieleck: *Iterative 3d modeling of thermal effects in end-pumped continuous-wave ho3+:yag lasers*. Applied Physics B, 129, December 2022.
- [21] Westergaard, HM: *Bearing pressures and cracks: Bearing pressures through a slightly waved surface or through a nearly flat part of a cylinder, and related problems of cracks*. Journal of Applied Mechanics, 6(2):A49–A53, 1939.
- [22] Williams, ML: *On the stress distribution at the base of a stationary crack*. Journal of Applied Mechanics, 24(1):109–114, 1957.
- [23] Irwin, George R: *Analysis of stresses and strains near the end of a crack traversing a plate*. Journal of applied mechanics, 24:361–364, 1957.
- [24] Tada, Hiroshi, Paul C. Paris, and George R. Irwin: *The Stress Analysis of Cracks Handbook - 3rd Edition*. American Society of Mechanical Engineers, 2000, ISBN 0-7918-0153-5.
- [25] Ju, Yang, Heping Xie, Xi Zhao, Lingtao Mao, Zhangyu Ren, Jiangtao Zheng, Fu Pen Chi-ang, Yongliang Wang, and Feng Gao: *Visualization method for stress-field evolution during rapid crack propagation using 3d printing and photoelastic testing techniques*. Scientific Reports, 8(1):4353, 2018.
- [26] Liu, Mingchao, Yixiang Gan, Dorian AH Hanaor, Bin Liu, and Changqing Chen: *An improved semi-analytical solution for stress at round-tip notches*. Engineering fracture mechanics, 149:134–143, 2015.
- [27] Paris, P.C. and F. Erdogan: *A Critical Analysis of Crack Propagation Laws*. ASME, 1963. <https://books.google.fr/books?id=QhXnoAEACAAJ>.
- [28] P.C. Paris, M.P. Gomez and W.P. Anderson: *A rational analytic theory of fatigue*. The Trend in Engineering, 13:9–14, 1961.
- [29] Ghodrat, Sepideh, Ton Riemsdag, and Leo AI Kestens: *Measuring plasticity with orientation contrast microscopy in aluminium 6061-t4*. Metals, 7(4):108, 2017.
- [30] Chopra, O and GL Stevens: *Effect of lwr water environments on the fatigue life of reactor materials–final report*. United States Nuclear Regulatory Commission, Office of Nuclear Regulatory Research, Rockville, MD, Report No. NUREG/CR-6909, Revision, 1, 2018.
- [31] Thyssenkrupp: *Stainless steel 316l 1.4404*, 2017. <https://www.thyssenkrupp-materials.co.uk/stainless-steel-316l-14404.html>, visited on 13 August, 2024.
- [32] CHABOCHE, JL: *Modelization of the strain memory effect on the cyclic hardening of 316 stainless steel*. In *Transactions of the 5th International Conference of SMiRT, Berlin, 1979*, 1979.

- [33] Haboussa, David: *Relations de comportement élasto-visco-plastique de chaboche [r5.03.04]*. Technical report, September 2013.
- [34] Delmas, Josselin: *Opérateur calc_champ [u4.81.04]*. Technical report, April 2013.
- [35] Peng, Ziling: *Study of environmentally assisted fatigue of austenitic stainless steels in primary water pwr environment*. Internship report, Material and Mechanics of Components Department (MMC), EDF Lab. les Renardières, Moret-sur-Loing, France, 2017. Supervisor: Xianfeng Ma.
- [36] Villa, Céline and Raphaël Labayrade: *Energy efficiency vs subjective comfort: a multiobjective optimisation method under uncertainty*. In *Proceedings of Building Simulation 2011: 12th Conference of International Building Performance Simulation Association, Sydney, 14-16 November*, Sydney, Australia, 2011. International Building Performance Simulation Association (IBPSA).
- [37] Coello, CA Coello: *Evolutionary multi-objective optimization: a historical view of the field*. IEEE computational intelligence magazine, 1(1):28–36, 2006.
- [38] Holland, John H.: *Adaptation in Natural and Artificial Systems*. University of Michigan Press, 1975.
- [39] Goldberg, David E: *Genetic algorithms in search, optimization, and machine learning*. Addison wesley, 1989(102):36, 1989.
- [40] Hornby, Greg, Al Globus, Derek Linden, and Jason Lohn: *Automated antenna design with evolutionary algorithms*. Collection of Technical Papers - Space 2006 Conference, 1, September 2006.
- [41] Lohn, Jason, Greg Hornby, and Derek Linden: *Human-competitive evolved antennas*. AI EDAM, 22:235–247, August 2008.
- [42] Marler, R Timothy and Jasbir S Arora: *The weighted sum method for multi-objective optimization: new insights*. Structural and multidisciplinary optimization, 41:853–862, 2010.
- [43] Wang, Dongshu, Dapei Tan, and Lei Liu: *Particle swarm optimization algorithm: an overview*. Soft computing, 22(2):387–408, 2018.
- [44] Srinivas, Nidamarthi and Kalyanmoy Deb: *Multiojective optimization using nondominated sorting in genetic algorithms*. Evolutionary computation, 2(3):221–248, 1994.
- [45] Abdel-Basset, Mohamed, Laila Abdel-Fatah, and Arun Kumar Sangaiah: *Chapter 10 - metaheuristic algorithms: A comprehensive review*. In Sangaiah, Arun Kumar, Michael Sheng, and Zhiyong Zhang (editors): *Computational Intelligence for Multimedia Big Data on the Cloud with Engineering Applications*, Intelligent Data-Centric Systems, pages 185–231. Academic Press, 2018, ISBN 978-0-12-813314-9. <https://www.sciencedirect.com/science/article/pii/B9780128133149000104>.
- [46] Xiong, Jian, Xu Tan, Ke wei Yang, Lining Xing, and Ying Wu Chen: *A hybrid multiobjective evolutionary approach for flexible job-shop scheduling problems*. Mathematical Problems in Engineering, 2012, August 2012.
- [47] Deb, Kalyanmoy, Ram Bhushan Agrawal, et al.: *Simulated binary crossover for continuous search space*. Complex systems, 9(2):115–148, 1995.
- [48] Deb, Kalyanmoy, Karthik Sindhya, and Tatsuya Okabe: *Self-adaptive simulated binary crossover for real-parameter optimization*. In *Proceedings of the 9th annual conference on genetic and evolutionary computation*, pages 1187–1194, 2007.

- [49] Deb, Kalyanmoy: *Real-coded genetic algorithms with simulated binary crossover: Studies on multimodal and multiobjective problems*. Complex systems, 9:431–454, 1995.
- [50] Zeng, Guo Qiang, Jie Chen, Li Min Li, Min Rong Chen, Lie Wu, Yu Xing Dai, and Chong Wei Zheng: *An improved multi-objective population-based extremal optimization algorithm with polynomial mutation*. Information Sciences, 330:49–73, 2016.
- [51] EDF: *Incefa-scale report d4.2 - mo36 modelling progress*. Unpublished project report, 2024.
- [52] Courtin, Stephan, Olivier Ancelet, Jack Beswick, Oliver Blakesley, and Roman Cicero: *Incefa-scale project—overview of the modelling plans*. In *Pressure Vessels and Piping Conference*, volume 87448, page V001T01A012. American Society of Mechanical Engineers, 2023.
- [53] Nip, K.H., Leroy Gardner, C.M. Davies, and A. Elghazouli: *Extremely low cycle fatigue tests on structural carbon steel and stainless steel*. Journal of Constructional Steel Research - J CONSTR STEEL RES, 66:96–110, January 2010.
- [54] EDF: *Finite element code_aster, Analysis of Structures and Thermomechanics for Studies and Research*. Open source at www.code-aster.org, 1989–2024.
- [55] Liu, G.R. and S.S. Quek: *Chapter 7 - fem for two-dimensional solids*. In Liu, G.R. and S.S. Quek (editors): *The Finite Element Method (Second Edition)*, pages 161–217. Butterworth-Heinemann, Oxford, second edition edition, 2014, ISBN 978-0-08-098356-1. <https://www.sciencedirect.com/science/article/pii/B9780080983561000072>.
- [56] Fortin, Félix Antoine, François Michel De Rainville, Marc André Gardner, Marc Parizeau, and Christian Gagné: *DEAP: Evolutionary algorithms made easy*. Journal of Machine Learning Research, 13:2171–2175, jul 2012.

A Technical Drawings

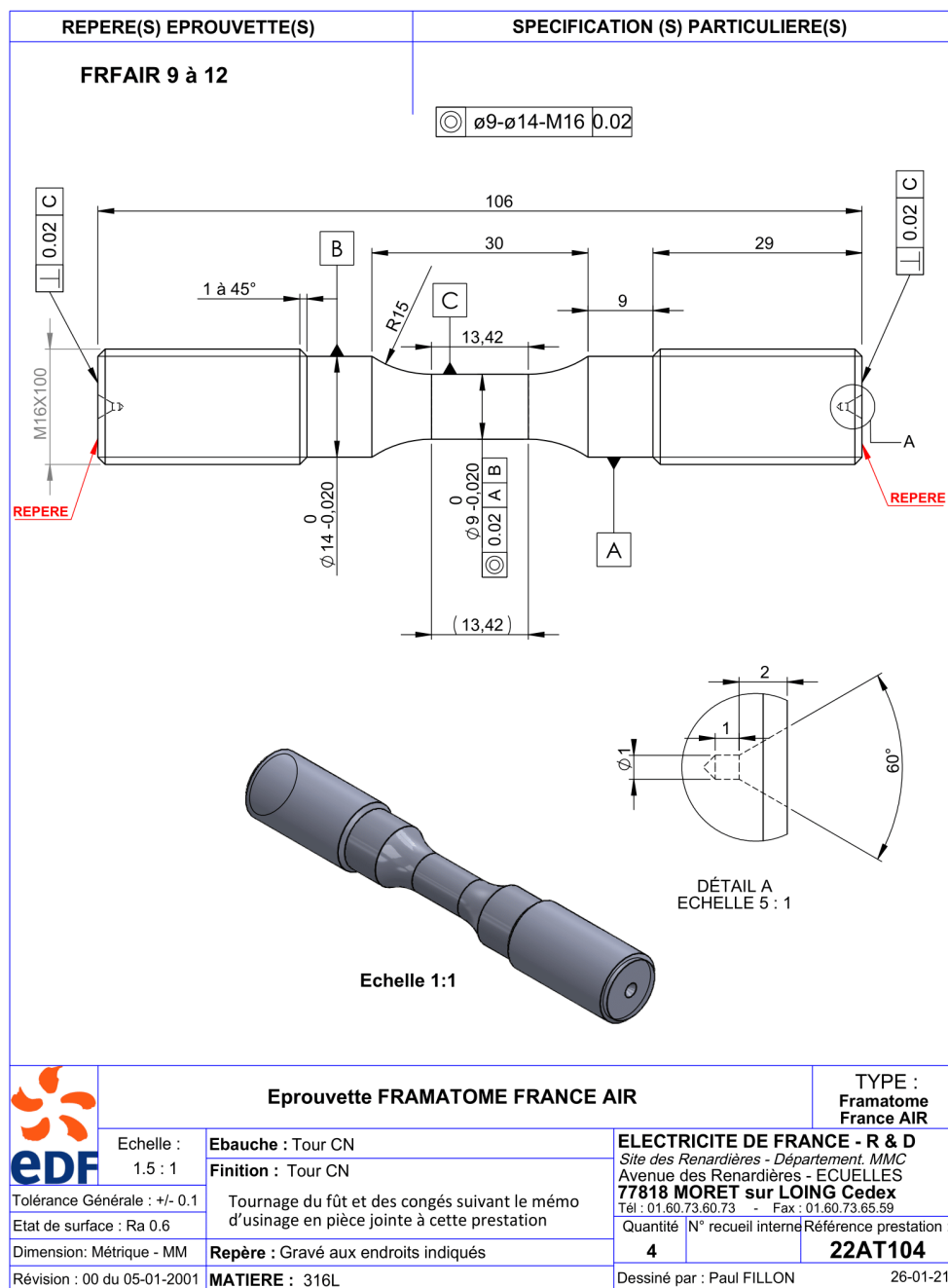


Figure A.1: Framatome France essay specimen used in this work

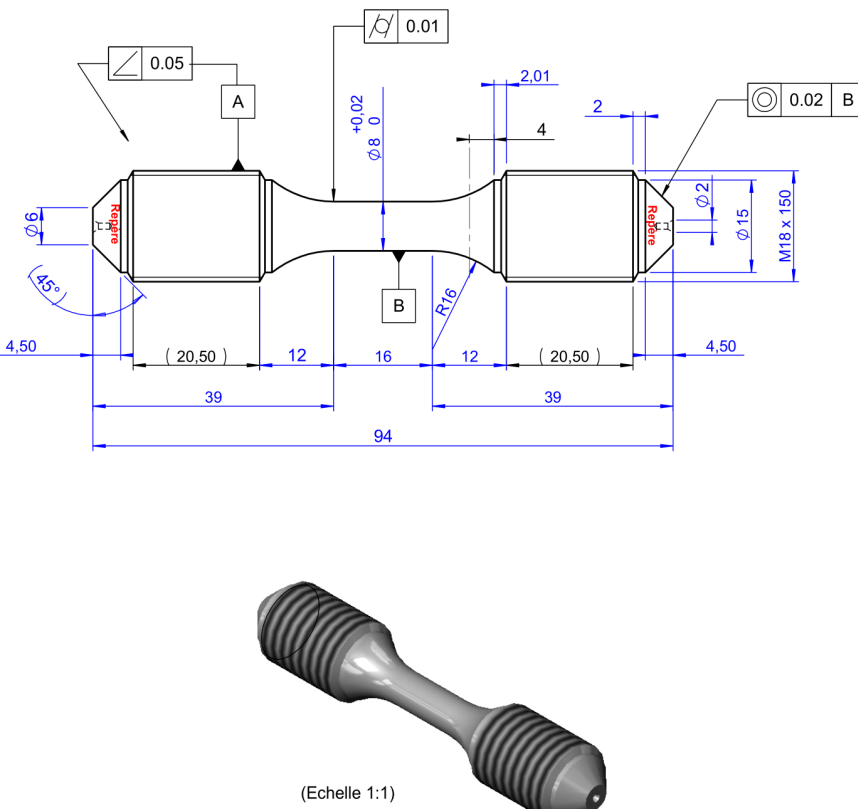
REPÈRE(S) EPROUVEtte(S)	SPECIFICATION (S) PARTICULARIE(S)																				
EDFAIR 6 à 10	 <p>(Echelle 1:1)</p>																				
 EPROUVEtte FFL2	TYPE : FFL2 <table border="1"> <tr> <td>Echelle : 1.25 : 1</td> <td>Ebauche : Tour CN. Finition : Tour CN Tournage du fût et des congés suivant le même d'usinage en pièce jointe à cette prestation</td> <td colspan="2">ELECTRICITE DE FRANCE - R & D Site des Renardières - Département. MMC avenue des Renardières - ECQUELLES 77818 MORET sur LOING Cedex Tél. 01.60.73.60.73 - Fax : 01.60.73.68.89</td> </tr> <tr> <td>Tolérance Générale : +/- 0.1</td> <td>Repère: Gravé à l'endroit indiqué sur le plan.</td> <td>Quantité N° recueil interne</td> <td>Référence prestation : 5 2 - 56 22AT104</td> </tr> <tr> <td>Etat de surface: Ra 0.6</td> <td></td> <td colspan="2">Dessiné par : ALIOUANE Nadji 27-11-2019</td> </tr> <tr> <td>Dimension: Métrique - MM</td> <td>MATIERE : 316L</td> <td colspan="2"></td> </tr> <tr> <td>Révision : 01 du 25-09-2020</td> <td></td> <td colspan="2"></td> </tr> </table>	Echelle : 1.25 : 1	Ebauche : Tour CN. Finition : Tour CN Tournage du fût et des congés suivant le même d'usinage en pièce jointe à cette prestation	ELECTRICITE DE FRANCE - R & D Site des Renardières - Département. MMC avenue des Renardières - ECQUELLES 77818 MORET sur LOING Cedex Tél. 01.60.73.60.73 - Fax : 01.60.73.68.89		Tolérance Générale : +/- 0.1	Repère: Gravé à l'endroit indiqué sur le plan.	Quantité N° recueil interne	Référence prestation : 5 2 - 56 22AT104	Etat de surface: Ra 0.6		Dessiné par : ALIOUANE Nadji 27-11-2019		Dimension: Métrique - MM	MATIERE : 316L			Révision : 01 du 25-09-2020			
Echelle : 1.25 : 1	Ebauche : Tour CN. Finition : Tour CN Tournage du fût et des congés suivant le même d'usinage en pièce jointe à cette prestation	ELECTRICITE DE FRANCE - R & D Site des Renardières - Département. MMC avenue des Renardières - ECQUELLES 77818 MORET sur LOING Cedex Tél. 01.60.73.60.73 - Fax : 01.60.73.68.89																			
Tolérance Générale : +/- 0.1	Repère: Gravé à l'endroit indiqué sur le plan.	Quantité N° recueil interne	Référence prestation : 5 2 - 56 22AT104																		
Etat de surface: Ra 0.6		Dessiné par : ALIOUANE Nadji 27-11-2019																			
Dimension: Métrique - MM	MATIERE : 316L																				
Révision : 01 du 25-09-2020																					

Figure A.2: EDF essay specimen used in this work

A TECHNICAL DRAWINGS

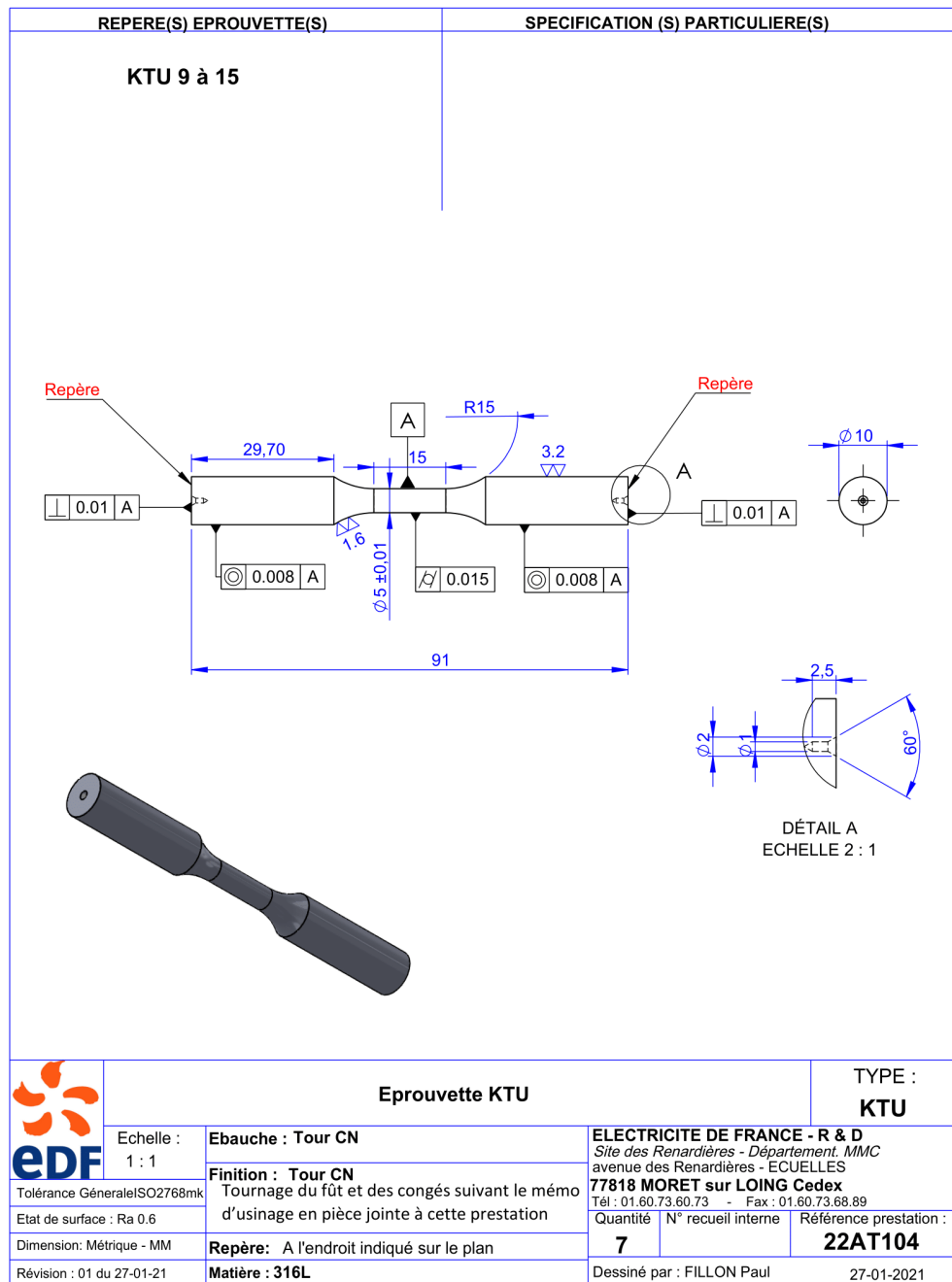


Figure A.3: KTU essay specimen used in this work